FEDERAL UNIVERSITY OF JUIZ DE FORA
INSTITUTE OF NATURAL SCIENCES / FACULTY OF ENGINEERING
GRADUATE PROGRAM IN COMPUTATIONAL MODELING

Nícolas Lima Oliveira

Optimizing Propeller Performance: A Comprehensive Constrained Multi-Objective Design Approach using Blade Element Theory and Evolutionary Algorithms

Juiz de Fora

2023

Nícolas Lima Oliveira

Optimizing Propeller Performance: A Comprehensive Constrained Multi-Objective Design Approach using Blade Element Theory and Evolutionary Algorithms

Doctoral Thesis presented to Graduate Program in Computational Modeling to the Federal University of Juiz de Fora, as a partial requirement to obtain the title of Doctor in Computational Modeling.

Advisor: Prof.ª D.Sc. Patrícia Habib Hallak

Coadvisor: Prof. D.Sc. Afonso C. de Castro Lemonge

Juiz de Fora

2023

Ficha catalográfica elaborada através do Modelo Latex do CDC da UFJF
com os dados fornecidos pelo(a) autor(a)

Lima Oliveira, Nícolas
Optimizing Propeller Performance: A Comprehensive Constrained Multi-Objective Design Approach using Blade Element Theory and Evolutionary Algorithms / Nícolas Lima Oliveira. – 2023.
151 f. : il.

Advisor: Prof.ª D.Sc. Patrícia Habib Hallak
Coadvisor: Prof. D.Sc. Afonso C. de Castro Lemonge
Doctorate Thesis – Federal University of Juiz de Fora, Institute of Natural Sciences / Faculty of Engineering. Graduate Program in Computational Modeling, 2023.

1. Propellers. 2. Optimization. 3. Aerodynamics. I. Habib Hallak, Patrícia, orient. II. C. de Castro Lemonge, Afonso, coorient. III. Título.

Nicolas Lima Oliveira

Optimizing Propeller Performance: A Comprehensive Constrained Multi-Objective Design Approach using Blade Element Theory and Evolutionary Algorithms

Tese apresentada ao Programa de Pós-Graduação em Modelagem Computacional da Universidade Federal de Juiz de Fora como requisito parcial à obtenção do título de Doutor em Modelagem Computacional. Área de concentração: Modelagem Computacional.

Aprovada em 08 de agosto de 2023.

BANCA EXAMINADORA

Profa. Dra. Patrícia Habib Hallak - Orientadora

Universidade Federal de Juiz de Fora

Prof. Dr. Afonso Celso de Castro Lemonge - Coorientador

Universidade Federal de Juiz de Fora

Prof. Dr. Leonardo Goliatt da Fonseca

Universidade Federal de Juiz de Fora

Prof. Dr. Konstantinos Kyprianidis

Mälardalens University

Prof. Dr. Stavros Vouros

Mälardalens University

Prof. Dr. Felipe dos Santos Loureiro

Universidade Federal de São João del Rei

Juiz de Fora, 27/07/2023.

Documento assinado eletronicamente por **Patricia Habib Hallak**, **Professor(a)**, em 08/08/2023, às 14:09, conforme horário oficial de Brasília, com fundamento no § 3º do art. 4º do Decreto nº 10.543, de 13 de novembro de 2020.

Documento assinado eletronicamente por **Leonardo Goliatt da Fonseca**, **Professor(a)**, em 08/08/2023, às 14:09, conforme horário oficial de Brasília, com fundamento no § 3º do art. 4º do Decreto nº 10.543, de 13 de novembro de 2020.

Documento assinado eletronicamente por **Afonso Celso de Castro Lemonge**, **Professor(a)**, em 08/08/2023, às 14:20, conforme horário oficial de Brasília, com fundamento no § 3º do art. 4º do Decreto nº 10.543, de 13 de novembro de 2020.

Documento assinado eletronicamente por **Felipe dos Santos Loureiro**, **Usuário Externo**, em 08/08/2023, às 15:50, conforme horário oficial de Brasília, com fundamento no § 3º do art. 4º do Decreto nº 10.543, de 13 de novembro de 2020.

Documento assinado eletronicamente por **Konstantinos Kyprianidis**, **Usuário Externo**, em 09/08/2023, às 06:01, conforme horário oficial de Brasília, com fundamento no § 3º do art. 4º do Decreto nº 10.543, de 13 de novembro de 2020.

Documento assinado eletronicamente por **Stavros Vouros**, **Usuário Externo**, em 09/08/2023, às 09:20, conforme horário oficial de Brasília, com fundamento no § 3º do art. 4º do Decreto nº 10.543, de 13 de novembro de 2020.

A autenticidade deste documento pode ser conferida no Portal do SEI-Ufjf (www2.ufjf.br/SEI) através do ícone Conferência de Documentos, informando o código verificador **1382376** e o código CRC **FA23EFA6**.

RESUMO

Atualmente são crescentes as preocupações com eficiência energética, sustentabilidade e com o meio ambiente, como proposto pela ONU através do The Global Goals (Goal 9 - Industry, Innovation and Infrastructure), e a busca por novas soluções mais eficientes e limpas é notória em todos os campos da engenharia. Com o avanço de novas técnicas de manufatura, descoberta e desenvolvimento de novos materiais e ampliação das capacidades computacionais surgem novas oportunidades de estudo no campo da engenharia aeronáutica. O presente trabalho propõe a elaboração de uma nova metodologia a ser utilizada no projeto e otimização de hélices, bem como os algoritmos e acoplamentos necessários. Foi realizada uma busca por perfis aerodinâmicos e composto um banco de dados com cerca de 1500 desses. Tais perfis tiveram suas coordenadas padronizadas e refinadas. Todos os perfis aerodinâmicos foram analisados através do método dos painéis utilizando o código XFOIL. Utilizando os algoritmos evolucionários AGEMOEA, ARMOEA, MSOPSII, NSGAII e NSGAIIARSBX presentes na plataforma de otimização PlatEMO acoplada ao programa de análise de hélices JAVAPROP, além do acoplamento de um código de análise estrutural, foram realizadas otimizações para diferentes objetivos. Esse conjunto de elementos foi adicionado ao PlatEMO como um problema e batizado de OptProp. Inicialmente, foram realizadas análises levando em conta apenas os parâmetros adimensionais das hélices, através de sete diferentes problemas de otimização multiobjetivo para dois diferentes grupos motopropulsores. Em seguida, é realizada uma otimização que busca a minimização da potência requerida para dois diferentes pontos de voo e uma hélice é selecionada da frente de Pareto obtida. Com tal hélice selecionada, busca-se uma otimização operacional para uma determinada missão através da variação da velocidade rotacional do conjunto motopropulsor. Em todas as otimizações são consideradas restrições geométricas e, na otimização operacional, é utilizado também restrições estruturais através de frequências naturais e diagrama de Campbell. Foram encontrados economias de energia próximas de $1,4\%$ após a otimização operacional.

Palavras-chave: hélices, otimização, aerodinâmica, desempenho, BEMT, CFD, análise estrutural, algoritmos evolucionários

ABSTRACT

Currently, concerns about energy efficiency, sustainability, and the environment are growing, as proposed by the UN through The Global Goals (Goal 9 - Industry, Innovation and Infrastructure), and the search for new, more efficient, and cleaner solutions is notorious in all engineering fields. With the advancement of new manufacturing techniques, discovery and development of new materials, and expansion of computational capabilities, new opportunities for study in the field of aeronautical engineering arise. The present work proposes the elaboration of a new methodology to be used in the design and optimization of propellers, as well as the algorithms and couplings necessary for its accomplishment. During the work, a search was made for aerodynamic profiles, and a database was created with about 1500 of these. Such profiles had their coordinates standardized and refined. All airfoils were analyzed using panel methods through the XFOIL code. Using the evolutionary algorithms AGEMOEA, ARMOEA, MSOPSII, NSGAII, and NSGAIIARSBX present in the PlatEMO optimization platform coupled to the propeller analysis program JAVAPROP, in addition to the coupling of a structural analysis code, optimizations were performed for different objectives. This set of elements was added to PlatEMO as a problem and named OptProp. Initially, analyzes were carried out taking into account only the dimensionless parameters of the propellers, through seven different multi-objective optimization problems for two different powertrain groups. Then, an optimization is performed to minimize the power required for two different flight points and a propeller is selected from the Pareto front obtained. With such a propeller established, operational optimization is sought for a given mission by varying the rotational speed of the system. In all optimizations, geometric constraints are considered, and, in operational optimization, structural constraints through natural frequencies and the Campbell diagram are also used. Energy savings close to 1.4% were found after operational optimization.

Key-words: propellers, optimization, aerodynamics, performance, BEMT, CFD, structural analysis, evolutionary algorithms

List of Figures

List of Tables

Contents

1 Introduction

This opening Chapter will introduce the reader to the most important components of this work. In the following Sections, the reader will be introduced to the motivations for carrying out this work, to the historical context of the development of propellers, to the current tools for their analysis, to the bibliographic review of references used, and also to the objectives that this work aims at.

1.1 Motivation and Contextualization

This section will present a historical context and in which context the thesis was elaborated.

1.1.1 Historical Review

Propellers are rotating devices that can work for two distinct and, in a way, opposed objectives; in the first, the propeller is coupled to a motor that is responsible for driving it. Its rotation is responsible for generating thrust and moving the system where it is coupled. This is the case used in aeronautics in general: planes, helicopters, UAVs, Drones, and so on. This configuration is also used for marine vehicles, such as boats, ships, and submarines. For the second objective, the propeller is driven by the wind and coupled to a system capable of transforming its kinetic energy of rotation into another type of energy that is of interest to the user. Historically, this operating paradigm has been used in windmills and is currently used in wind power plants. These two systems can be viewed side by side in Figure 1.

Figure 1 – Mill and wind farm - Withdrawal of `https://pt.wikipedia.org/wiki/Energia_eólica` (available on 06/28/2023).

The present work is focused on propellers for aeronautical purposes. According to Bass [19], in the second half of the 18th century applications of propellers to airships began, although very little was known about their principles. A 23-foot (7.0104 m) diameter propeller, coupled to a 9hp (6.711kW) engine, was used on the La France airship in 1884. In the early 19th century, a considerable number of experiments were carried out to investigate how propeller characteristics, such as the number of blades, influenced its performance. Propellers were essential for the development of the first airplanes, aircraft heavier than air, being used by Santos Dumont and the Wright brothers.

At the advent of the First World War, variable pitch propellers were created, since the aircraft's performance was of great importance in battles. In Figure 2, a propeller of this type is represented.

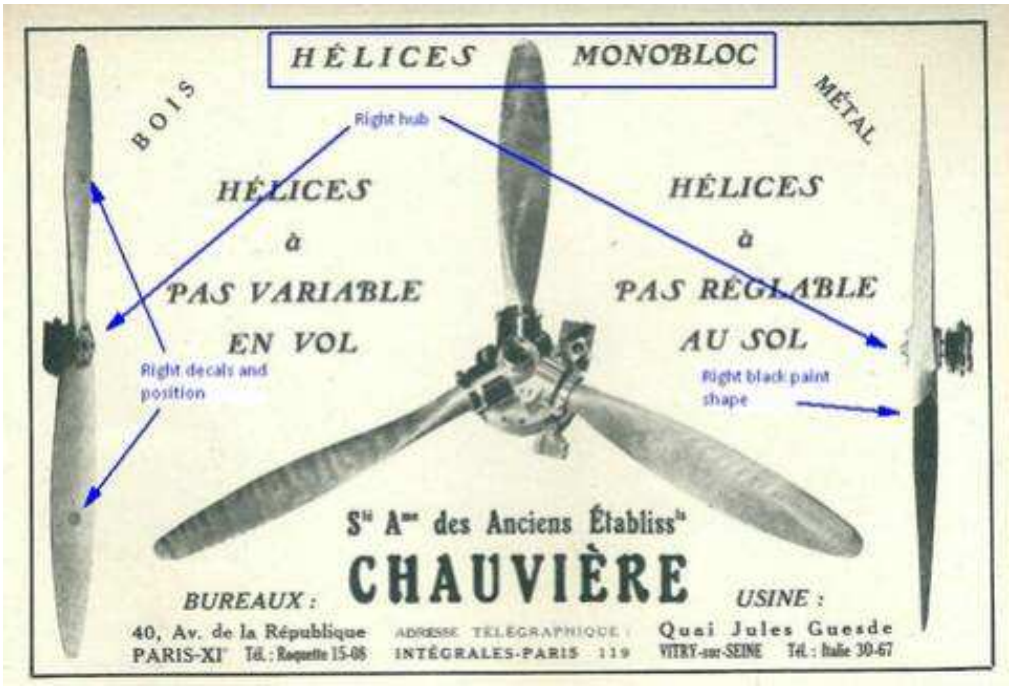

Figure 2 – One of the first propellers with variable pitch, developed in 1908 by Chauvière - Withdrawal of `https://i.servimg.com/u/f38/14/14/01/64/tm/1936_i10.jpg` (available on 06/28/2023)

In 1939 [19], the first duralumin propellers were developed, replacing the magnesium alloy propellers, due to the search for weight reduction. The wooden propellers also had their quality improved, since the quality of the wood itself, at that time, was superior to the wood of yesteryear. After the second half of the 20th century, advances in aerodynamics and computational techniques were responsible for creating a new range of propellers far superior in performance and reliability characteristics. Currently, new optimization techniques, computational fluid dynamics, and the development of new materials, such as composites, are increasing the performance of propellers.

UAVs [20] have been in use since the First World War and currently operate for a number of different purposes: surveillance, special operations, military operations, climate and agriculture monitoring, and even entertainment. Propellers are a considerable part of the performance of a UAV. The aerodynamic and acoustic performance of propellers for UAVs has been widely studied [21]. The UAV Elbit (USA), developed for monitoring civil airspace, is shown in Figure 3.

Figure 3 – UAV Elbit - Withdrawal of `https://www.ynetnews.com/PicServer5/2018/07/11/8651518/8651513199690640360no.jpg` (available on 06/28/2023)

1.1.2 GCEME Group and EMBRAER - FAPEMIG research project and FEC at Mälardalen University

This doctoral thesis, as well as its author's master's thesis, is integrated with the activities of the Electromechanical Conversion Group (GCEME) of the Federal University of Juiz de Fora (UFJF). The GCEME is a group formed mainly by researchers from aeronautical, mechanics, civil, and electrical engineering. Its main activity is the development of research related to energy efficiency of different systems.

The research group approved in the FAPEMIG Public Notice 06/2017- Research in the area of the aeronautical sector - partnership FAPEMIG - EMBRAER S.A. the project entitled "Assembly of a Test Bench for Aeronautical Propulsion Hybrid-Electric". The project, already completed, proposed the planning and construction of a static test bench for electric hybrid aeronautical propulsion in series configuration for the establishment of a multidisciplinary knowledge base of the various areas involved. Among these areas, power electronics, electronic monitoring systems, data acquisition, control, management and supervision, design of electric motors and engines, propeller aerodynamics, and mechanical design are mentioned.

A schematic diagram of the proposed hybrid propulsion system can be seen in Figure 4. The item PRP refers to the propeller that is coupled, in sequence, to the electric generator EG, to a torque wrench, and to the electric motor. The shaft part between the

electric motor EM and the electric generator EG is supported by a support structure. The entire system is static and all its components works in an integrated manner.

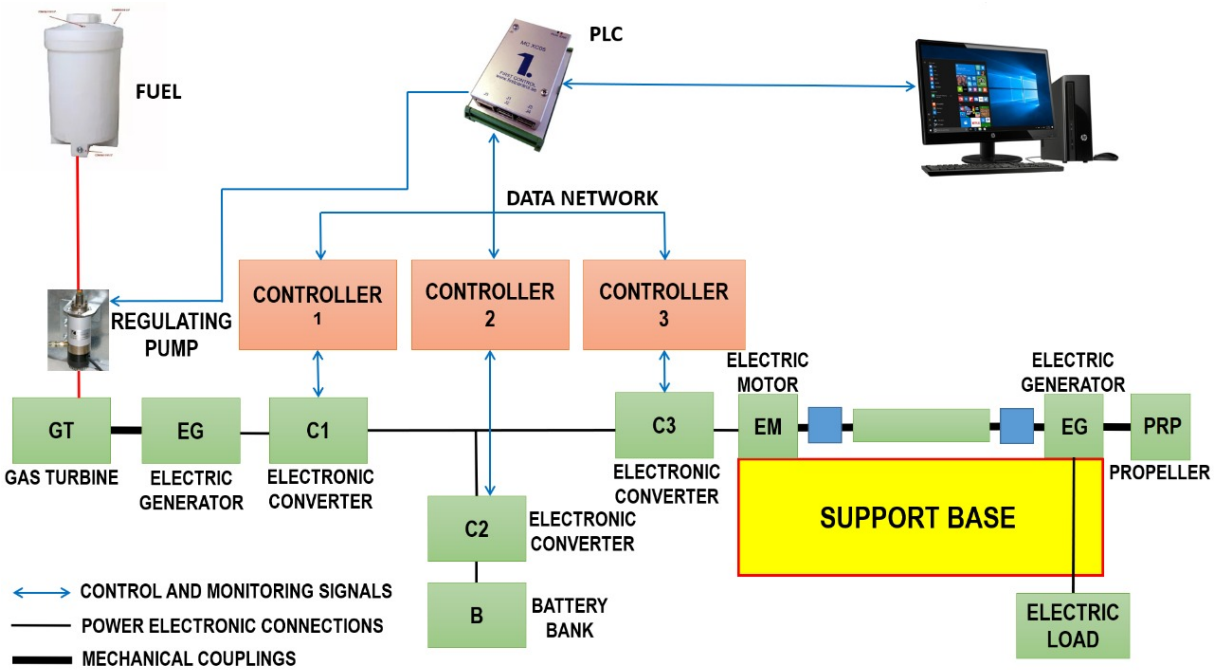

Figure 4 – Schematic diagram of the hybrid propulsion system

One of the activities foreseen in the GCEME project is the aerodynamic study of the propeller coupled to the system. When the bench is in operation, the thrust, torque, rotation, and power supplied by it will be sampled and evaluated under different conditions during the tests.

This was the motivation for the student's master's thesis, in which the main subject was the study of models to measure the aerodynamic coefficients of the propeller. From the knowledge achieved, it was possible to propose the present research project.

Part of this doctoral thesis was developed at the Future Energy Center (FEC) at Mälardalen University, Sweden, with the guidance of Professors Konstantinos Kyprianidis and Stavros Vouros. The research conducted in FEC aims to address the upcoming energy and environmental challenges by exploring and creating methods and systems that enhance resource efficiency and embrace digitalization in the shift towards renewable energy. Aviation has significant environmental impacts, since aircraft engines produce emissions that give rise to important environmental concerns regarding their global impact and their effect on local air quality at the ground level [22]. Through collaboration with industry and society, FEC strives to develop energy systems that are efficient, adaptable, and innovative, while minimizing their adverse effects on the environment and reducing emissions. This crucial research plays a tangible role in providing solutions to the pressing

global challenges of our time. FEC conducts research in the main following areas:

- Renewable energy with a focus on affordable, reliable, sustainable, and modern energy
- Resource efficiency with a focus on energy efficiency, low emissions, and nutrient and material recovery
- Digitalization with focus on energy efficiency and environmental performance

1.2 Objectives and contributions

The main objective of this work is to propose an innovative methodology for the design of propellers through multi-variable and multi-objective optimization using evolutionary algorithms. This methodology proposes propeller optimization in terms of aerodynamic performance parameters using geometric and structural constraints. It is proposed that the methodology be able to present several propeller choices to the aeronautical designer through visualizations of Pareto curves and surfaces that, allied to their own experience, will make the propeller design a discipline capable of making them more energy efficient.

Currently, most designers are satisfied with choosing general propellers indicated by engine manufacturers. However, this paradigm begins to change as the manufacture of propellers has been a discipline of great interest, innovation, and evolution. Therefore, having new tools for the manufacture of propellers, the designer will also look for new ways to design custom propellers. Generally, the selection of the propeller is conditioned to the expected aerodynamic performance of the aerial vehicle, the engine characteristics and engine control propeller noise and vibrations, the installed weight of the propellers, the influence of the propellers on flying qualities, and the structural limits imposed by the layout of the aircraft [23]. To achieve the defined objectives during the conceptual design stage, the propeller features are mainly associated with some important aspects, such as the blade shape (i.e, the plan form of the blades, the airfoil shape, and the twist along the blade), the number of blades per propeller, and the propeller diameter [23].

In this regard, several researchers are looking for alternatives to propeller design and optimization that will be cited in the bibliographic review Section 1.4. The present work is dedicated to this topic of study.

The proposed methodology will be covered in Chapter 3. It uses several tools already consolidated in the literature, some of which needed to be modified to work according to the proposed objectives. At other points, it was necessary to create new codes to complete tool gaps in the methodology. Such adaptations and conceptions of new codes will be properly presented throughout this work.

As partial and specific objectives of the present work, we mention:

- Creation of a database of aerodynamic profiles and further refinement of these;
- Extension of the aerodynamic profile database through its analysis using the panel method in terms of aerodynamic coefficients and geometry characteristics like area and moments of inertia;
- Coupling the database to propeller aerodynamic performance analysis tools;
- Coupling structural analysis tools to the analysis algorithm;
- Expansion of the analysis algorithm through its coupling with genetic optimization algorithms;
- Development of objective functions and constraints for application of test cases;
- Propeller optimization study through dimensionless aerodynamic parameters;
- Propeller optimization for a given conventional mission;
- Mission operational optimization through multiple rotational propeller speeds and comparison with fixed rotational speed;
- Use of structural vibration constraints in operational optimization through Campbell Diagram.

As can be seen in the subsequent literature review Section (1.4), the present work takes the courses of the aforementioned research, using tools already extensively tested such as the BEMT methods and evolutionary algorithms. However, new points of interest are added to the field of studies, such as the use of new multi-objective functions, with structural and geometric constraints, and, unlike the studies analyzed, is added to the discussion the importance of selecting appropriate aerodynamic airfoils through an extensive database with generated data from airfoils available in the literature. The proposed method, as well as other works, starts from the importance of designing a propeller considering which motor-propulsion group it will be used in and not just in the optimization of an isolated propeller. This work also uses the developed method to generate a propeller for a typical mission. Among the various propellers generated through optimizer algorithms, one of them is chosen to carry out an operational optimization, aiming to further reduce the required flight power levels and, therefore, reduce the consumed fuel and the emission of pollutants. In addition, the work also studies the relation between the energy required in a conventional mission with three different rotational speeds of the propellers against the energy required in multi-rotational speeds situations.

1.3 Propeller Performance Analysis Tools

There are different methods in the literature for propeller design and analysis based on different levels of sophistication. In general, the main objective of these methods is to evaluate the performance of these elements in terms of thrust, torque, power, and efficiency. They describe themselves, very concisely in this Section, some of these methods.

1.3.1 Analytical models - Actuator disk and blade element theory

First, the analytical model is known as the actuator disk theory is mentioned (or the amount of linear motion), and the blade element theory (BET), as well as hybrid formulations of these two theories (Blade Element Momentum Theory - BEMT).

The first, developed for marine propellers by Rankine [24] and Froude [25], follows the basic principle of operation of a propeller, which is to supply the air that passes through it a certain amount of movement, taking advantage of the reaction generated to accelerate a body against air displacement.

Tracing a brief history, a great contribution to the development of rational theories for the study of propellers came from the work of Prandtl. The latter developed, to incorporate the effects of circulation to the wings of airplanes, the theory of the lift line, which was later assimilated into the propeller theory. Betz in 1919 showed that the loading distribution for propellers slightly loaded and considering the condition of minimum energy loss, that is, with constant vorticity along the blade's mat, cause the detached vortexes to form a regular helical mat that moves without deforming in the propeller mat [26, 27, 28]. The idea of sectioning the blades into infinitesimal elements and integrating the elementary forces to obtain the global aerodynamic parameters was first proposed by Drzewiecki [29]. In 1935, Glauert presented a methodology that incorporates two basic models: Actuator Disk Theory and Blade Element Theory [30]. In 1948, Theodorsen proved that it is possible to obtain the distribution of the lift coefficient in the blades for different loading levels by analyzing the helical vortex sheet on the belt away from the propeller when considering the contraction of the belt [31]. It is worth mentioning that Theodorsen's work is a milestone in propeller theory.

It is noteworthy that these formulations do not demand a lot of computational resources, but they are quite limited when more complex analyzes are desired.

1.3.2 Models in computational fluid dynamics

At the top of the hierarchy are models that consider viscous flows, three-dimensional, incompressible, and/or compressible. These flows are described by Navier-Stokes partial differential equations. The simulations of this nature are called computational fluid dynamics (CFD) and are made with the aid of computational resources.

In CFD, Navier Stokes equations are solved using discrete methods, the most traditional of which are the finite element method (FEM), the finite difference method (FDM), or the finite volume method (FVM). Generally speaking, these methods transform the partial differential equations and their initial and boundary conditions in an algebraic system of equations.

The main concerns of the aforementioned methods are to use specific algorithms that address the inherent problems of discretizing Navier Stokes equations. Among these problems, the non-linearity of the advective term stands out, the pressure-velocity coupling problem, the interaction problems between the fluid and the structure in motion, and, according to the Reynolds parameter, the insertion of turbulence that contemplate the various temporal and spatial scales.

In addition to these questions, for the object of study of this research, the issue of compatibility of interfaces also stands out. For the execution of simulations involving rotating elements, as is the case of the propeller, it is necessary to define at least two different domains; one is stationary, the other rotating. For the simulation to be possible, it is necessary to make the interfaces common to different domains compatible. Due to rotation, it becomes necessary to account for the relative movement of multiple rotors and stators, either by direct topological changes in the mesh or by geometric simplifications [32].

CFD, due to its complexity, requires appropriate computational resources due to high processing costs. In addition, for the practice of engineering, the cost of the simulation must be low enough to allow detailed studies of conditions outside the design, optimization of the geometric shape, robust design studies, etc [32].

The literature also provides hybrid models resulting from the combination of the models mentioned above. Malkie et al. [33], for example, proposed a CFD-BEMT coupled model to evaluate the performance of a multiple tidal stream turbine. Bahmari et al. [34] presented a multi-fidelity shape optimization of the hydraulic turbine in which a surrogate model permits to select, among all feasible solutions, a few promising solutions which are transferred to the high-fidelity phase to warrant robustness to the simulations.

However, when compared to the other approaches, the advantages of its versatility and flexibility, as it allows the solution of some problems that mathematically do not have an exact analytical solution as well as enables this study to be applied to geometries and often complex cases. This is the main attraction for the use of these tools, and it is in this context that this research is inserted.

1.4 Literature Review

This Section presents some work on propeller performance consulted during the research. Emphasis is given to work in propeller analysis and optimization, BET and BEMT models, propeller structural analysis, and CFD for the most varied applications. Many, as can be seen, corroborate the methodology used in the research.

Firstly, in works that use analytical models, such as the theory of the actuating disk and the theory of the blade element, the valuable contribution of Wald [26] stands out. This author makes a compilation of the main works that contributed to the improvement of this methodology, which, up to the present day, is still used in projects and research for providing reliable results, at a low computational cost.

Several works are found in the literature that combines aerodynamic concepts with optimization platforms. Optimization problems, in turn, can be developed to meet a single expected objective or, promisingly and interestingly, multiple objectives, many of them conflicting.

Some of these efforts are concentrated on airfoil shape optimization. For example, multi-objective optimization problems concerning a class of viscous transonic airfoils are discussed by Pulliam et al. [35], presenting a comparison between a genetic algorithm and adjoint methods. The results show the optimization trade-off between drag and lift as conflicting objectives. Multi-objective design optimization for a three-element airfoil consisting of a slat, the main wing, and a flap was carried out by Kanazaki et al. [36]. The conflicting objective functions were the lift coefficient at the landing and near stall conditions, both to be maximized simultaneously. The genetic algorithm was used as the search engine.

Parashar et al. [37] discussed the self-organizing maps (SOM) and design selection for the multi-objective design of airfoils. The optimization of an airfoil is performed concerning lift and drag coefficients, taking into account the uncertainties in Mach number and angle of attack. A methodology for the multi-objective optimization of natural laminar flow airfoils using a kriging-assisted multi-objective genetic algorithm was proposed by Cameron et al. [38]. The design methodology was able to find a set of Pareto optimal wing sections showing low drag and extended regions of laminar flow at the cruiser and loiter flight conditions. Benini et al. [39] presented a multi-objective and multipoint optimization problem analyzing a multi-element airfoil used in high-lift devices searching for optimal shape setting slap and flap as design variables. The objective is to improve its aerodynamic performance at take-off and landing operations.

Ribeiro et al. [40] employed single and multi-objective genetic algorithms with an artificial neural network as a surrogate model, coupled with a CFD solver, to optimize airfoil shape. In [41], a multi-objective optimization based on kriging models was investigated

to reduce the airfoil trailing edge noise while maintaining the aerodynamic performance. Koziel and Leifsson [42] presented a multi-objective design of transonic airfoil shapes using a multi-objective evolutionary algorithm (MOEA). The proposed method adopted a fast surrogate model of the airfoil with kriging interpolation of low-fidelity CFD airfoil simulations. Kovačević et al. [43] provided an artificial intelligence method (genetic algorithm) to optimize the rotor blade airfoil. This research was followed by aerodynamic analysis via BEMT and CFD, structural analysis, and experimental tests in a manufacturing composite propeller.

Regarding propeller optimization, Chang and Sullivan [44] and Cho and Lee [45] proposed a single-objective optimization of the pitch and the pitch and chord, respectively, of propeller blades. Both intended to maximize the propulsive efficiency under the constraint of constant power consumption. The VLM was used to obtain the aerodynamic parameters.

Dorfling and Rokhsaz [46] presented a procedure for deriving the Euler-Lagrange equations for propeller blade twist optimization, searching to maximize efficiency. The propeller aerodynamic performance model was the BET, coupled with the vortex theory of Goldstein [47]. Schatz *et al.*[48] proposed a multi-criteria optimization of an aircraft propeller considering manufacturing in carbon fiber-reinforced polymers.

Using BEMT and CFD approaches, Toman *et al.* [49] proposed a blade shape single-objective optimization of an aircraft propeller using space mapping surrogates, in which the propeller blade shape optimization was discussed, searching for the maximum aerodynamic efficiency with a minimal number of high-fidelity model evaluations. Alshahrani [50], using the BEMT model, investigated the variable pitch propeller and the influence of the number of blades, formulating an optimization problem of a propeller design for small hybrid-electric propeller aircraft.

The multi-objective aeroacoustic optimization of an aircraft propeller was discussed by Pagano *et al.* [51] considering the noise emission at take-off and the cruise efficiency. A CFD approach, with a suitable physics-based surrogate model based on the complete potential equation that can predict the inherently unsteady flow field on a helicopter rotor at different flight conditions, was used.

Marinus *et al.* [52] adopted a differential evolution algorithm to perform a multi-objective optimization of transonic propeller blades combined with CFD simulations. The design variables were the control points of B-spline parameterizations of the radial distributions of the sweep, twist, chord, and thickness and the points controlling the shape of the two airfoils used to manufacture the blade. The propeller power and the propeller plane were the objective functions, both in the cruise and take-off/landing conditions.

MacNeill and Verstraete [53] presented a multi-objective optimization of propellers

for a hybrid electric fuel cell-powered unmanned aerial system. A multidisciplinary optimization method used an empirically correct electric motor model, an extended BEMT theory aerodynamic model, and an Euler-Bernoulli beam structural model. Pareto fronts showed the trade-off between the propeller and motor efficiencies for optimal endurance and range conditions for the aircraft. In addition, Pareto optimality between aircraft endurance and both climb-rate and maximization of flight velocity was investigated.

Pareto sets were obtained by Slavik *et al.* [54] to find the optimal propeller, using the vortex blade theory. The objective was to find the best performance with a fixed propeller (i.e., high maximal horizontal and cruise speed, short take-off, and high rate of climb).

This brief review highlights several researchers' contributions to multi-objective optimization of various thermodynamic systems. Ganesan *et al.* worked on a Gas Turbine - Absorption Chiller system optimization with many objectives [55]. Gul *et al.* proposed a multi-objective optimization approach for industrial gas turbines fueled by natural gas [56]. Sadegui *et al.* analyzed the effects of thermophysical and thermomechanical recovery in a combined gas turbine and organic Rankine cycle system based on the methane steam reforming process [57]. They used a genetic algorithm for multi-objective optimization. Ding *et al.* proposed a multi-objective optimization for a microgrid's integrated renewable, power-to-gas, and solid oxide fuel cell/gas turbine hybrid system [58].

In the field of experimental tests, we first mention the work of Witkowski [59] who designed and rehearsed the propeller in a wind tunnel they called Purdue. Also, noteworthy are the works of Brandt and Selig [60] and Deters *et al.* [61]. In the latter, there is a detailed description of the tests and results performed for different propeller models, which include propellers designed and tested by the authors themselves. On the website https://m-selig.ae.illinois.edu/props/propDB.html it is also possible to obtain detailed information on the experimental campaigns, geometric models, and results of the propellers tested by the team.

As works related to the keywords: propeller analysis and optimization, BEM and BEMT models, propeller structural analysis, and CFD, the following stand out:

- Nouri *et al.* [62]: the authors of this work seek the optimization of a marine counter-rotating propeller through genetic algorithms and the Kriging method. Through a coupling between the Kriging method, the genetic algorithm, and a CFD tool, it is possible to determine the hydrodynamic performance of the propellers and execute the optimization process. Using an iterative process, the geometries are analyzed, and the results are added to the initial population. The results obtained by the authors were considered efficient, and the algorithm developed can be used as an optimization package for marine propellers.

- Lee and Lin [63]: this work designs a composite material propeller that works in different operating ranges. The propeller deformation is determined according to the fiber orientation of the material used. Through structural calculations using the finite element method and CFD, it is possible to determine the deformation experienced by the propeller, as well as its aerodynamic performance. Through genetic algorithms, it is possible to determine the best stacking arrangement for the propeller.

- Gur and Rosen [64]: in this research, a new propeller design method involving aerodynamics, structural, and acoustic analysis was proposed. Through the combination of several analysis tools, three different optimization schemes are proposed. The developed method, which can be applied to the propeller design of ultralight aircraft, is compared to the classic Betz's condition method and has good performance. The method shows the importance of considering the entire propulsion system and not just the propeller.

- Hallak *et al.* [65]: this work applies methods ranging from low-fidelity to high-fidelity methods. The authors used a 14×7 APC propeller to test these methods. This propeller was experimented in a wind tunnel and later its geometric modeling was performed on a 3D scanner. The BEMT and CFD methods were used to analyze their aerodynamic characteristics. In CFD, two different methods were used: Frozen Rotor (FR) using ANSYS-CFD and Arbitrary Mesh Interface (AMI) using OpenFOAM. The turbulence model used was the $k-\omega\ SST$ and the influence of the transition laminar-turbulent boundary layer model was also investigated through the Gamma Theta transitional method. When comparing the computational tests with the physical experiment, it was observed that the analysis method has a strong relationship with the Reynolds number. At low speeds, the BEMTs approached physical experiments. BEMT linear model overpredicted the power and efficiency for a high advance ratio, while BEMT with three-dimensional flow equilibrium presented consistent results with a low computational cost. On the other hand, the CFD-AMI model shows better results for higher advanced ratio velocities, but is computationally more expensive. The CFD-FR model maintains a constant pattern of error that, in the analysis of efficiency, did not compromise the results.

- Sodaj and Kosel [66]: the objective of this research is to demonstrate that the propeller design based on BEM models can adequately provide distributions of important amounts of aerodynamic performance, such as thrust and power distribution. To know how valid these distributions are, CFD analysis is used. Surprisingly, the authors are faced with better matches of the BEM method to the experimental data than those obtained through CFD. The authors also suggest that, according to the results obtained in the study, there is potential for the use of BEMs in fluid-structure

predictions and believe in coupling these methods to structural solvers in order to create a rapid-design analysis tool for propellers and other rotary-wing devices.

- Gaggero *et al.* [67][68]: through the combination of a Boundary Elements Method algorithm, a viscous solver based on a RANSE (Reynolds Averaged Navier–Stokes Equation) approach, 3D parametric description of the propeller blade and a genetic algorithm, the geometry of a new propeller is generated to improve propulsive efficiency and improvements related to the cavitation phenomenon. The created algorithm works through engine-propeller matching that, when a new propeller is defined, the maximum possible speed is identified as well as the engine's operating point. A group of optimal propellers is obtained, and their results are validated through the BEM method. Through the complex flow fields generated, one of the optimal geometries is chosen. The improvements observed in a cavitation tunnel and a substantial increase in maximum speed in tests carried out at sea using high-speed craft prove the reliability of the design process.

- Cho and Lee [45]: in this work, an optimization technique was developed to determine an optimum propeller shape considering the efficiency improvement. The method satisfies the constraints of keeping the power coefficients and the activity factor constant. A lifting line theory (vortex lattice method) and a surface theory lifting (panel method) are used to calculate the aerodynamic efficiency parameters of the propeller. The authors used chord length and twist angle as design variables. The optimization is validated by comparing the results with other numerical schemes. Optimizations are proposed for different propellers, such as the SR-3 and SR-7.

- Jiang *et al.* [69]: the authors of that work apply Non-dominated Sorting Genetic Algorithm-II (NSGAII) to the design of propellers and couple the method of finite elements with the method of panels to perform fluid-structure interaction. In the multi-objective optimization methodology, objectives related to efficiency, unsteady force, and mass were used in addition to certain constraints. The effectiveness and robustness of the method are validated when executing the code with different initial values and converging into similar results. The authors believe that the proposed method is a promising tool for the future of more efficient propeller designs.

- Herath *et al.* [70]: this work uses an optimization scheme using a cell-based finite element method (CS-FEM) combined with a genetic algorithm. The optimization algorithm and the codes developed in this work were implemented under a variety of parameter configurations and compared to the need to obtain a propeller with passive pitch variation ideally. Recommendations are also presented for the required thickness of the propeller blade to achieve the optimal performance of the flexion-torsion coupling without resulting in large tilt deformations.

- Stuermer [71]: a series of CFD simulations are conducted by these researchers, with the main purpose of investigating the effects of other surfaces, such as airplane fuselage, axle, and wing, on the efficiency of the system. Basically, two configurations were analyzed and compared: an isolated propeller with an axisymmetrical nacelle and another propeller with a symmetrical axis nacelle mounted in the middle of an untwisted wing with a symmetrical airfoil. The simulations were carried out in the DLR TAU program, as a Spalart Alamaras turbulence model (equation model). The compatibility of the surfaces of the rotating and stationary domains is done through a technique they call Chimera, which is based on the use of several grids that have overlapping regions and where the variables required in a limit node are obtained by interpolations from the values of surrounding cells.

- Beaudoin and Jasak [32], Jasak and Beaudoin [72]: the importance of these articles is in the implementation of techniques for handling interfaces, then called GGI (Generalized Grid Interface), which allows the coupling of the rotating and stationary domains. The presented algorithm presented was developed for the OpenFOAM platform. The main advantage of the presented technique is that there is no need to adjust the mesh topology at the interface between two meshes. Instead, a set of weighting factors is assessed to properly balance the flow at the GGI interface.

- Park [73]: this study refers to the structural and aerodynamic designs of propeller blades for a turboprop aircraft. The structural design contemplates the aerodynamic loads that cause flexion, torsion, and shear, in addition to vibrations. Aerodynamic loads are obtained through CFD simulations in the ANSYS-Fluent program, RANS -SST turbulence model. The 8-blade propeller model is studied using the MRF technique (Moving Reference Frame). An isolated, flexible paddle is analyzed using a fluid-structure interaction package to verify the possibility of the occurrence of vibrations induced by the flow.

- Mohamed [74]: the object of study of this work is wind turbines, and its main objective is to reduce the aeroacoustic effects caused by the rotation of the blades. The aerodynamic effects to assess the noise generated by the blades are obtained by means of CFD simulations in the ANSYS-FLUENT program, with URANS k - ε (Unsteady Reynolds Averaged Navies Stokes) turbulence model and SMM technique (Sliding Mesh Model) to allow the blades to move.

- Kutty and Rajendran [75]: in this work, the CFD is applied to a small-scale, fixed-blade APC propeller (advanced precision composites), APC 10 $\times$ 7. The commercial program ANSYS-Fluent, model of turbulence k- ε, MRF technique to consider propeller rotation. The presented modeling presented good results in terms of thrust, power, and efficiency.

- Mizzi *et al.* [76]: this work presents an optimization methodology in propellers of marine vessels through CFD analysis. The commercial program Star-CCM, turbulence model RANS k - ω was used, and, for the movement of the system, the MRF models.

- Chirico *et al.* [77, 78]: investigating the aeroacoustic effects caused by the rotation of the propellers, in a model coupled to the propeller and fuselage. The main objective is the coupling to an optimization platform aiming at a comfortable acoustic model for users. To this end, a particular CFD code, three-dimensional modeling, and an arbitrary Lagrangian algorithm is used to allow border movements. Apply URANS turbulence models and a hybrid of these with LES formulations (Large Eddy Simulation).

- Król and Tesch [79]: this work is dedicated to the study of marine vessel propellers. It uses the OpenFOAM platform, k - ω turbulence model, and an MRF module. The results are validated with the experimental ones in a water tank whose experiments were carried out by the authors themselves.

- Sodja *et al.* [80]: this work investigates the effects of fluid interaction of flexible propeller blades, using two approaches: one uses the BEMT method coupled to structural dynamics models, while the second uses CFD coupled also to structural dynamics models. The CFD simulations were carried out in ANSYS-CFX, with a k - ε turbulence model and rotating reference frame techniques, a simplification of the MRF for the rotation-only movement. An important conclusion of this work, which can serve as a reflection for future work, is that the rate of advance becomes an invalid measure of similarity in the case of flexible propeller blades and the behavior of such blades can change significantly with changing operation conditions, keeping the feed rate constant.

- Hoyos *et al.* [81]: this paper proposes an aero-structural algorithm to reduce the energy consumption of a propeller through a propeller design method coupled with Particle Swarm Optimization. The prediction of aerodynamic performance is performed using the Blade Element Momentum Theory tool, which in turn is fed with aerodynamic data of airfoils obtained from XFOIL. Data is validated in OpenFOAM. A model based on the Euler-Bernoulli beam theory, validated through Finite Element Analysis, is also used. A case study is conducted where chord and pitch distributions are compared to those predicted by vortex theory. Tests were conducted in a wind tunnel to validate the use of the algorithm by comparing them with CFD and XFOIL optimal propellers. Finally, the optimal CFD propeller is compared with a commercial propeller of the same diameter, pitch, and operational conditions, showing greater thrusts and efficiency.

- Zhang *et al.* [82]: the authors propose the use of the adjoint method to solve the Navier-Stokes equation and optimize the aerodynamic configuration in order to increase the precision and efficiency of a propeller design. The wing-body configuration was used to validate the basic solver and the rotational effects were added to the model through the moving reference frame method, which is able to increase the accuracy and efficiency of the model. The optimization was performed in order to maximize the thrust coefficient based on the gradient solver. The torsional moment of the wing-root was used as a constraint. The distribution of twist angles and chord length and the blade airfoils were selected as design variables. The influence of twisted angle distribution was studied, and the results demonstrated an optimal location according to common knowledge that high twisted angles lead to high wing loads. The chord length distribution, which changed the contour line of both leading and trailing edges of the blade, improved the propeller performance by reducing the cross-flow. The optimization of the blade's airfoils was also carried out, generating a 3.28% enhancement of thrust efficiency.

- Yang *et al.* [83]: in this paper, the authors used the discrete adjoint method to optimize a cluster of airfoils in a three-dimensional state. Through parametric perturbations and flow pattern reconstruction method, optimizations were performed in the twist angle and chord length distribution. It was found that the precision of the method is consistent with Computational Fluid Dynamics and with experimental data, indicating that the method combines high fidelity and low computational costs, accurately quantifying the influence of complex and three-dimensional characteristics of the flow, and providing a reference for the propeller design of a high altitude long endurance UAV.

- Koyuncuoglu and He [84]: this work is focused on the aerodynamic efficiency of electric vertical take-off and landing (eVTOL) aircraft. The aerodynamic efficiency of propellers and wings has a great influence on the overall performance of this type of aircraft, however, these elements are usually considered separately. The authors propose a method to simultaneously optimize the wing-propeller assembly. Computational Fluid Dynamics solvers were used to simulate the two elements through separate meshes, and then the adjoint method was employed to compute the derivatives and couple them with a gradient-based optimization algorithm. The objective function of the optimization used was the propeller power consumption and the design variables were the wing shape and twist, propeller center, twist, chord, outer radius, and rotation speed. Constraints related to force balance and geometric properties were also used. A power reduction of 18.3% was obtained, and all constraints were met.

- Geng *et al.* [85]: the authors of this work carried out an optimization considering

aerodynamic and aeroacoustic performance simultaneously using artificial intelligence. A Deep Neural Network was selected to map the non-linear relationship between the aerodynamic and aeroacoustic parameters, and the optimization was performed through the implementation of a deep reinforcement learning algorithm called Deep Deterministic Policy Gradient (DDPG), to which was also added a DNN-fidelity based surrogate Multi-Model (TL-MFDNN) with Transfer Learning between pre-trained and re-trained processes. When comparing the optimizations with TL-MFDNN surrogate model based and DDPG using direct Computational Fluid Dynamics simulation, the computational cost was reduced by 77.3% and the optimized propeller had a maximum noise reduction of 1.69dB with negligible performance reductions.

- Guan *et al.* [86]: the authors used an integrated method combining Fluid-Structure Interaction (FSI), Design of Experiment (DoE), and Non-dominated Sorting Genetic Algorithm II (NSGAII) to improve the efficiency quality of marine propeller design. The radial distribution of the skew, chord length, pitch, and camber were used as design variables, guaranteeing the thrust coefficient and structural strength of the propeller. Finally, a propeller with higher efficiency, higher thrust, and safer structure was obtained, showing that the design method is suitable for practical engineering applications.

- Doijode *et al.* [87]: in this work, the authors present a method to improve the computational cost of optimizing marine propellers by reducing the number of evaluations using machine learning. The search is directed toward three types of clusters: the first with designs with performance of interest and low cavitation, the second with performance not of interest and high cavitation, and the third with designs whose performance cannot be determined using the Boundary Element Methods. For simple cases of single-optimization to maximize efficiency, these clusters can be identified with unsupervised classifiers, while for multi-objective cases it is necessary to use supervised classifiers. Due to multicollinearity, classic design variables such as chord length, pitch, skew, rake, thickness distribution, and camber of hydrofoils cannot be visualized. In this way, a new orthogonal parametric model is proposed where its parameters are directly derived from the propeller blade mesh. It is expected that the orthogonal parameters have a stronger correlation with the performance predictors of Boundary Element Methods or Computational Fluid Dynamics than with the classical variables, since the blade surface mesh is used as a boundary condition to solve the governing equations. The authors demonstrate that the method performs well and that the proposed clusters can be identified after some evaluations, however, reducing the cost of optimizations results in a trade-off with the completeness of the search. A demonstration of the method is also performed on a simple fully wetted flow case of the benchmark Wageningen B-4 70 propeller with

P/D=1.0, allowing back-of-the-envelope verification and validation of our results.

- Meng *et al.* [88]: in this work, the authors point out that for wind turbines to become more efficient, the related systems need to get bigger and bigger. As the size scale increases, the natural frequencies of the blades decrease, and the influence of rotational speed increases. In this way, a comprehensive study of the centrifugal stiffening effect on the structure of the blades is carried out. The work is based on the wedge beam model and Rayleigh-Ritz method and the natural frequency variation curves are obtained through the ANSYS software. As parameters that affect the natural frequency were pointed out: blade length, stiffness-mass ratio, and aspect ratio and it was found that the centrifugal stiffening effect exerts an important impact influence on the fundamental frequency of the blade, being 10% for NREL 5 MW.

1.5 Scope

This Chapter presents the topic studied, the motivation for its study, its importance, and the objectives to be achieved.

In the second Chapter, theoretical concepts important for understanding the work will be presented. Among these topics are fundamental propeller concepts, analysis methods, and multi-objective optimization concepts.

In the third Chapter, the methodology used for the construction of this work will be presented.

In the fourth Chapter, the codes and software used for the development of this work will be presented.

In the fifth Chapter, it will be analyzed how the optimization code was developed, as well as how the algorithms were coupled.

In the sixth Chapter, the elaborated experiments and their results are presented, which are commented on.

In the last and final Chapter, the final comments will be made, as well as proposals for future work.

2 Theoretical Background

2.1 Propeller Performance

This Chapter is dedicated to describing the principles of propeller operation, its main geometric characteristics, and how it is evaluated in terms of its performance.

2.1.1 Propeller Operating Principles

An aircraft's propeller consists, commonly, of two or more blades connected to the central hub, in which these blades are fixed. When rotating, the blades "cut" the air and create an aerodynamic effect, similar to wing lift, that is, the circular displacement of the blade in the air causes a low pressure on the back of the blade, and high pressure on the face, generating thrust.

During the operation, the propeller rotates and advances in the same way as a screw. At each turn, it advances a certain distance, which is called the propeller pitch. Therefore, they are classified as fixed-pitch or variable-pitch propellers. Fixed pitch propellers are generally one-piece and with their blades fixed to the cube, forming a single piece. The variable pitch propellers have their blades installed in the hub and can be moved to change their angle.

The purpose of varying the blade angle is to maintain an optimal angle on the propeller blades, while the plane's speed varies, maximizing its efficiency. A small blade angle of attack performs well in relation to drag, but generates little momentum, while large angles have the opposite effect. The best angle blade attack is when they act as small wings, generating more lift than drag.

The propeller's function is to absorb the power produced by the engine, transmitting it to the air that passes through the propeller disk. This energy is used to accelerate the air, generating thrust force on the propeller blades. If the ability to absorb power from the propeller does not combine properly with engine power, both become inefficient.

Propeller slip is the difference between the geometric pitch and the effective pitch of the propeller. The geometric pitch is the distance that a propeller should advance in a revolution. The effective pitch is the actual distance traveled by a revolution of the propeller.

2.1.2 Geometric Features of Propellers

The geometric characteristics of a propeller can be divided into aerodynamic profile geometry and propeller geometry itself. The following Subsections will address these topics.

2.1.2.1 Airfoil Geometry

According to Anderson [89], the aerodynamic profile is the geometric shape of the propeller section. A propeller can contain only one profile over its entire length, as well as a combination of several profiles. The dimensions used to define a profile can be seen in Figure 5.

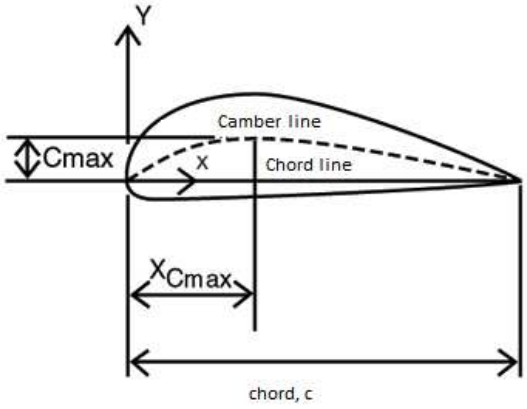

Figure 5 – Airfoil geometric dimensions - Withdrawal of `http://www.akiti.ca/NACA4Bkgrnd.html` - available on 06/28/2023

The mean camber line is the average between the upper and lower surfaces of the airfoil. The forward region is known as the leading edge, while the opposite region is known as the trailing edge. The straight line between these two regions is the chord line. The length of this line is known as the chord, c. The maximum distance between the chord line and the camber line is known as the maximum camber (C_{max}), and the position where it is found is known as X_{Cmax}. The thickness of the profile is the maximum distance between the lower and upper surfaces measured perpendicular to the chord line.

NACA (National Advisory Committee for Aeronautics), NASA's predecessor, created a four-digit system to describe numerous aerodynamic profiles. Subsequently, a five-digit system was created. The dimensions used to define a profile can be seen in Figure 5. The four digits of the aerodynamic profile are:

- 1º Digit: Maximum camber ($C_{\max}$) in percentage terms.
- 2º Digit: Maximum camber position (X_{Cmax}) in percentage terms.
- 3º e 4º Digits: Percentage thickness.

2.1.2.2 Propeller Geometry

The diameter (D) of a propeller is defined as the distance from end to end, and the radius (R) is defined as the distance between the center to one of the tips of the propeller. The chord (c) and the torsion angle (β) are defined as functions of the radial position (r) of the propeller. These parameters can be seen in Figure 6.

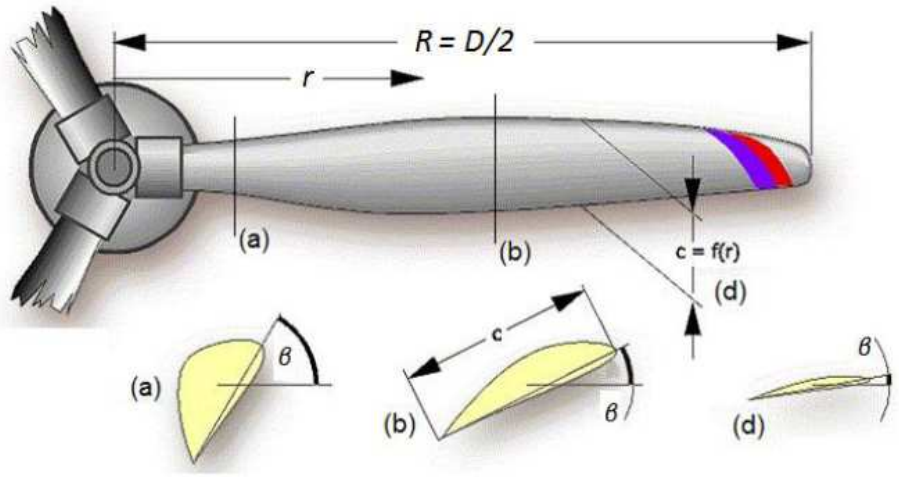

Figure 6 – Geometric parameters of a propeller - Withdrawal of `http://www.mh-aerotools.de/airfoils/prophist.htm` (available on 06/28/2023)

The pitch of the propeller is defined as the distance it advances after a revolution. Figure 7 shows the step definition.

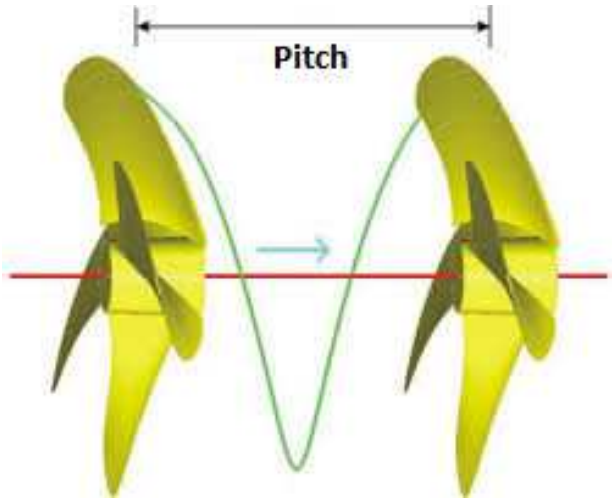

Figure 7 – Propeller pitch - Withdrawal of `http://www.propellerpages.com/?c=articles&f=2006-03-08_what_is_propeller_pitch` (available on 06/28/2023)

2.1.3 Performance Parameters

The performance parameters of a propeller are usually dimensionless. According to Brandt and Selig [60], the efficiency of a propeller is given by:

$$\eta = J\frac{K_T}{K_P} \tag{2.1}$$

where J is a nondimensionalisation of the velocity called the advance ratio and given by:

$$J = \frac{V}{nD} \tag{2.2}$$

where V, n, and D are, respectively, the forward speed, rotation, and diameter of the propeller.

The coefficients of thrust (K_T) and power (K_P), present in Equation 2.1, are defined as:

$$K_T = \frac{T}{\rho n^2 D^4} \tag{2.3}$$

$$K_P = \frac{Power}{\rho n^3 D^5} \tag{2.4}$$

Where ρ is the air density, T is the thrust generated and $Power$ is the power absorbed by the propeller.

Usually, the efficiency of a propeller is plotted against the advance ratio, as shown in Figure 8.

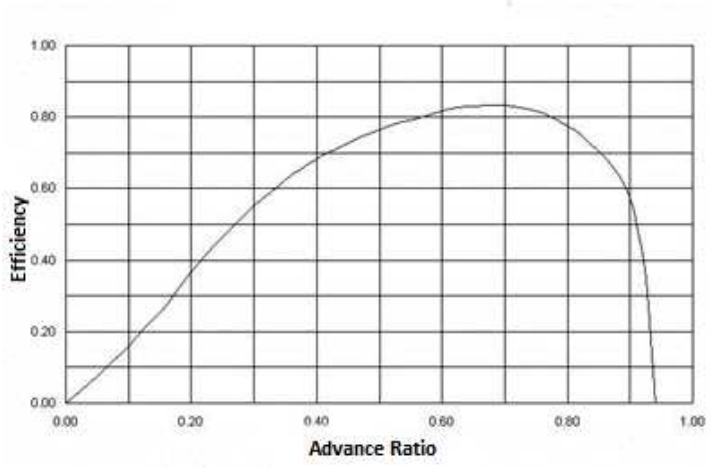

Figure 8 – Propeller efficiency by the rate of advance - Adapted from `http://www.blackholes.org.uk/PP/e1low.gif` (available on 06/28/2023)

This information is relevant to find the ratio of progress with the highest efficiency value. In order for the propeller to be considered suitable for an aircraft, it is important that its maximum efficiency occurs at an advance ratio that corresponds to an important speed of the aircraft, such as, for example, the cruising speed.

The increase in the pitch of a propeller causes the efficiency curve to shift to the right, increasing the advance ratio at maximum efficiency, as shown in Figure 9.

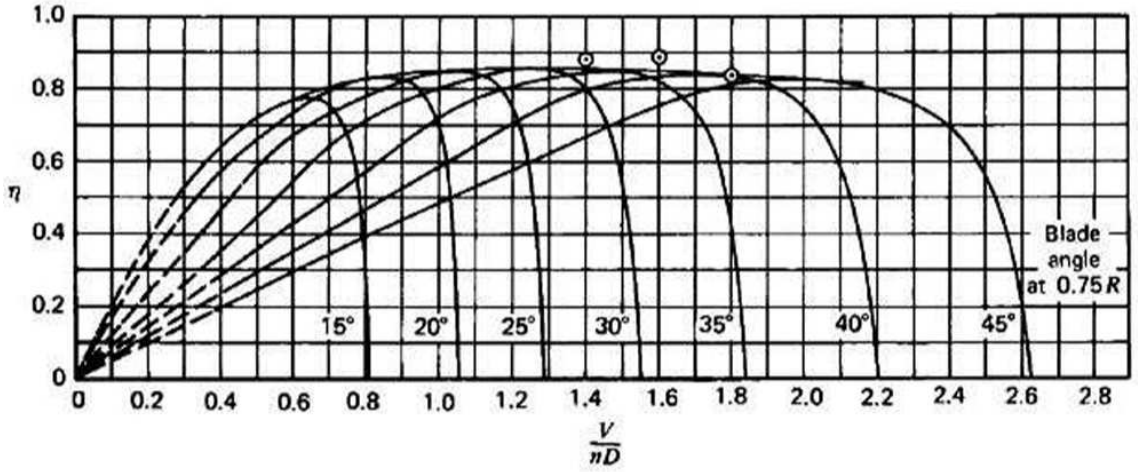

Figure 9 – Propeller efficiency due to the advance rate for different steps - Adapted from [1]

The values of the efficiency (2.1), thrust coefficient (2.3), and power coefficient (2.4) as a function of the advance ratio are obtained through information on the thrust and torque resulting from the propeller operation. These values are obtained experimentally or through one of the tools presented in Subsection 1.3, which are the Blade Element Theory and its variations, and the computational fluid dynamics.

2.2 Propeller Analysis Models

2.2.1 BET and BEMT Methods

The BEMT method was developed from two other methods: the Actuator Disk Theory and the Blade Element Theory.

In the Actuator Disk Theory, the propeller is considered to have infinite blades and can be seen as a circular disk. The fluid is also considered to be inviscid, incompressible, and uniform throughout the disc. However, any rotational movement in the slipstream and frictional drag of the blades is neglected. The layout of the model is represented in Figure 10

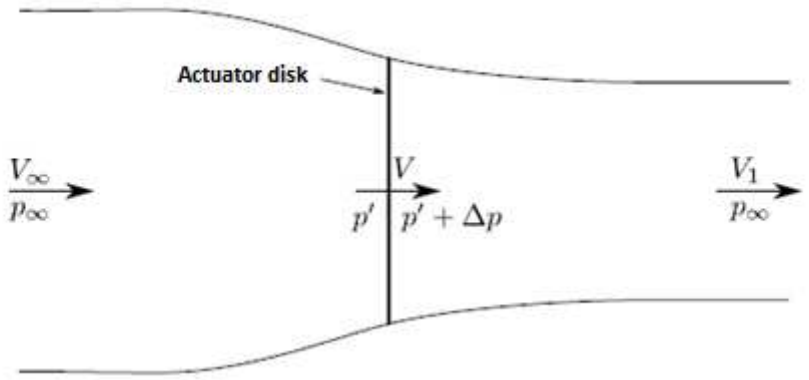

Figure 10 – Blade Element Theory model, adapted from [2]

According to Bernoulli's equation:

$$p_\infty + \frac{1}{2}\rho V_\infty^2 = p^{'} + \frac{1}{2}\rho V^2 \tag{2.5}$$

For the front of the disc:

$$p^{'} + \Delta p + \frac{1}{2}\rho V^2 = p_\infty + \frac{1}{2}\rho V_1^2 \tag{2.6}$$

And to the rear part of the disc:

$$\Delta p = \frac{1}{2}\rho(V_1^2 - V_\infty^2) \tag{2.7}$$

The incompressibility hypothesis simplifies the analysis. Developing, it is obtained that the thrust is given by:

$$T = A\Delta p = \frac{A}{2}\rho(V_1^2 - V_\infty^2) \tag{2.8}$$

Where A is the disk area.

Thrust can also be written as:

$$T = A\rho V(V_1 - V_\infty) \tag{2.9}$$

Equating the two formulations for thrust, we obtain:

$$V = \frac{V_1 - V_\infty}{2} \tag{2.10}$$

Defining the speed increase on the disk as an induced speed V_a:

$$V = V_\infty - V_a \tag{2.11}$$

$$V_1 = V_\infty + 2V_a \tag{2.12}$$

Therefore:

$$T = 2A\rho V_a(V_\infty + V_a) \tag{2.13}$$

Then, the disk is divided into annular elements, and for each annular element, there is an elemental torque and an elemental thrust. To find the total thrust and torque, elemental fractions must be integrated throughout the disk (Figure 11.

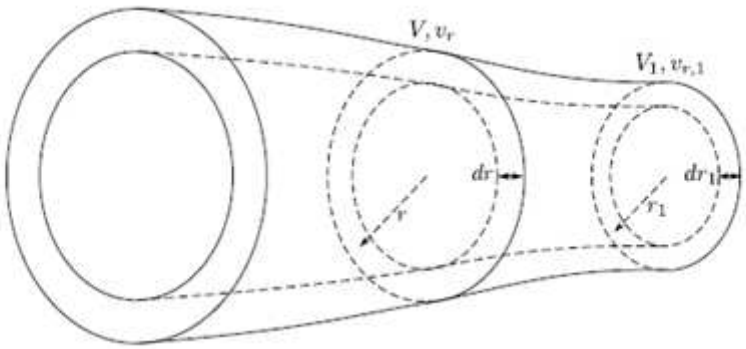

Figure 11 – Division of the actuating disc into annular elements

As limitations and inaccuracies of the Actuator Disc Theory:

- Does not consider the energy of rotation of the air currents originated due to the thrust;
- Does not consider the drag or friction of the propeller blades moving through the air;

- Does not consider the non-uniformity of the thrust, with tip and hub losses;
- There is a loss of energy due to the finite number of blades, since there is variation in thrust at a given point over time;
- Does not provide information on how to size propeller blades to produce the desired thrust.

The Blade Element Theory (BET) is a simplified model for studying the performance of a given propeller. At BET, the propeller is subdivided into small elements, and the two-dimensional flow of each element is analyzed individually. The theory is based on the assumption that there is no interference between adjacent elements.

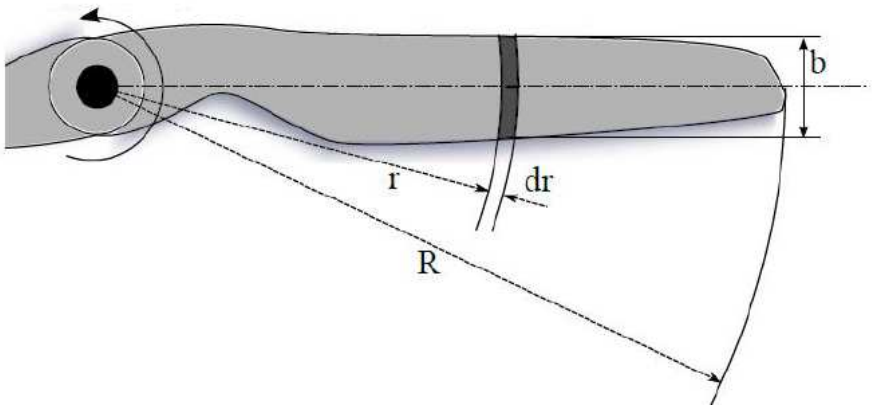

Figure 12 – Scheming of the Blade Element Theory Model

As seen in Figure 12, the distance between the propeller axis and the centerline of each element is given by r and the width of each subdivision is dr. R is the distance between the axis and the tip of the propeller. c is the chord and ϕ is the torsion angle for the section of each element.

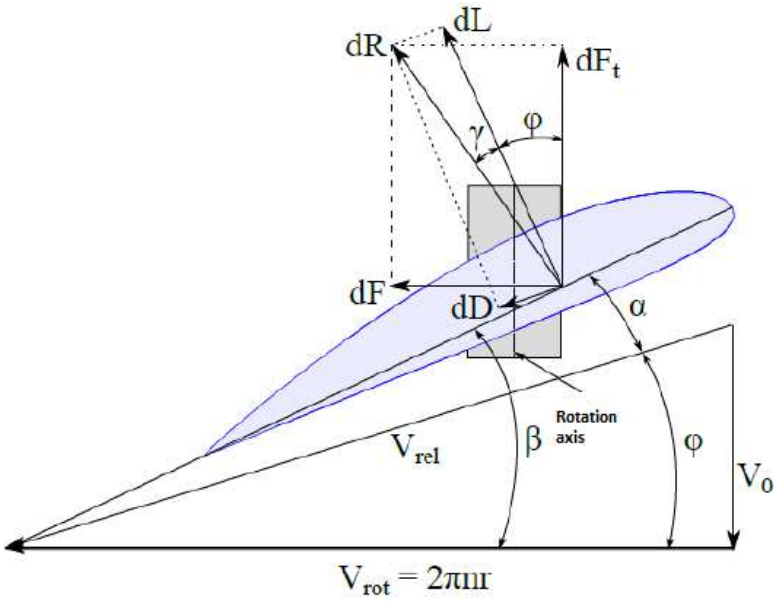

Figure 13 – Forces and speeds acting on the Blade Element Theory

The forces and speeds acting on each element can be seen in Figure 13. The radial elements have their forces integrated throughout the radius of all the blades. The sum of forces on all elements represents the total thrust and torque.

As limitations of the model:

- There is no interference between the blade elements;
- There is no flow in the radial direction;
- The tip effects are not taken into account.

The union of these two basic models, after some corrections, results in the BEMT method.

2.3 Physical Modeling of Viscous and Incompressible Flows

When computer simulations are to be performed, some relevant issues must be observed for the physical and mathematical modeling of the problems.

In this Section, a description of the approaches that allow the creation of a computational model are discussed. To meet the demand for this research, the equations for the continuous medium of fluid dynamics are presented below. The characteristics of turbulent flows and some models that may represent this behavior are also presented. The Section ends with a discussion on the continuum kinematics, where one must observe changes in the referential caused by moving domains.

2.3.1 Modeling Levels

When it is desired to formulate problems in fluid mechanics, as in any other science, some approximations must be made. Such approximations qualify the different flow models that exist and are carried out at different hierarchical levels. Hirsch [90] proposes the following hierarchical classification.

- Reality Level: this corresponds to the descriptions used to portray the physical world, comprising several scales from subatomic to astronomical. Fluids are linked to the idea of the continuum, without reference to subatomic scale. Macroscopic quantities can be treated as results of averages over many interactions between molecules using empirical considerations, called constitutive equations. Based on this hypothesis and the principles of conservation of mass, amount of movement, and energy, it is possible to describe the behavior of fluids by Navier-Stokes equations.

- Time Level: corresponds to the required temporal resolution of the model. The conservation equations can be obtained by integrating the conservation laws on all time scales smaller than those necessary for analyzing the problem.

- Spacial Level: relates to the number of spatial variables used to describe the flow. All flow is three-dimensional and, however, there are simplified models that use the averages of fundamental conservation laws along one or two spatial dimensions, thereby reducing the complexity of the problem. An example of using two-dimensional models comes from the shallow water equations [91]. These equations are applied to flows in bays and ports.

- Dynamic Level: concerns the relative importance of the forces that govern the flow. Depending on the importance of a given force, it can be disregarded, resulting in a simpler mathematical description. In lubrication problems, where viscous effects are dominant, the forces of inertia are usually neglected. In other cases, simplified models are applied in different flow regions.

- Level of Homogeneity: applicable to multiphase flows and flow in porous media. The model equations are obtained by averaging the conservation equations in volumes containing mixtures of different materials External data containing information about the changes in mass, amount of movement, and energy at the material interfaces are required.

Flow compressibility is an important consideration in fluid mechanics. Liquids are typically treated as incompressible, while gases are considered compressible. However, this classification is not definitive as liquids still have some compressibility, and low-speed gas flow can be approximated as incompressible.

It is important to note that the question of compressibility is not limited to the physical aspect alone, but directly affects the mathematical characteristics of the equations that represent the model [92] and [93]. Flow compressibility can be inferred from the Mach number, defined as:

$$Ma = \frac{v}{c} = \frac{\text{fluid speed}}{\text{sound speed}} \tag{2.14}$$

It should be noted that for values of Mach number less than 0.3, the flow can, in general, be considered incompressible [94].

2.4 Multi-Objective Optimization

In most real engineering problems, in addition to several design variables, there is also more than one objective that must be prioritized when carrying out a project. Due to this aspect, there is a need to perform optimizations observing more than one parameter of interest, called multi-objective optimization. Single-objective optimization aims to seek only an optimal solution for only one objective function. In multi-objective optimization, on the contrary, the objective is not to find a single optimal solution, but rather a set of solutions that represent a dominant solution region of the problem. [95]

2.4.1 Multi-Objective Optimization Problem

The multi-objective optimization problem (MOOP) is defined through some common concepts:

- Design variables: these are the variables that the optimizer algorithm has the capacity to work with in order to carry out the optimization;
- Objective functions: functions capable of evaluating the quality of a solution through the design variables;
- Constraints: These are magnitude constraints imposed on the design variables. They are usually related to physical, engineering, or economic limitations.

A Constrained Multi-objective Optimization Problem (CMOP) is formed by a set of variables that will be varied throughout the optimization process, a set of objective functions to be optimized, and a set of constraints that must be satisfied for the solution to be feasible. The problem can be written as follows [96]:

min

$$Z(x) = (z_1(x), z_2(x), ..., z_n(x)), \tag{2.15}$$

subject to

$$g_j(x) \leq 0, \quad j = 1, ..., n_g, \tag{2.16}$$

$$h_l(x) = 0, \quad l = n_g + 1, ..., n_h \tag{2.17}$$

$$a_i \leq x_i \leq b_i, \quad i = 1, ..., n_a \tag{2.18}$$

where $x = x_1, ..., x_{n_a}$ is a n_a - dimensional variable project vector, $Z(x)$ is a function that returns a vector of values, $g(x)$ and $h(x)$ are constraints of inequality and equality.

The variables a and b are the upper and lower limits of x; n_{obj}, n_g, and n_h represent the number of objective functions, inequality constraints, and equality constraints, respectively.

2.4.2 Dominance and Pareto-Optimality

The concept of optimality in multi-objective optimization is based on the notion introduced by Francis Ysidro Edgeworth in 1881 and later generalized by Vilfredo Pareto in 1896. In multi-objective optimization, Pareto's concept of dominance is used to compare two feasible solutions to the problem [13]. The term Pareto front was coined to determine a region with dominant solutions. A multi-objective optimization problem seeks to find a particular Pareto front so that, allied to its experience, the designer or project responsible is able to determine one or more solutions that best meet the problem resolution.

Figure 14 presents a schematic mapping of a general problem where a three-dimensional variable space, that is, a problem with three variables, is injected into a two-dimensional solution space, therefore, a problem with two objective functions:

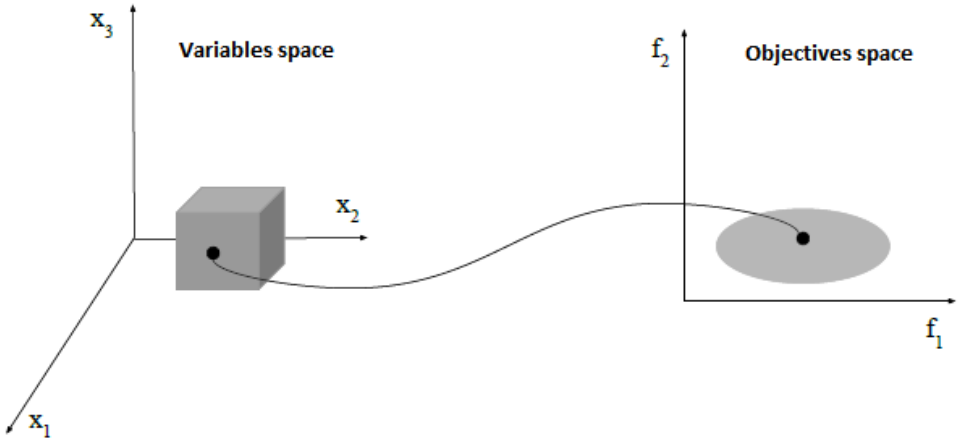

Figure 14 – Schematic mapping of solutions in three-dimensional space to objectives in a two-dimensional space - Adapted from [3]

Considering two different solutions, s_1 and s_2, s_1 is said to dominate s_2 ($s_1 \preceq s_2$), for minimization cases, if the following conditions are met:

- The solution s_1 is better than or equal to s_2 in all objective functions.
- The solution s_1 is strictly better than s_2 in at least one objective function.

Figure 15 illustrates the concept of dominance between two points. Points A and B have different values of f_1 and f_2 and point B has both values less than A, so $B \preceq A$. A region of non-dominated solutions is called of Pareto-optimal set and represents the solution to a multi-objective optimization problem [13].

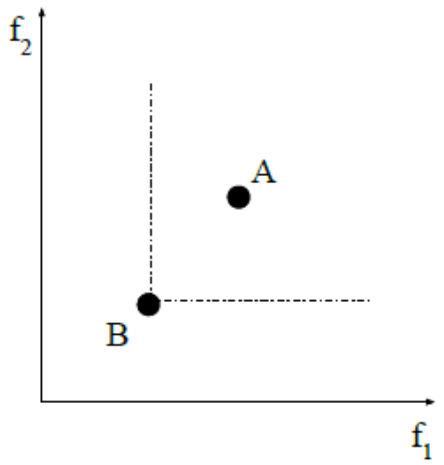

Figure 15 – Scheme of dominance between two solutions - Adapted from [3]

As multi-objective optimization works with two or more search spaces, it is important that the solutions are distributed satisfactorily in all of these. For this condition to be achieved, therefore, it is necessary to obtain solutions in efficient ways, which can be a task of considerable computational costs.

According to Azuma [3], there are three important goals in multi-objective optimization:

- Obtain a set of solutions that is as close as possible to the Pareto front;
- Obtain a set of solutions with the greatest possible diversity, including criteria such as uniformity in spreading along the Pareto front;
- Achieve the two previous goals with the greatest computational efficiency possible.

Figure 16 graphically represents the first two goals. As can be seen from the representation, convergence, and diversity can be conflicting and, for this reason, it is necessary, when evaluating the performance of an algorithm, to use metrics that consider both goals.

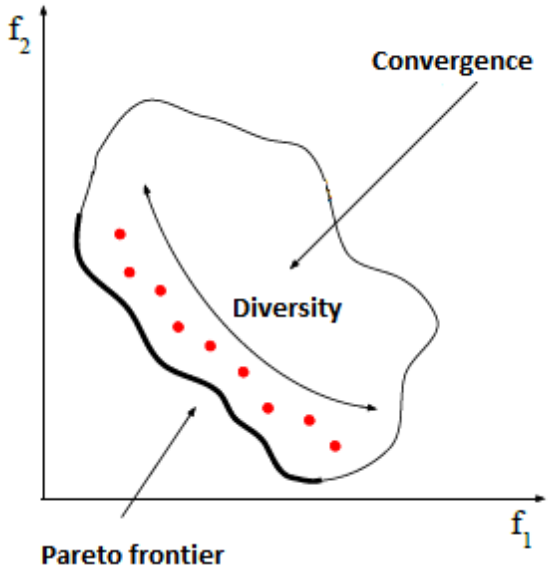

Figure 16 – Diversity, convergence, and Pareto front concepts - Adapted from [3]

2.4.3 Evolutionary and Genetic Algorithms

Multi-objective Evolutionary Algorithms (MOEAs) have been the subject of studies during the last decades and can be considered one of the most promising areas in the field of evolutionary computing [97]. In the field of engineering, many researchers have devoted themselves to the design and creation of evolutionary algorithms for solving multi-objective optimization problems.

Genetic algorithms (GA), a class of evolutionary algorithms, are a set of stochastic algorithms for efficient and robust search. GA simulates the biological evolutionary process by applying genetic operations on chromosomes. From an initial population, evaluations are carried out through objective functions and an appropriate application of genetic operators such as selection, mutation, and cross-over. The flow of a GA is shown in Figure 17.

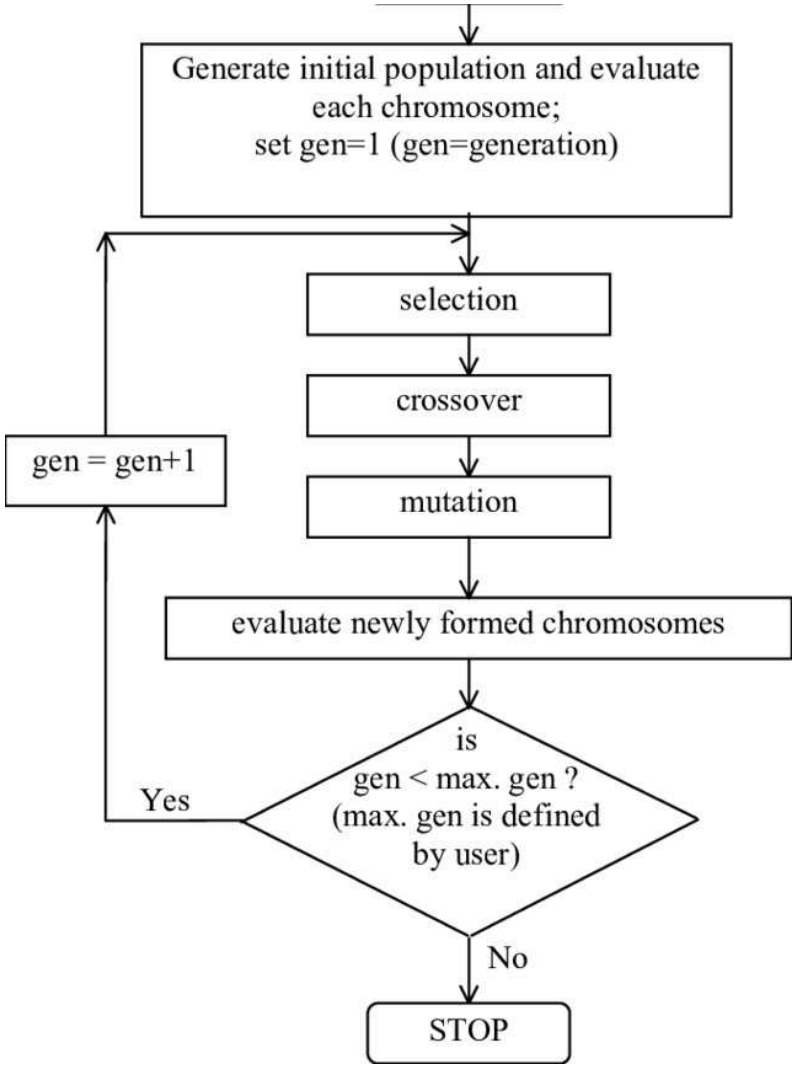

Figure 17 – Flow chart of a binary genetic algorithm - Withdrawn from [4]

For the optimizations carried out in the present work, were adopted evolutionary algorithms codes and later adapted to the MATLAB programming environment through the PlatEMO Software [30]. These codes and tools will be addressed conveniently in Chapter 4 and Chapter 5, respectively.

2.5 Campbell Diagram

In this Section, solutions to consider the effects of propeller rotation and aerodynamic effects in the Campbell Diagram will be discussed.

2.5.1 Rotation Influence

This Subsection aims to investigate how rotation affects the natural frequencies of vibration in propeller blades. Ramberg [5] used the Rayleigh energy method to calculate the influence of rotation on natural frequencies, since for speeds of rotation of a practical order, the shape of the deflection curve is not appreciably changed by the centrifugal force, and an accurate value may be obtained. Figure 18 shows how rotation influences the first two vibration frequencies for the type 32 propeller blade. The affine blade model, developed by Theodorsen [98], is also presented in this work. This method proposes that the frequency values for a blade can be found using a base model.

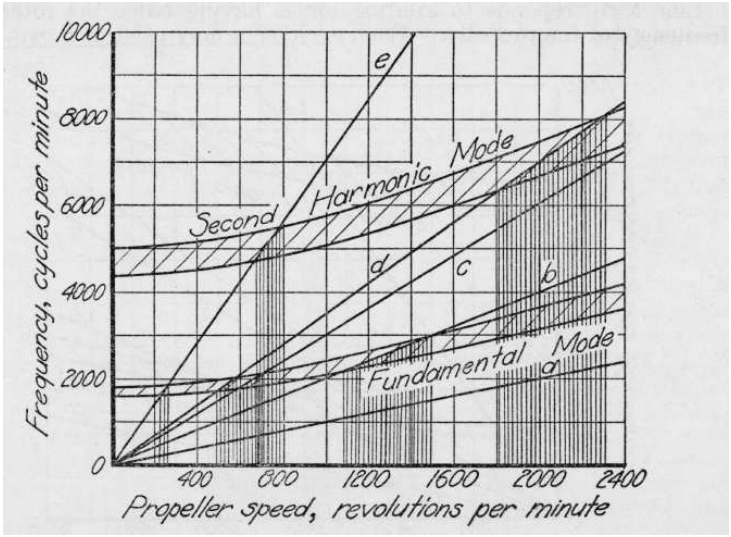

Figure 18 – Campbell Diagram for blade type 32 - Withdrawal from [5]

Lu *et al.* [6] presents a method for determining the natural frequencies from an unmanned micro helicopter blade subject to rotation. The natural frequencies and mode shapes of the blade for the helicopter are studied by using beam characteristic orthogonal polynomials by the Rayleigh-Ritz method. The variation of natural frequencies with the rotational speed and the mode shapes at different rotational speeds are plotted in Figure 19.

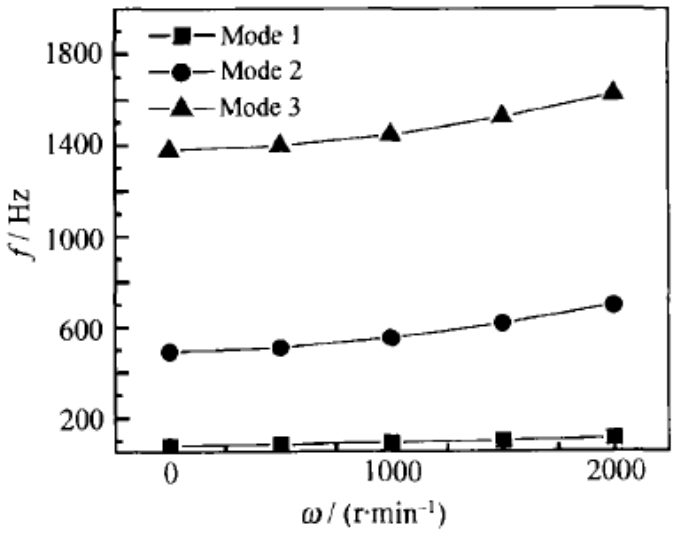

Figure 19 – Campbell Diagram for micro helicopter blade - Withdrawal from [6]

A similar study is conducted by Bicak [99]. Through the dynamic stiffness matrix method, natural frequencies of a coupled bending-bending-torsional are calculated. It is assumed that the blade has a symmetric airfoil cross-section, the distance at the root between the elastic axis and the axis of rotation is zero, and the area centroid of the cross-section coincides with the elastic axis.

Finally, Baxy [7] proposes a method where the blades of a rotating device can be approximated as a cantilever beam. According to the method, the blade natural frequencies influenced by rotation are given by:

$$\hat{\beta}_j^4 = \beta_j^4 + \epsilon_c \tilde{\lambda}_j^4 + \epsilon_r \hat{\lambda}_j^4 + \epsilon_r \epsilon_c \hat{\tilde{\lambda}}_j^4 \tag{2.19}$$

where under-script j is related to frequency mode, β and $\hat{\beta}$ are uncorrected and corrected non-dimensional frequencies, λ are correction factors, ϵ_c and ϵ_r are non-dimensional rotation and curvature parameters. The author provides tabulated data for all coefficients used in the method through non-dimensional tables. Figure 20 shows the results obtained with the method compared with Finite Element Method results.

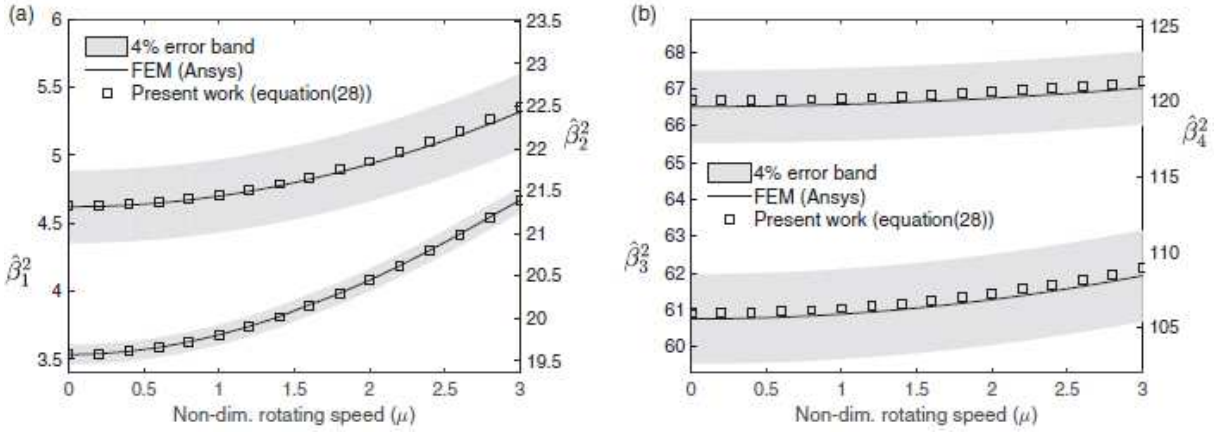

Figure 20 – Non-dimensional Campbell diagram comparing FEM and Baxy method - Withdrawal from [7]

Rao [8] proposes a method to find the modal frequencies of a cantilever beam. For this, mass and stiffness matrices are derived. Breadth and depth are considered for each section of the beam, as well as the twist angle. Shear and rotation effects are also considered.

Figures 21 and 23 show the influence of rotation and twist angle effects on the first four natural frequencies.

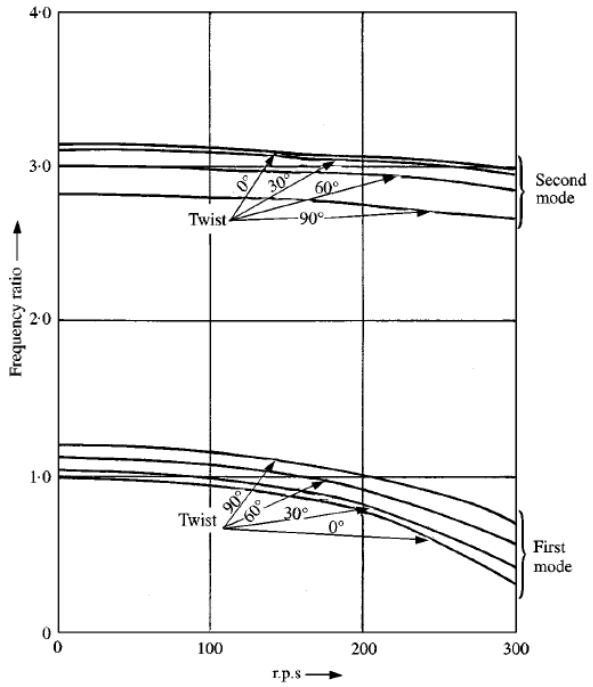

Figure 21 – Effect of rotation and twist on first and second natural frequencies - Withdrawal from [8]

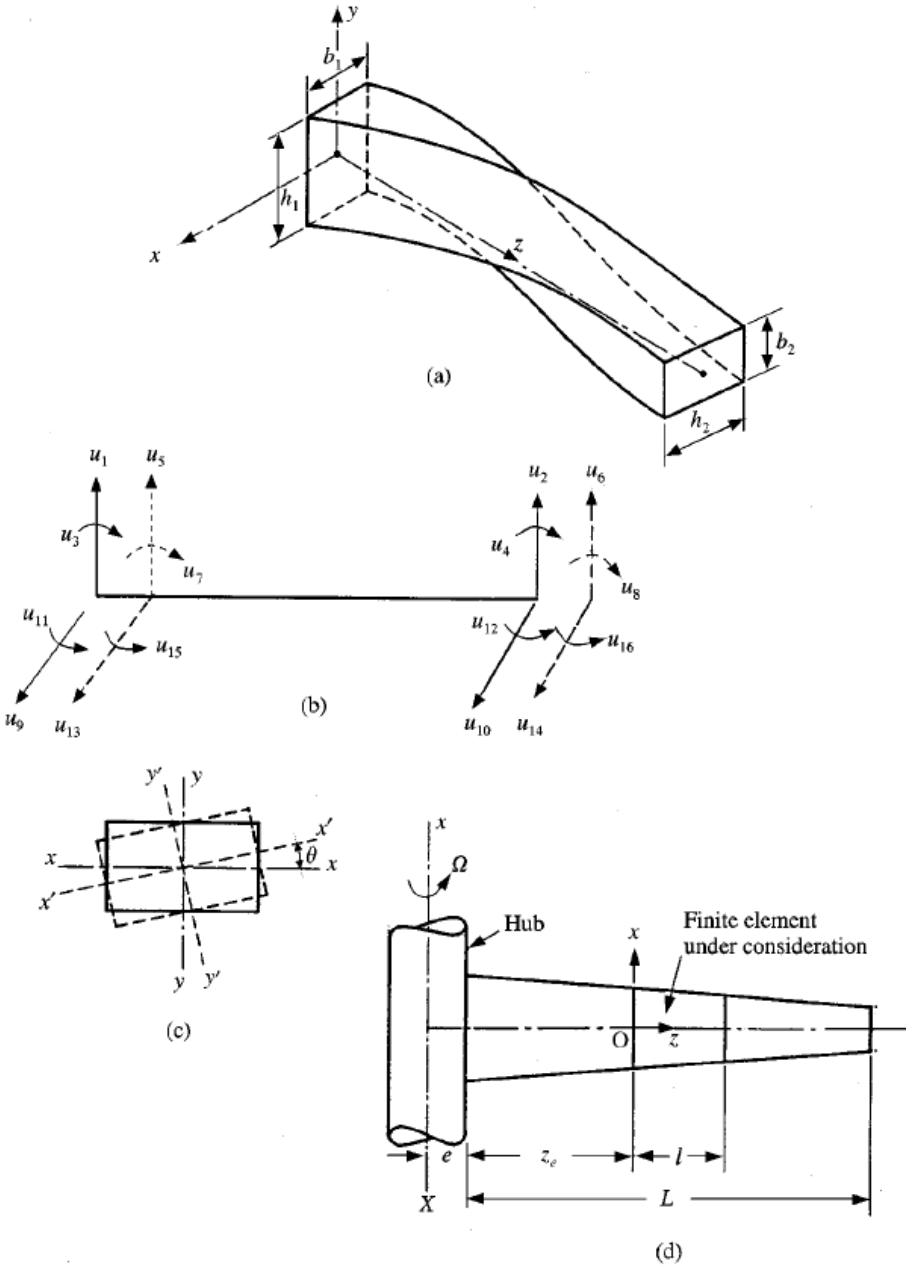

Figure 22 – (a) An element of a tapered and twisted beam, (b) degrees of freedom of an element, (c) angle of twist, (d) rotation of a tapered beam - Withdrawal from [8]

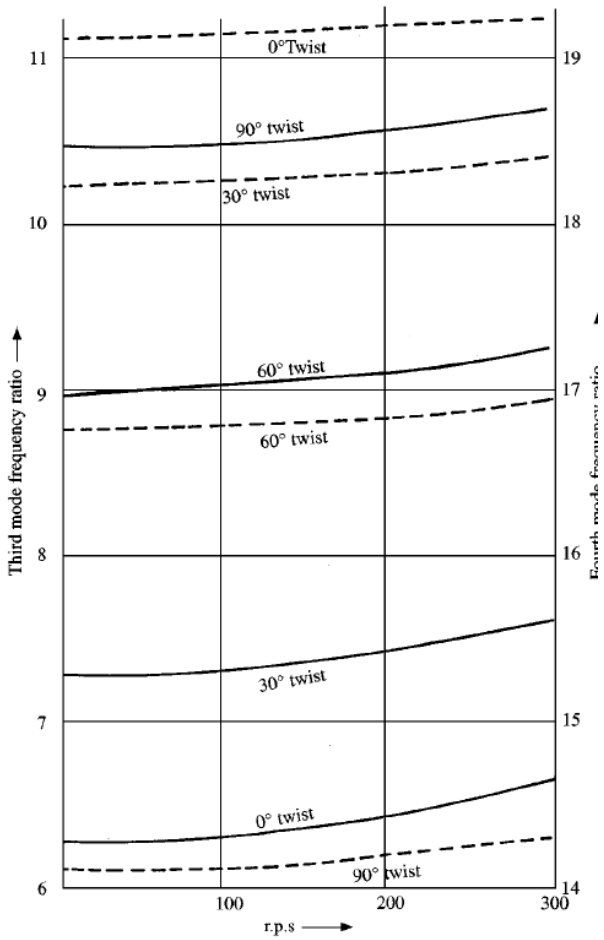

Figure 23 – Effect of rotation and twist on third and fourth natural frequencies - Solid line represents the third mode and the fourth is represented by the dashed line - Withdrawal from [8]

2.5.2 Aerodynamic Excitation

This Subsection presents how aerodynamic influences can be accounted in the Campbell Diagram. Boyce [9] presents the following case:

"For example, take the second-stage blade of a hypothetical compressor. Its first flexural natural frequency is calculated and found to be 200 Hz. From the Campbell diagram figure, it is apparent that a forcing frequency of 12,000 rpm produced by operating the compressor at 12,000 rpm will excite the 200-Hz first flexural frequency of the blade (200 Hz $\times$ 60 = 12,000 rpm). Also, there are five inlet guide vanes ahead of the second-stage blade row. Operating the compressor at 2,400 rpm will excite the 200-Hz natural frequency of the blade (200 Hz $\times$ 60 = 5 $\times$ 2,400 rpm)."

The text also introduces the concept of band spread around a natural frequency, as shown in Figure 24.

Antony [100] focuses his work on the study of structural analysis of turbine

blades. For that, he performs an extensive dynamics structural analysis to predict natural frequencies and modal forms using Finite Element Method. Through such analyses, it is possible to draw the Campbell diagram and, therefore, study the possibility of resonance in operating speeds. To carry out the work, the frequency of the aerodynamic excitation was considered as N × RPM/60, where N is the number of turbine blades. In other words, the engine order N must be considered in the diagram.

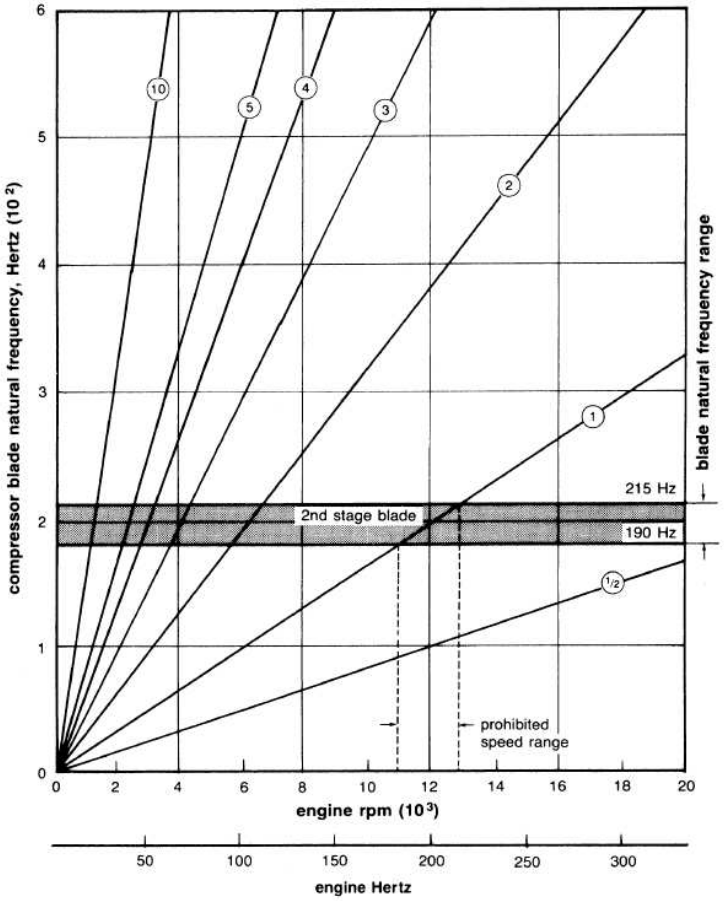

Figure 24 – Campbell diagram with band spread on natural frequency - Withdrawal from [9]

Piccirillo [101] cites as a general formulation for engine orders:

$$EO = mN \pm n_i \qquad \forall\, m \in \mathbb{N} \tag{2.20}$$

Where EO is engine orders, N is the number of blades and n_i are the nodal diameters that can assume the values:

$$n = \frac{N}{2}, \qquad if\ N\ is\ even \tag{2.21}$$

$$n = \frac{N-1}{2}, \qquad if\ N\ is\ odd \tag{2.22}$$

n_i can have values between 0 and n. An EO can be negative, which is equivalent to rotation in the opposite direction.

3 Methodology

This Chapter presents the reader with the methodology proposed by the present work to achieve the objectives set out in Section 1.2.

The methodology developed can be divided, for better understanding, into three major parts:

- Creation of an extensive database of aerodynamic profiles;
- Development of a unifying algorithm for several codes and tools capable of optimizing propellers aerodynamically, while its structural validity is checked;
- Execution of code developed through a typical mission, obtaining a propeller and then applying it in operational optimization.

Figure 25 is a flowchart that represents the first two steps, as well as important individual processes in each one.

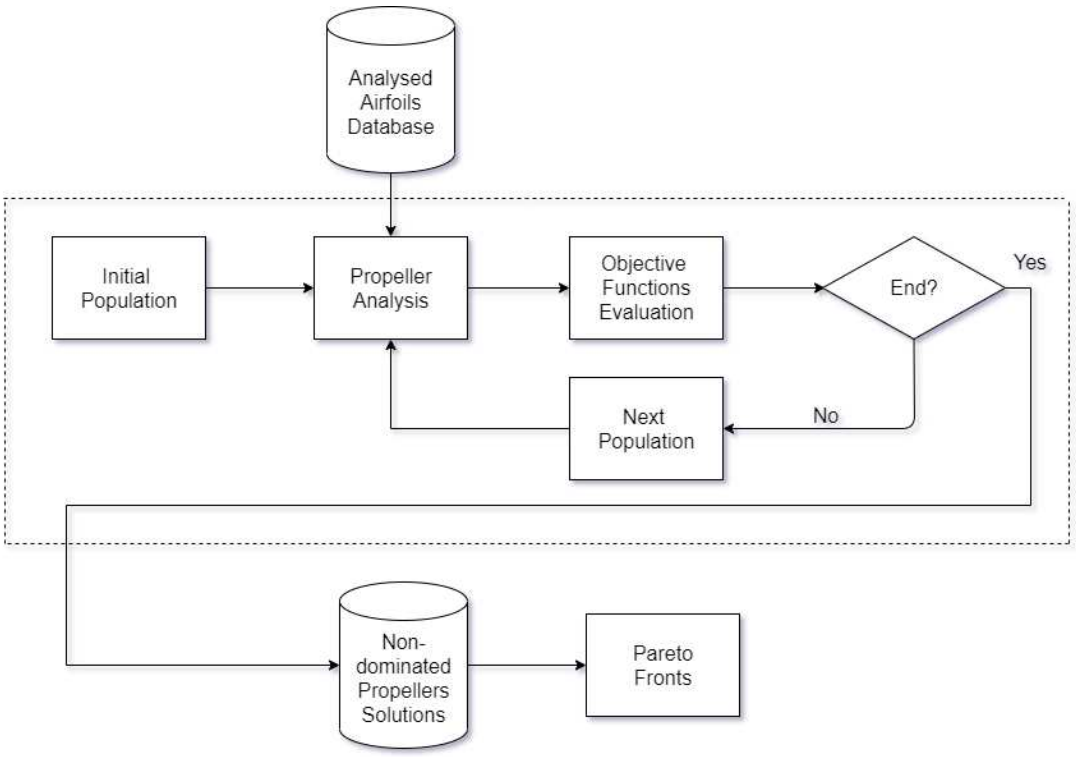

Figure 25 – Methodology Flowchart

The first stage of the work covers the creation of a profile database, as well as the refinement and subsequent aerodynamic analysis of these. There is a wide range of different aerodynamic profiles in the literature, however, there is no strict standardization of how your data is offered. Therefore, it is necessary to carry out data standardization processes,

as well as the refinement of these profiles concerning the number of points in Cartesian coordinates. After the process of improving this data set, it is possible to perform the aerodynamic analysis of these aerodynamic profiles. For this, the panel method was chosen, using the XFOIL code and the XFLR5 software, which will be covered in due course throughout the work.

The second part of the present work proposes to create a general algorithm that, using a multi-objective function, is able to select, through evolutionary processes, viable propellers on the Pareto front. At this stage, it is important for the reader to understand that from a group of chosen variables, several generated propellers need to be correctly analyzed from an aerodynamic performance point of view. This analysis will be performed through codes that use the BEMT due to its high efficiency when analyzed, its low computational cost, and moderate precision. When the aerodynamic performance characteristics of a group of propellers is obtained, it is possible to evaluate them according to the proposed objectives. After the evaluation, it is possible to apply the genetic operators: selection, cross-over, and mutation. This process is repeated until the convergence criteria are reached. The codes used will be explained in Chapter 4 and development will be covered in Chapter 5. This process will be carried out using different paradigms. In the first group of optimizations, two different engines are proposed as inputs and different dimensionless coefficients as objective functions. In this group, the engine power values are used as input. In the second optimization group, a typical mission of a Turboprop aircraft is proposed, where the required powers and flight speeds are inputs at specific points, and the objective function is power minimization.

The third and last part of the work consists of using the propeller created in the previous step to carry out an operational optimization of a proposed mission. The characteristic mission is first calculated using fixed propeller rotational speeds, and then the same mission is calculated using multiple propeller rotational speeds. After comparing the two missions, a third case in which there is a structural vibration constraint is also proposed.

The set of elements used, including the airfoil database and its aerodynamic data, the JAVAPROP, and the developed structural code were defined in PlatEMO as a problem called OptProp.

4 Codes and Software Overview

In this Chapter, the codes and programs that were used, either in full or after certain modifications, to perform the optimizations proposed in this work are presented.

4.1 XFOIL

The XFOIL code was created by Mark Drela in 1986. The main objective was to combine the speed and precision of high-order panel methods. Since version 1.0, XFOIL has undergone numerous revisions, updates, and improvements. These changes originated mainly from perceived deficiencies during the actual use of the project, so XFOIL is now strongly focused on the practical development of airfoils [102].

Once the geometry of an aerodynamic profile is provided through coordinates in a plane, XFOIL is able to calculate the pressure distribution in this airfoil at different angles of attack, in certain Reynolds numbers. This pressure distribution is provided through pressure coefficients on both the upper and lower surfaces of the airfoil. Through pressure coefficients, XFOIL also delivers important airfoil characteristics to users, such as lift, drag, and moment coefficients through a polar file. In Figure 26 a data flow is shown where it is possible to observe how XFOIL works. As explained in this paragraph, it can be seen in the figure that the initial program input is the airfoil coordinate file and the output is a polar file.

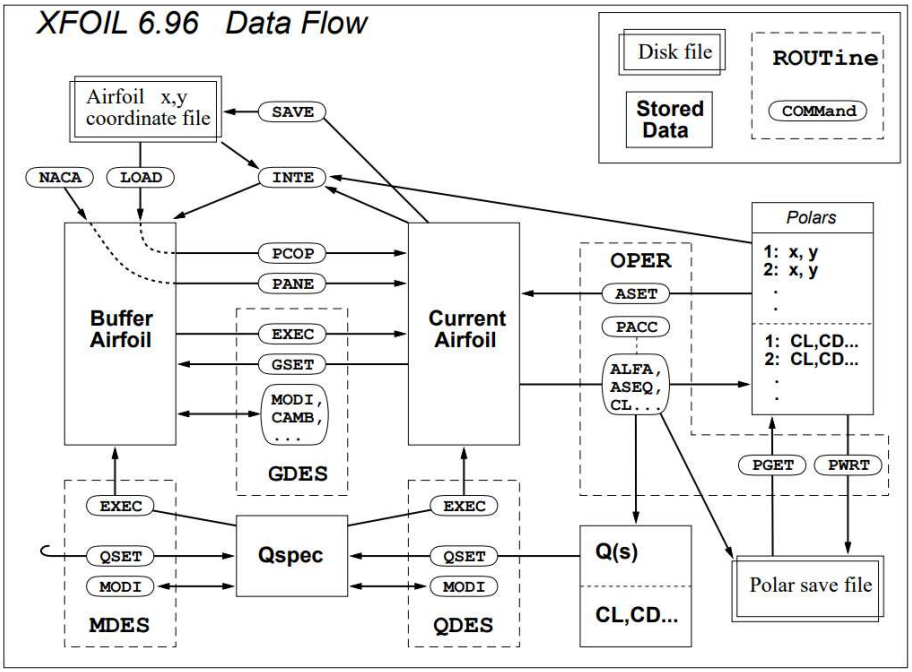

Figure 26 – XFOIL Dataflow - Withdrawn of `https://web.mit.edu/drela/Public/web/xfoil/dataflow.pdf` (available on 06/28/2023)

4.2 BET and BEMT Software

In the next Subsections, the BET (Blade Element Theory) and BEMT (Blade Element Momentum Theory) methods will be discussed, as well as some propeller analysis software that uses such methods in their implementation.

4.2.1 JAVAPROP

JAVAPROP is a tool developed in a JAVA environment that aims to carry out the analysis and design of propellers and wind turbines. The software uses the blade element theory method, implemented through a coupling of momentum considerations with the two-dimensional characteristics of the aerodynamic profiles used. As will be explored in the present work, JAVAPROP allows the use of different airfoils and how they impact the performance characteristics of the propeller. [103]

Figure 27 shows a schematic of some features available in JAVAPROP. Through a database with propeller geometric characteristics and engine characteristics, it is possible to analyze an arbitrary propeller, geometric modifications in that propeller as well as the optimum design of a propeller.

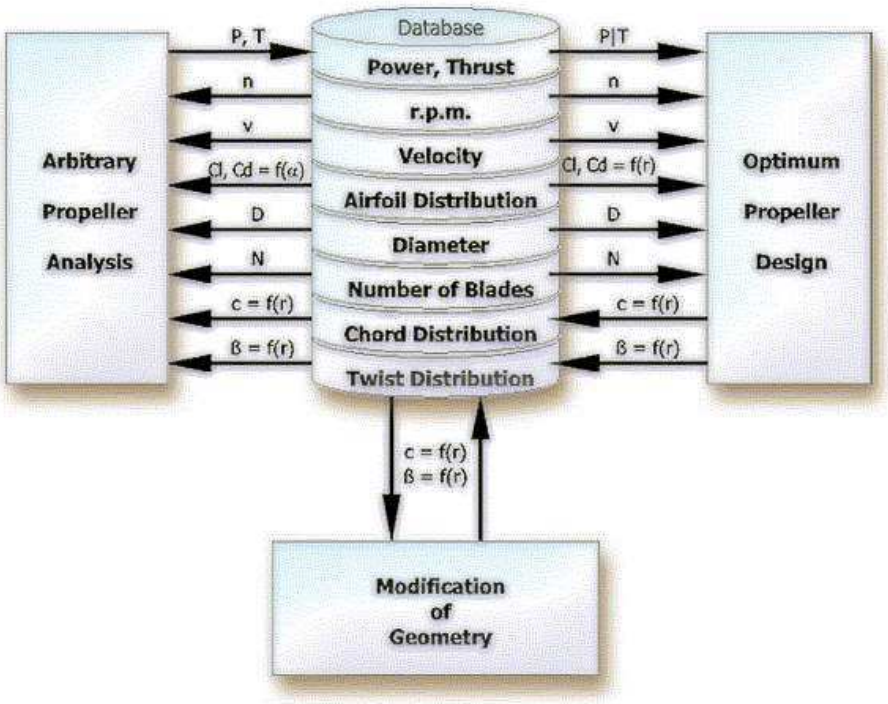

Figure 27 – JAVAPROP Schematization - Withdrawn of [10]

Since JAVAPROP is software developed from the blade element momentum theory, it is also expected that the theory's limitations will be extended to JAVAPROP. According to the JAVAPROP User's Guide [103], such limitations are:

- The disc loading of the propeller is not too high (thrust coefficient $K_t < 2$), which excludes static operation conditions;
- The number of blades is small ($n < 15$) so that no strong interaction due to overlap and thickness occurs;
- Three-dimensional effects are small (no winglets, no highly curved blades);
- Compressible flow effects are small and mostly two-dimensional ($M_{tip} < 1.0$).

JAVAPROP has a very restricted native database of aerodynamic profiles, but it is possible to import aerodynamic data files from external airfoils. It is also possible to use JAVAPROP automation processes using other software and programming languages such as MATLAB, Python, Octave, Maple, and Mathematica. Those processes will be explored in the future Subsection **5.2.1**.

4.2.2 JBLADE

The JBLADE software was developed as the object of study of a thesis prepared at the Department of Aerospace Sciences of the University of Beira Interior - Portugal, under the guidance of Miguel Silvestre [104]. The tool was developed in open source in the $C++$ programming language using the multiplatform framework Qt. The code is based on the QBLADE programs, developed in TU Berlin and XFLR5, developed by André Deperrois.

The performance coefficients of the aerodynamic profiles analyzed in JBLADE are the result of the coupling of QBLADE with XFOIL. JBLADE uses Blade Element Momentum (BEM) classic theory, with modifications made in order to improve the results by adding three-dimensional considerations of the flow ([105] & [106]). The software has a graphical interface that facilitates the construction and analysis of the propeller simulations. JBLADE's long-term goal is to provide a validated, accurate, and easy-to-use open source code that can be used to design and optimize a variety of propellers [11].

Figure 28 shows the two modules used to build JBLADE; XFOIL and BEM code. Among such data, there are polars, blades, and propellers as well as data obtained after simulations. Such a layout is based on QBLADE, since few changes have been made to the structure.

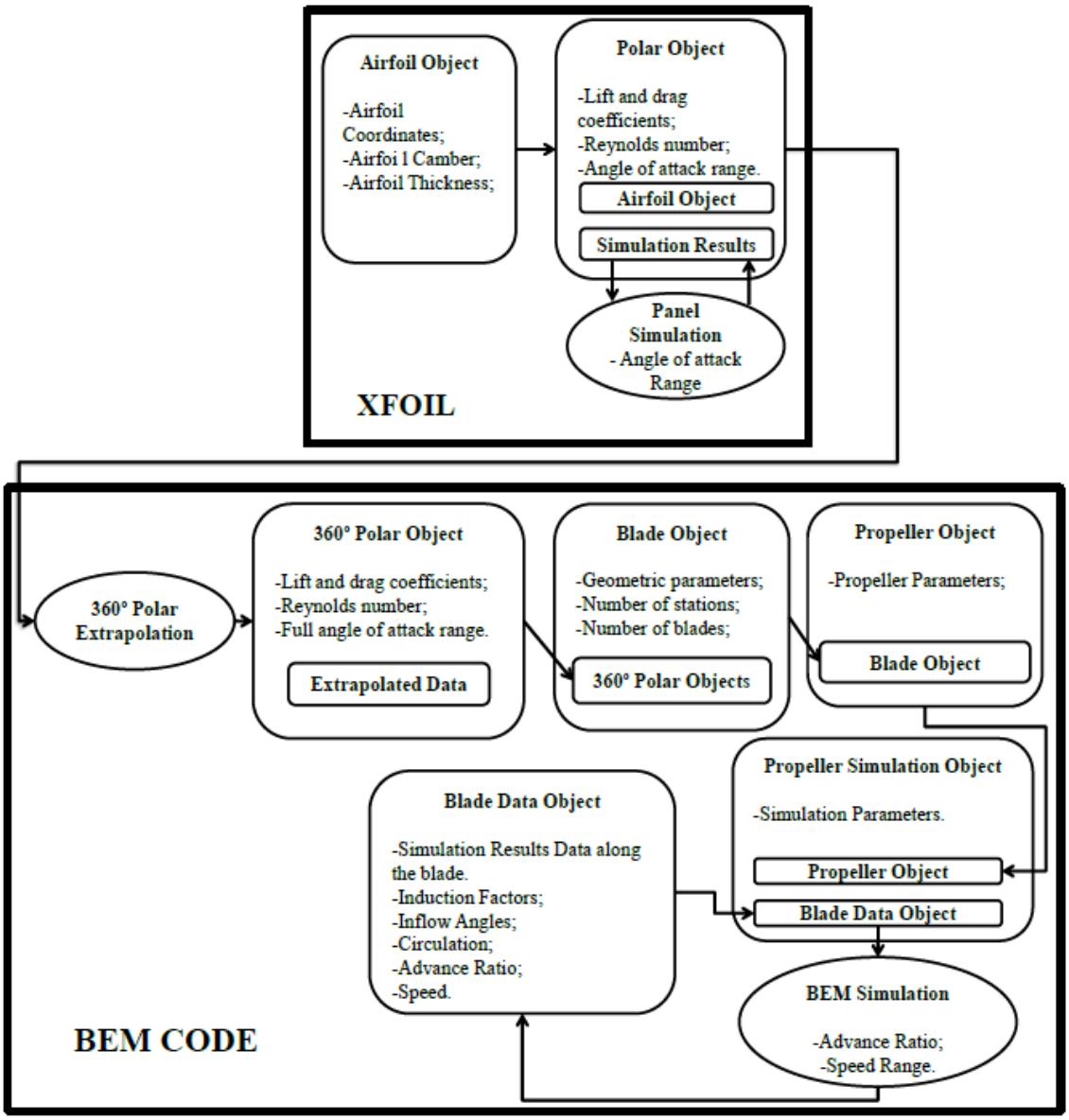

Figure 28 – JBLADE Schematization - Withdrawn of [11]

As explained in the previous Section regarding JAVAPROP, JBLADE is also a software developed from the blade element theory and therefore will also have its limitations as a counterpart. JBLADE is also based on XFOIL and will also share its limitations.

4.2.3 QPROP

QPROP is a software developed by Drela [12], through the programming language Fortran 77, which objective is to predict the performance of a propeller-engine group. QPROP uses an extension of the classical blade-element/vortex formulation, developed originally by Betz [107], Goldstein [47], and Theodorsen [108], and reformulated somewhat by Larrabee [109]. According to Drela, [12], those extensions include:

- Radially-varying self-induction velocity which gives consistency with the heavily-loaded actuator disk limit;
- Perfect consistency of the analysis and design formulations;
- Solution of the overall system by a global Newton method, which includes the self-induction effects and power plant model;
- Formulation and implementation of the Maximum Total Power (MTP) design condition for windmills.

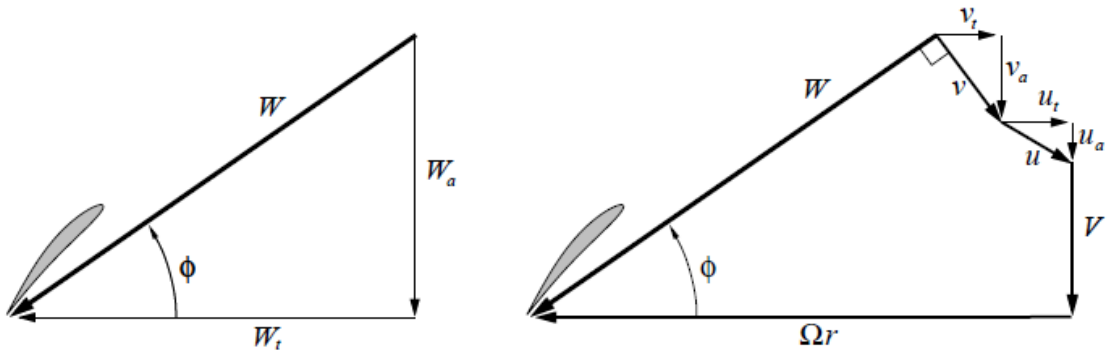

Figure 29 – Speed scheme for a QPROP airfoil section - Withdrawn of [12]

The development of the theory used by QPROP is presented in detail in Appendix A.

4.3 Evolutionary Algorithms

In this Section, the optimizer algorithms that were used to obtain the results will be presented.

4.3.1 NSGAII

Within the Multiobjective Evolutionary Algorithms (MOEAs), the NSGAII stands out for its effectiveness and is widely used in the literature. NSGAII was proposed by Deb [95] and its main feature is the order of non-dominance. All solutions evaluated by the algorithm are classified as dominated or non-dominated. The non-dominated, or dominant, are better classified in relation to the others. The iterations of the algorithm are repeated as long as all solutions are dominant.

Another feature of the NSGAII is the division of its solutions into different ranks. Each rank corresponds to the set of solutions that are not dominated by any other rank. In this way, rank 1 individuals dominate rank 2 individuals, who in turn dominate rank 3 individuals, and so on. Such a concept is exemplified through Figure 30.

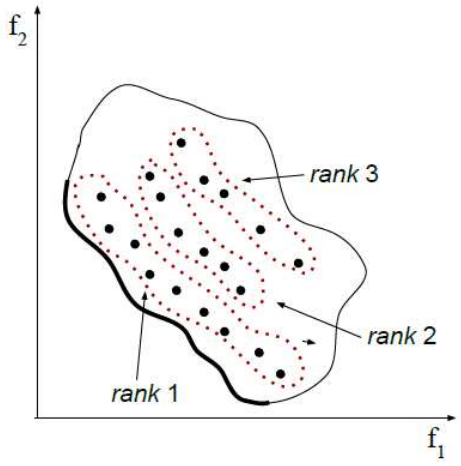

Figure 30 – Pareto ordering proposed by - Withdrawal of [13]

As soon as the subdivision into ranks is performed, the crowding distance is calculated. This parameter provides an estimate of the density of solutions in the region around a given point. Points that have values of the objective function at the ends receive infinite values for the crowding distance so that such solutions are always selected. Figure 31 exemplifies the crowding distance calculation process for an i point, which can be understood as the size of the largest cuboid that includes i without including any other points.

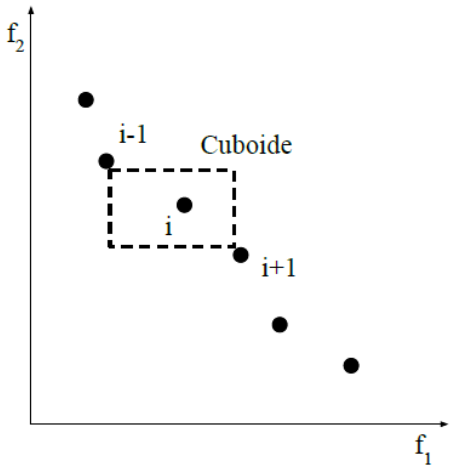

Figure 31 – Crowding Distance - Withdrawal of [13]

The crowding distance calculation process is performed for each objective function and is used to order individuals of the same rank. The use of this parameter generates a better spread of future solutions, avoiding agglomerations in regions and seeking new solutions in other viable regions. The solutions that will be chosen for the next iterations of the genetic algorithm will be the non-dominated solutions of the first rank, and the

solutions of the next ranks that can be chosen are those that have the most interesting crowding distance values.

4.3.2 MSOPS-II

Hughes [110] proposes the Multiple Single Objective Pareto Sampling (MSOPS) algorithm, which is a technique that allows multiple single-objective optimizations to occur in parallel and therefore explores a larger area of the potential population. The main advantage of this algorithm is that it does not rely on a Pareto front ranking to generate selective pressure. However, for the proper operation of MSOPS, it is necessary for the designer to generate a group of target vectors. Each individual in the population is evaluated, for each of the target vectors, based on a conventional aggregation method. In this format, each individual in the population will receive a score, for each element of each target vector, which indicates how well it performs in relation to the target conditions. Figure 32 demonstrates the process for a single population member:

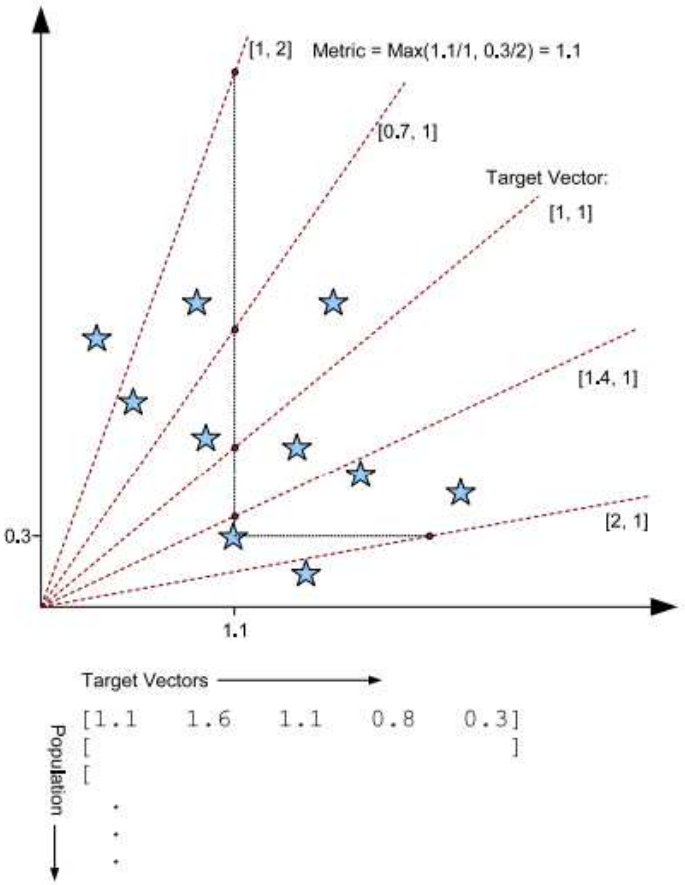

Figure 32 – Process of generating MSOPS ranking - Withdrawal of [14]

Subsequently, Hughes [14] proposes the second version of the algorithm, MSOPS-II, with the following improvements:

- redefinition of the fitness assignment method in order to simplify the analysis and allow better constraint handling. The original method had a computational cost of order $O(vp\log(p))$, while in MSOPS-II the cost is in the order of $O(p\log(p))$, where p is the number of elements in the population being sorted and v is the number of target vectors;
- automatic target vector generation, eliminating the need for the designer to make initial interventions. Figures 33 and 34 show, respectively, the target vector generation for MSOPS and MSOPS-II.

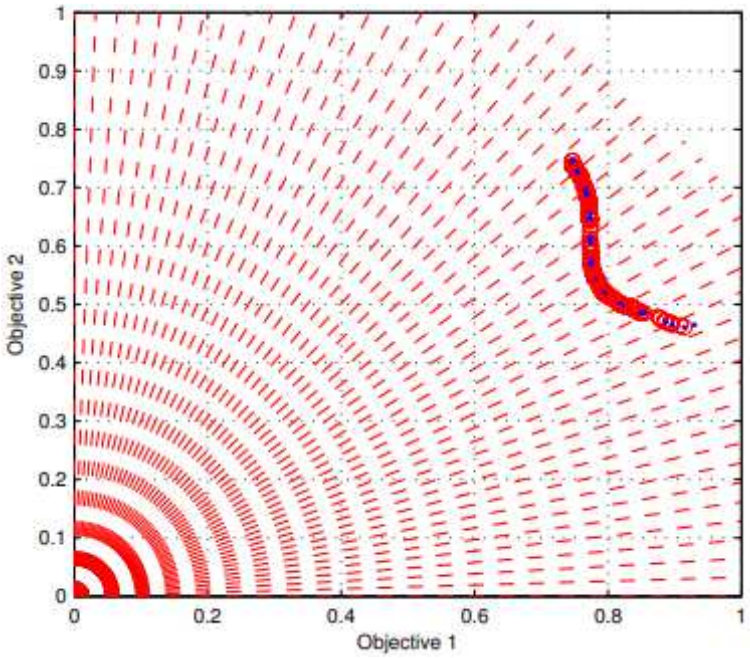

Figure 33 – Target vector generation method for MSOPS. In this scenario, many vectors do not intersect the feasible objective surface. The dashed lines show the direction of the target vectors, the circles represent the non-dominated points, and the dots the last generation population members - Withdrawal of [14]

4.3.3 ARMOEA

Seeking a new MOEA capable of addressing real-world problems and finding Pareto optimal fronts, Yi et al. [15] develop the ARMOEA algorithm. This algorithm introduces a new variant called preference angle and reference information-based dominance, aiming the creation of a stricter partial order among non-dominated solutions. In the proposed method, the Euclidean distance and angle information between candidate solutions and reference points are calculated to evaluate the degree of convergence and population diversity, respectively. In addition, an adaptive threshold is designed to adjust the judgment condition of ar-dominance using an iterative process in a pre-specified interval. The proposed algorithm increases the convergence speed of the population and reduces the number of solutions in the non-preferred region.

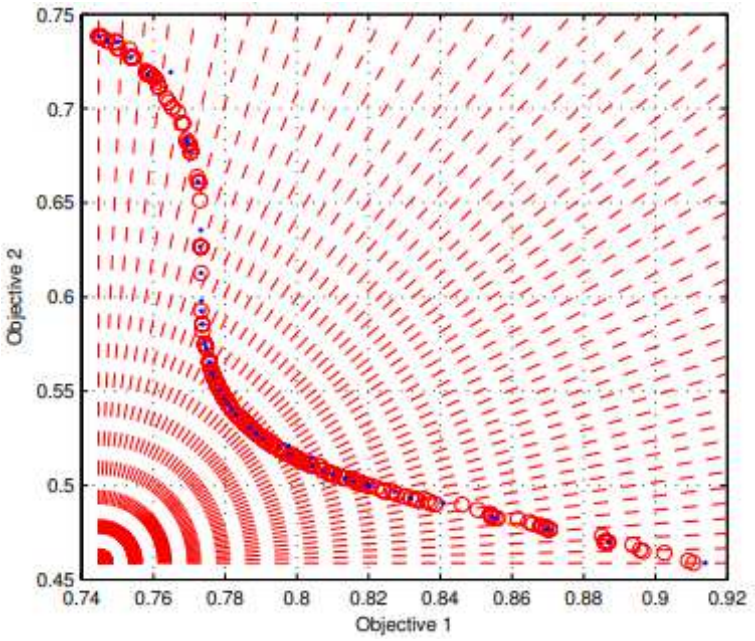

Figure 34 – Example of the converged simulation for 50 automatically generated target vectors, showing sufficiently uniform spreading in angle across the objective surface - Withdrawal of [14]

To evaluate the dominance relationship between solutions, the following metric is defined:

$$\phi(r,x) = [\xi(t)\frac{\theta(r,x) - \theta_{min}}{\theta_{max} - \theta_{min}} + (1 - \xi(t)\frac{D(r,x) - D_{min}}{D_(max) - D_{min}}] \times (1 + \frac{1}{e^m}) \tag{4.1}$$

where m is the number of objectives, $\xi(t)$ is the adaptive weight, t is the iteration number, θ refers to the preference angles and D to the distance of the reference points.

The ar-dominance must have a strong convergence pressure in the first iterations and guide the population to the Pareto front, for this, the distance information must be a priority. In the last stage of the iteration, diversity is a priority, so the angle metric between each solution and the reference point should be more considered. Because of these aspects, $\xi(t)$ should vary adaptively over the iterations:

$$\xi(t) = \xi_{min} + (\xi_{max} - \xi_{min})e^{-(1-\frac{t}{T})} \tag{4.2}$$

where T is the maximum number of iterations.

The ar-dominance relationship algorithm can be seen in Figure 35. In addition to these aspects, another variable called the adaptive threshold δ is also used, which is applied to control the distribution of solutions by constraining the metric ϕ. More details of the method, as well as its use in benchmark problems, can be found in the literature [15].

ar-Dominance Relationship

Input: Reference point r, solutions p_1 and p_2.
Output: The domination relationship between p_1 and p_2, the elitist one solution p'.

```
/*Pareto principle domination comparison*/
if p1 ≺ p2 then
    p1 ≺ar p2, p' ← p1; //the ar-dominance relationship is represented by symbol ≺ar
end if
if p2 ≺ p1 then
    p2 ≺ar p1, p' ← p2;
end if
/*ar-dominance comparison*/
if p1 and p2 are Pareto-equivalent then
    Calculate φ(r, p1) and φ(r, p2); //refer to Eq.(4)
    if φ(r, p1) − φ(r, p2) < −δ then
        p1 ≺ar p2, p' ← p1;
    else
        if φ(r, p2) − φ(r, p1) < −δ then
            p2 ≺ar p1, p' ← p2;
        else
            p1 and p2 are ar-dominance equivalent;
            p' ← Randomly − Choose(p1, p2);
        end if
    end if
end if
```

Figure 35 – ar-Dominance Algorithm - Withdrawal of [15]

4.3.4 AGEMOEA

Panichella [16] sought to develop an algorithm capable of generating good results, that is, a Pareto front with good diversity and proximity. For this, it was proposed the AGEMOEA (Adaptive Geometry Estimation based Multi-objective Evolutionary Algorithm) which:

- estimates the geometry of the Pareto front generated using a fast procedure of computational complexity O(M × N) (where M is the number of objectives and N is the population size);
- adapts the diversity and proximity metrics accordingly.

AGEMOEA modifies NSGAII by replacing fitness scores that are assigned to each non-dominated front. In AGEMOEA, the NSGAII crowding distance is replaced by the survival score, which is a metric that combines both diversity and proximity of non-dominated solutions. Figure 36 displays the code for attributing the survivor score:

SURVIVAL-SCORE

Input:
$\mathbb{F}_d$: pool of non-dominated solutions
d: index of the non-dominated front
p: exponent of estimated geometry the p-norm

1 **begin**
2 **if** $d==1$ **then**
3 score$[E] \longleftarrow +\infty$ /* E = extreme points of $\mathbb{F}_1$ */
4 $\Omega \longleftarrow$ E /* Considered solutions */
5 $\overline{\Omega} \longleftarrow \mathbb{F}_d \setminus \Omega$ /* Remaining solutions */
6 **for** *each solution* $S \in \overline{\Omega}$ **do**
7 proximity$[S] \longleftarrow \|f(S)\|_p$
8 **for** *each solution* $S_1 \in \mathbb{F}_d$ **do**
9 **for** *each solution* $S_2 \in \mathbb{F}_d$ **do**
10 dist$[S_1, S_2] \longleftarrow \|f(S_1) - f(S_2)\|_p$
11 **while** $|\overline{\Omega}| > 0$ **do**
12 **for** *each* $S \in \overline{\Omega}$ **do**
13 diversity$[S] \longleftarrow \min_{T \in \Omega} \text{dist}[S, T] + \min2_{T \in \Omega} \text{dist}[S, T]$
14 $\text{value}[S] \longleftarrow \dfrac{\text{diversity}[S]}{\text{proximity}[S]}$
  /* Select the solution with the max value */
15 $S^* \longleftarrow \arg\max_{S \in \overline{\Omega}} \text{value}[S]$
16 score$[S^*] \longleftarrow$ value$[S^*]$
17 $\Omega \longleftarrow \Omega \bigcup \{S^*\}$ /* Considered solutions */
18 $\overline{\Omega} \longleftarrow \overline{\Omega} \setminus \{S^*\}$ /* Remaining solutions */
19 **else**
20 **for** *each* $S \in \mathbb{F}_1$ **do**
21 score$[S] \longleftarrow 1/\|f(S)\|_p$

Figure 36 – Survival Score Algorithm - Withdrawal of [16]

As can be seen in line 14 of Figure 36, the survival score is given by:

$$SurvivalScore(S) = \frac{diversity}{proximity} \tag{4.3}$$

By Equation 4.3 it is observed that the survival score will be better the greater the diversity and the smaller the proximity. The rest of the AGEMOEA works basically like the NSGAII, with minor modifications that can be seen in the literature [16]

4.3.5 NSGAIIARSBX

The crossover operation is indispensable for the generation of good offspring solutions in the context of MOEAs. Among several crossover operators, the Simulated Binary Crossover (SBX) is widely used in different MOEA algorithms. Although the SBX is quite effective in solving problems with regular Pareto fronts, its performance suffers when studying problems with rotated ones. To deal with this issue, Pan Et al. [17]

proposes a modified SBX, named Rotation-based Simulated Binary Crossover (RSBX), to improve the performance of MOEAs in problems where the Pareto front is not parallel with the design variables.

The general idea is to rotate solutions in the decision space through a rotation matrix calculated through the covariance of the current population matrix. Then, an adaptive operator selection strategy is proposed to seek the best overall performance of different multi-objective problems.

At first, the rotated matrix V is initialized as an identity matrix, and the mean vector is initialized as the central values of each of the design variables. Afterward, the mating selection algorithm is used to determine the parent solutions. Then, the SBX is executed with a probability p_s, while the RSBX is executed at $1 - p_s$, generating the offspring solutions, and the conventional operators of the MOEA are executed. Finally, the rotated matrix V, the current population vector, and the probability p_s are updated. The pseudocode of this process can be seen in Figure 37.

Framework of MOEA-ARSBX

Require: N (population size)
Ensure: $POP^{(g_{max})}$ (final population).
1: Initialize population $POP^{(o)}$
2: Initialize mean vector **m** and rotation matrix **V**
3: Initialize probability p_s
4: **for** $g \leftarrow 0$ to g_{max} **do**
5: Select N individuals from $POP^{(g)}$
6: $Q \leftarrow \emptyset$
7: **for** $i \leftarrow 0$ to $N/2$ **do**
8: **if** $rand < p_s$ **then**
9: $\mathbf{V} \leftarrow \mathbf{I}$
10: $\mathbf{m} \leftarrow \mathbf{0}$
11: **else**
12: $\mathbf{V} \leftarrow$ Calculate the rotation matrix by using (7)
13: $\mathbf{m} \leftarrow$ Calculate the mean vector by using (5)
14: **end if**
15: $\mathbf{P} \leftarrow \mathbf{V}(\mathbf{P}^{(g)} - \mathbf{m})$
/*P denotes the set of decision vectors of the population*/
16: $\mathbf{q} \leftarrow$ Generate decision vectors by SBX
17: $\mathbf{q} \leftarrow \mathbf{V}^{-1}\mathbf{q} + \mathbf{m}$ /*$\mathbf{V}^{-1}$ is the inverse matrix of **V***/
18: $Q \leftarrow Q \cup \{\mathbf{q}\}$
19: **end for**
20: $POP^{(g+1)} \leftarrow$ Select N individuals from $POP^{(g)} \cup Q$
21: Calculate the covariance matrix **C** by (6)
22: Update **V** and **m** by current population by (7) and (5), respectively.
23: Update p_s by (9)
24: **end for**

Figure 37 – ARSBX Framework Algorithm - Withdrawal of [17]

The NSGAIIARSBX algorithm is the coupling of NSGAII with RSBX, making it capable of dealing with problems that have non-traditional Pareto fronts as solutions.

5 Development

In this Chapter, the steps followed to develop the optimization methodology created are described. The process of developing such algorithms is a task that involves several approaches to compatibility, modifications, and couplings of different existing codes and software and the creation of new ones. The problem resulting from the union of these codes and software was added to PlatEMO and called OptProp. In subsequent Sections, such approaches are exposed.

5.1 Airfoil Database Creation and Analysis

5.1.1 Airfoil Database

The first step taken in the development was the search for a database that included a wide variety of aerodynamic airfoils. The UIUC Airfoil Coordinates Database [111] has approximately 1500 airfoils, including several families already consolidated in the aeronautical field and in the literature: NACA, EPPLER, SELIG, Drela, Gottingen, Wortmann.

The airfoil database is made available in a compressed file (*.zip*) that has each airfoil in the format *.dat*. Such files are formatted as shown in Table 1.

Line 1	Airfoil name	
Next lines	X coordinates	Y coordinates

Table 1 – Airfoil *.dat* format

5.1.2 Airfoil Refinement

Airfoils obtained through the University of Illinois Urbana-Champaign (UIUC) Airfoil Coordinates Database have different numbers of coordinate points. Airfoils with an insufficient number of points, when placed under analysis in XFOIL, have their convergence impaired and decreased results reliability. To solve this problem, an algorithm has been developed using the function *interpac* [112]. An average total of 200 points was set for the refined airfoils. Generally, XFOIL achieves good convergence between 100–150 points, as indicated by Deperrois [113]. The points were distributed to concentrate on the first 15% of the airfoil chord, both in the upper and lower lines, approximately 70% of the points. This approach was chosen because the leading edge has bigger curvature and therefore needs more points to be smooth. As an example, the graphical result of the process can be seen in Figure 38.

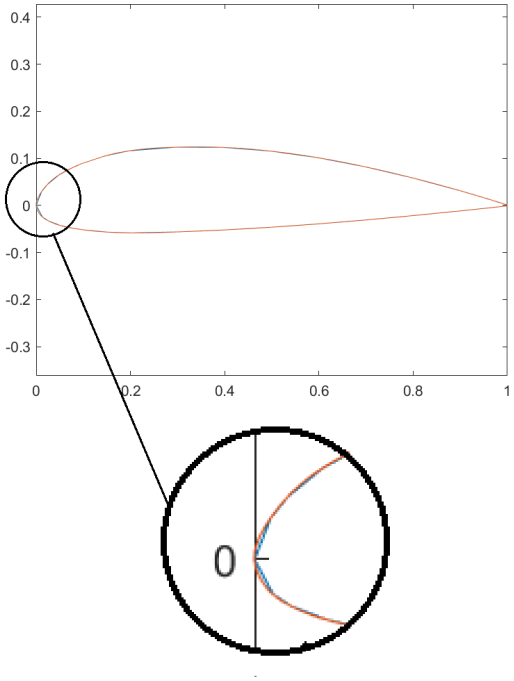

Figure 38 – Visualization of refinement algorithm results on airfoil - the blue line is the original airfoil and the orange one is the refined airfoil.

5.1.3 Airfoil Analysis

The refined airfoils using the method described in the previous Section were exported in the open software XFLR5, which uses the open-source XFOIL, based on the panel method. For each of the initial profiles obtained from the UIUC Airfoil Coordinates Database, the following analysis criteria were used: angle of attack range between $-60°$ and $60°$, with $0.5°$ increment, Reynolds number of 5×10^4, 10^5, 5×10^5, and 10^6, both top and bottom forced transitions were located at section position 1.00 x/c. The NCrit used for the panel method simulations was equal to 9.00 and the Mach number was equal to 0, while the maximum number of iterations was set to 100. The analysis was executed with 8 CPU multithreaded. Figure 39 shows a set of $Cl \times \alpha$ curves for several profiles.

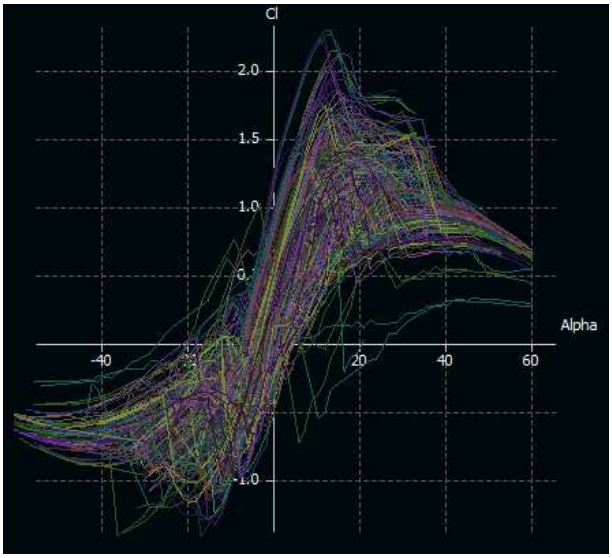

Figure 39 – $Cl \times \alpha$ curves for a batch of database airfoils

Each of the analyzed profiles generates four output files, each for one of the Reynolds numbers used in the simulations. Figure 40 displays one of these output files.

```
xflr5 v6.47

 Calculated polar for: HQ 3.5 8 AIRFOIL

 1 1 Reynolds number fixed          Mach number fixed

 xtrf =   1.000 (top)        1.000 (bottom)
 Mach =   0.000     Re =     1.000 e 6     Ncrit =   9.000

  alpha     CL        CD       CDp       Cm    Top Xtr Bot Xtr   Cpmin    Chinge    XCp
 ------- -------- --------- --------- -------- ------- ------- -------- --------- ---------
 -13.500  -0.4197   0.14986   0.14811  -0.0192  1.0000  0.0039  -1.7348   0.0000   0.1963
 -12.000  -0.3837   0.13238   0.13068  -0.0249  1.0000  0.0044  -1.7831   0.0000   0.1779
 -10.500  -0.3597   0.11535   0.11372  -0.0280  1.0000  0.0049  -1.8924   0.0000   0.1658
  -9.000  -0.3353   0.09732   0.09578  -0.0336  0.9986  0.0055  -2.0180   0.0000   0.1445
  -7.500  -0.2525   0.07351   0.07199  -0.0597  0.9843  0.0063  -2.0844   0.0000   0.0077
  -3.000   0.1553   0.00896   0.00381  -0.1073  0.8693  0.0094  -2.7584   0.0000   0.9461
  -1.500   0.3210   0.00675   0.00124  -0.1066  0.8189  0.0122  -1.3956   0.0000   0.5830
   0.000   0.4849   0.00479   0.00098  -0.1068  0.7629  0.7236  -0.6138   0.0000   0.4696
   3.000   0.8026   0.00569   0.00152  -0.1033  0.5280  1.0000  -1.0458   0.0000   0.3755
   4.500   0.9435   0.00839   0.00291  -0.0994  0.2369  1.0000  -1.8917   0.0000   0.3508
   6.000   1.0719   0.01224   0.00553  -0.0936  0.0059  1.0000  -3.4614   0.0000   0.3311
   7.500   1.2030   0.01544   0.00898  -0.0877  0.0044  1.0000  -5.4369   0.0000   0.3149
   9.000   1.2976   0.02069   0.01467  -0.0760  0.0043  1.0000  -7.3453   0.0000   0.2986
```

Figure 40 – Exit file format for XFLR5 exported polar

The next step was to transform the data obtained and exported from XFLR5 into data that could be read using JAVAPROP. For this, two routines were created in MATLAB, *polar2mat.m* and *mat2afl.m*. The *.afl* extension is one of the native extensions for importing non-native airfoils to JAVAPROP. An example of *.afl* data is exhibited in Figure 41.

```
(Dicke 12.28%)     0.050 e 6
This is an airfoil polar file for JavaProp. It can have up to 1000 data triples.
This format will be changed to my airfoil-polar-XML form in a future release.
---------------------------------------------------------------
alpha   cl              cd              cm
-21.000000 -0.641800 0.254840 0.060700
-19.500000 -0.607700 0.235850 0.049000
-18.000000 -0.571700 0.215290 0.037700
-16.500000 -0.550000 0.201290 0.025600
-15.000000 -0.552400 0.185790 0.013400
-13.500000 -0.541100 0.163730 0.006400
-12.000000 -0.541600 0.140660 0.001300
-10.500000 -0.680100 0.079230 -0.035900
-9.000000 -0.800700 0.054590 -0.027400
-7.500000 -0.754200 0.034450 -0.014400
-6.000000 -0.694900 0.024900 0.007700
-4.500000 -0.535400 0.032350 0.030800
-3.000000 -0.278800 0.032290 0.020100
-1.500000 -0.163000 0.030720 0.017400
0.000000 0.000000 0.030480 0.000000
1.500000 0.162800 0.030710 -0.017400
3.000000 0.278700 0.032270 -0.020000
4.500000 0.535600 0.032340 -0.030800
6.000000 0.694900 0.024900 -0.007700
7.500000 0.764200 0.034700 0.013800
9.000000 0.813500 0.053480 0.027100
10.500000 0.692800 0.077060 0.036400
12.000000 0.541900 0.140660 -0.001400
13.500000 0.541400 0.163710 -0.006500
15.000000 0.554400 0.186120 -0.013300
16.500000 0.550100 0.201320 -0.025600
18.000000 0.571700 0.215280 -0.037700
19.500000 0.607600 0.235810 -0.048900
21.000000 0.641400 0.254680 -0.060700
22.500000 0.670800 0.274980 -0.073500
```

Figure 41 – JAVAPROP *.afl* extension used for importing non-native airfoils

5.2 Blade Element Momentum Theory and Optimization Coupling

5.2.1 JAVAPROP Automation for MATLAB

JAVAPROP, software that uses the BEMT method for propeller analysis, was presented in Subsection **4.2.1** of the present work. Although the original program uses an interface programmed in *Java* language, an automation that makes it possible to run the code through other languages has also been implemented. For the study carried out here, automation in MATLAB was used [114].

The function *DesignProp.m* was used to run the propeller design process through a group of inputs (Table 2). In the Subsection *5.2.2.1*, modifications made to the original function are explained, as well as the coupling process with the objective and optimizing functions.

Input	Dimension
Number of sections	-
Air density	kg/m^3
Air kinematic viscosity	m^2/s
Speed of sound	m/s
Sections airfoils	-
Sections angles of attack	degree
Diameter	m
Spin diameter	m
Airspeed	m/s
Rotational Speed	rpm
Power	W
Thrust	N
Torque	N.m

Table 2 – *DesignProp.m* JAVAPROP code inputs

5.2.2 PlatEMO

Since the creation of the first evolutionary algorithm and with the perception that the increase in contemporary computational capabilities would make this type of method interesting, many researchers have dedicated themselves to this area and have proposed hundreds of different codes, with increasingly creative approaches and algorithms capable of solving broader problems. However, these algorithms were not arranged in any way that made them easily usable, being written in different computational languages, and some of them did not even have public source code. So that researchers could test new codes, compare them with existing ones through benchmark codes, and solve real-world problems, libraries of MOEAs emerged, capable of gathering codes, problems, performance indicators, and tools related to carrying out evolutionary optimizations.

One of the main software related to the theme is PlatEMO (Platform for Evolutionary Multi-Objective Optimization), written in MATLAB language by Tian *et al.* [115]. Compared to other software, PlatEMO has the following main advantages:

- At the time of writing this text, PlatEMO has 216 MOEAs and 432 benchmark problems, with several popular algorithms: multi-objective genetic algorithms, multi-objective differential evolution algorithms, multi-objective particle swarm optimization algorithms, multi-objective estimation of distribution algorithms, surrogate-assisted multi-objective evolutionary algorithms;
- important metrics such as coverage, generational distance (GD), hypervolume (HV), inverted generational distance (IGD), normalized hypervolume (NHV), pure diversity (PD), spacing, and spread, among others, are integrated into the software;

- the software is fully developed in MATLAB language, therefore, any machine that has MATLAB software installed will be able to use PlatEMO, regardless of the operating system installed. Through the GUI, the user does not need to write additional codes to configure his experiment, in addition to having facilities for exporting the result to Excel and LaTeX environments. The PlatEMO test module is shown in Figure 42.

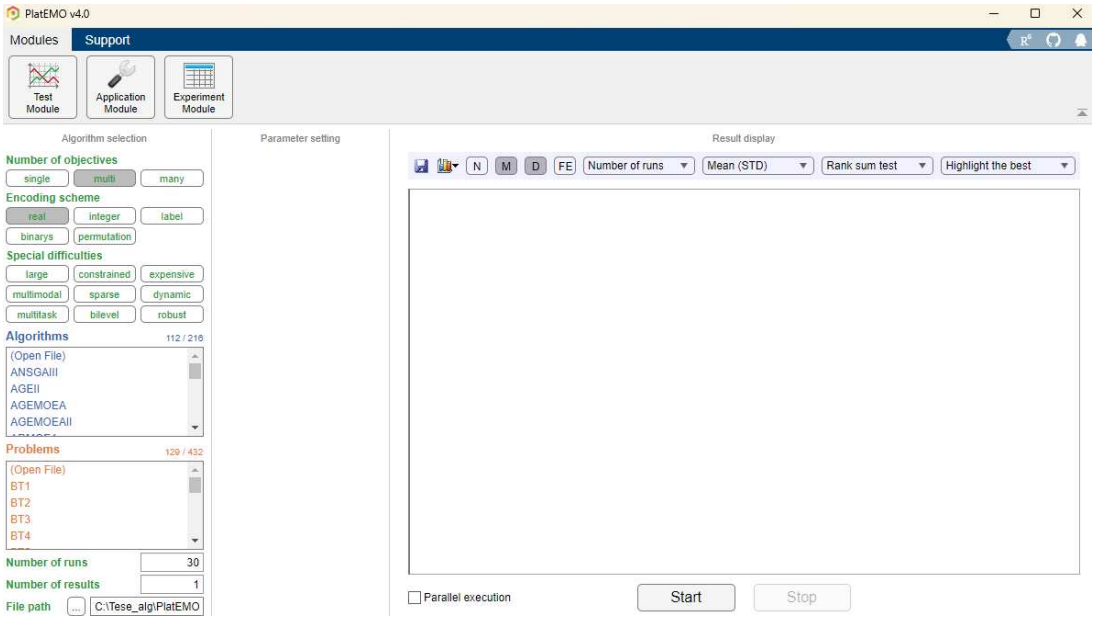

Figure 42 – PlatEMO test module screen

The evolutionary algorithms used through PlatEMO to obtain the results of this work were described in Section 4.3.

5.2.2.1 Codes Development and Coupling

This Section describes how the analysis and optimization codes were developed, as well as the coupling between them.

5.2.2.2 *DesignProp.m* Development

DesignProp.m is the function responsible for doing the aerodynamic analysis of a given propeller. The code receives initial data such as the properties of the air (density, speed of sound, and kinematic viscosity), data related to the mission, such as airspeed, required power, required thrust, and finally the propeller data itself: airfoils along the chord, diameter, number of blades, rotational speed, and the ratio between total and hub diameter.

Four sections were used for the analysis of the propellers, where different aerodynamic profiles can be selected. In positions between two sections, the resulting profile is an

interpolation between the two closest section profiles. Of the approximately 1500 profiles analyzed initially, 6110 polar files were generated, since some combinations of airfoils and Reynolds numbers were not able to generate results through the analysis performed by the panel methods. Although all analyzes were performed between $-60°$ and $60°$ for the angle of attack, most profiles do not generate results in the entire analysis range. For this reason, required values were stipulated to use the profiles in each of the four sections. The required angle ranges as well as the positioning of the section are shown in Table 3.

Section Number	1	2	3	4
Section Position (x/c)	0	1/3	2/3	1
Minimum AoA (°)	-20	-20	-15	-15
Maximum AoA (°)	40	30	20	15

Table 3 – Airfoil sections specifications

AoA criteria are used as constraint functions of the optimization.

Through the input data, *DesignProp.m* loads the data of the airfoils used in the propeller. These data can be divided into two groups:

- aerodynamics: drag, lift, and moment coefficients for different Reynolds numbers;
- geometric: dimensionless area, dimensionless moments of inertia, principal axis of inertia angle, and dimensionless polar moment.

From the airfoil's aerodynamic data and the remaining necessary characteristics, the program uses a code coupled to JAVAPROP, which creates a propeller with chord and twist angle distribution through Rankine's theory. From these data, the code can generate the absolute geometric characteristics for each of the propeller sections. Finally, propeller aerodynamic data is generated. At this point, the function analyzes the value of the average Reynolds number of each of the four sections and checks if it is close enough to the one used in the propeller generation. If not, the propeller obtained will be indicated as constrained in relation to the Reynolds number in the corresponding sections.

In Table 4 it is possible to view the optimization variables. The Airfoil/Polar section variables and the Number of Blades variables are integer variables, while all the others are real variables.

Variable	Dimension
Airfoil/Polar Section #1	-
Airfoil/Polar Section #2	-
Airfoil/Polar Section #3	-
Airfoil/Polar Section #4	-
Thrust	N
Power	W
Rotational Speed	RPM
Airspeed	m/s
Propeller Diameter	m
Number of Blades	-
Hub Diameter/Propeller Diameter	-

Table 4 – Optimization variables for *DesignProp.m*

The outputs obtained from the code are all geometric information of the propeller, as well as aerodynamic performance information such as thrust, torque, real power, torque, power and momentum coefficients, and efficiency. The complete list of variables obtained can be found in the JAVAPROP User's Guide [103].

5.2.2.3 OptProp.m Development

OptProp.m is a class definition file that makes the direct connection to PlatEMO. This code loads the JAVAPROP analysis files (*JAVAPROP.jar* and *MHClasses.jar*), as well as the PlatEMO paths and folders. After loading, the optimization options such as population size, number of generations, number of objectives, number of design variables, number of constraints, lower and upper limits of variables, and types (real or integer) of variables are configured. Here, it is also defined which version of *prop_objfun.m* will be used by the optimization.

As this code is responsible for being the link between the PlatEMO optimizer and all other aspects developed, such as the airfoil database, the BEMT code and its specificities, and the structural code that will be presented in the Subsection 5.3, the method created was also named OptProp.

5.2.2.4 prop_objfun.m Development

This function is responsible for receiving values that will be used throughout the optimization, such as thrust, airspeed, and power in different conditions. It is also responsible for indicating to PlatEMO what the design variables, objective functions, and constraints will be. After calculating the objective functions and constraints through *DesignProp.m*, *prop_objfun.m* will pass them on to *OptProp.m* to work on in the optimization process. In this way, the function described here can be understood as an intermediary function

between two others, which simplifies the configuration of project variables, objective functions, and constraints, making the data flow more efficient.

5.3 Structural Code

This Section shows the development of a structural analysis code for cantilever beams with twist angle and rotational speed. The code is based on that developed by Rao [8], presented in Section 2.5. Rao determines each section of the cantilever beam as a rectangle and uses the width and length of each of these as inputs:

The code used in this present thesis is adapted from the algorithm proposed by Rao, however, instead of the inputs being rectangles dimensions, were used as inputs areas and moments of inertia of each section. This allows the code to be able to handle geometries with more complex sections, such as airfoils.

5.3.1 Taper & Twist Validations

Table 5 shows the geometric data of four different beams simulated in the code and in the Modal/ANSYS module. They can also be seen in Figures 43, 44, 45, and 46.

	h_1 (m)	b_1 (m)	h_2 (m)	b_2 (m)	Twist (^{o})
Simple	0.03	0.02	0.03	0.02	0
Taper	0.03	0.02	0.015	0.008	0
Twist	0.03	0.02	0.03	0.02	60
Taper & Twist	0.03	0.02	0.015	0.008	30

Table 5 – Geometric properties of beams

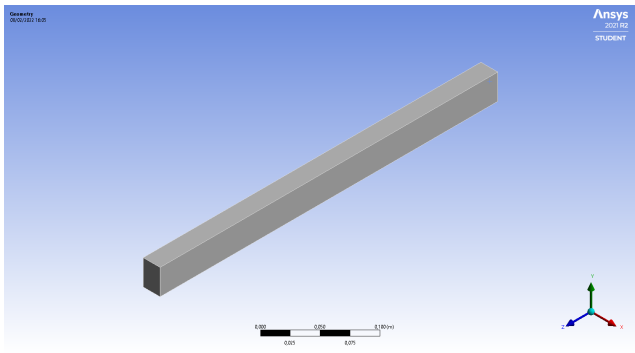

Figure 43 – Simple beam

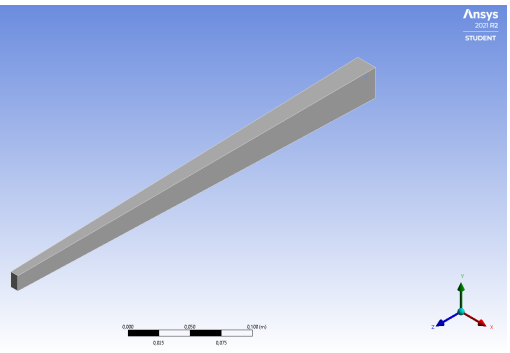

Figure 44 – Taper beam

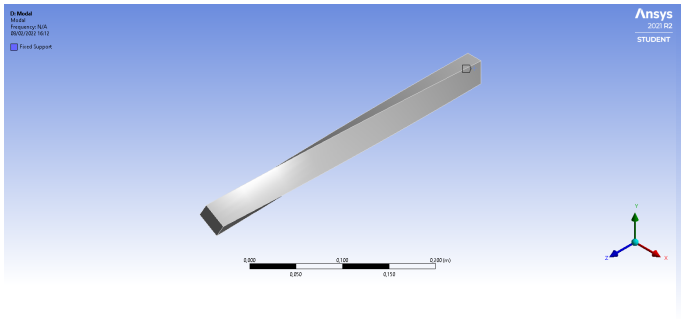

Figure 45 – Twist beam

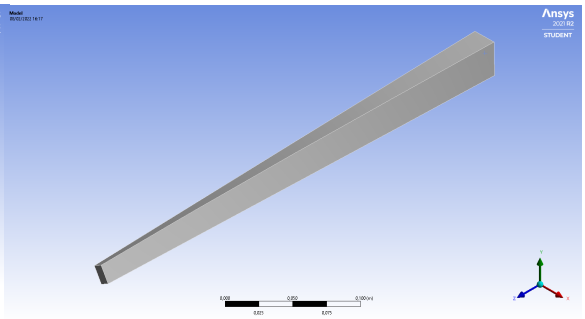

Figure 46 – Twist & taper beam

Table 6 shows the results obtained for the first six natural frequencies for each beam using the two methods. MATLAB results were obtained through the discretization of 8 elements, while those obtained by Modal/ANSYS (3D - FEM) had around 200 elements. Figure 47 shows an error chart for each of the beams at the six frequencies.

		f_1	f_2	f_3	f_4	f_5	f_6
Simple	MATLAB	102.66	153.91	641.57	958.40	1789.08	2657.50
	Modal/ANSYS	102.16	152.72	632.98	933.22	1741.50	2517.00
	Error	0.49%	0.77%	1.34%	2.63%	2.66%	5.29%
Taper	MATLAB	138.70	214.73	546.82	874.35	1325.98	2138.48
	Modal/ANSYS	137.42	212.52	538.84	855.12	1296.50	2054.30
	Error	0.92%	1.03%	1.46%	2.20%	2.22%	3.94%
Twist	MATLAB	102.60	151.35	628.96	932.94	1735.70	2551.30
	Modal/ANSYS	102.84	150.33	648.43	903.61	1800.80	2417.00
	Error	0.24%	0.68%	3.00%	3.25%	3.62%	5.56%
Taper & Twist	MATLAB	138.14	213.11	543.34	861.72	1317.79	2081.05
	Modal/ANSYS	137.51	210.67	544.23	843.46	1316.40	2013.30
	Error	0.46%	1.16%	0.16%	2.16%	0.11%	3.36%

Table 6 – Results obtained for natural frequencies (Hz) of the beams

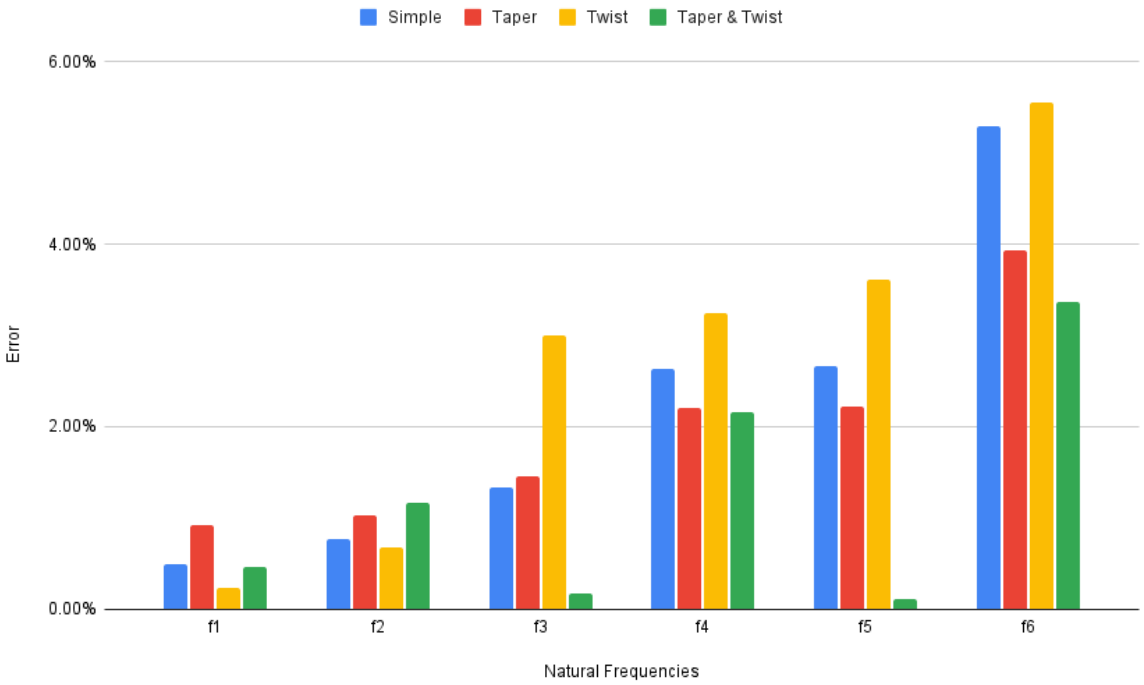

Figure 47 – Error obtained for the algorithm against Modal/ANSYS

As seen in Table 6 and Figure 47, the error for the first natural frequency is less than 1% between the results of the code developed and obtained by Modal/ANSYS. The error increases for higher natural frequencies, being between 3-5%. Such behavior can be explained by computational errors being more present in higher-order frequencies.

5.3.2 Rotational Speed Validations

The results obtained by the algorithm developed considering the influence of rotation on the first four vibration frequencies are presented in Table 7. Table 8 and Figures 48 and 49 show the results for the frequency ratio, which is the ratio between the natural frequency of a given mode and given rotation and the first non-rotating frequency. A no-twisted beam with a length of 0.31 m and section dimensions of 0.00865m and 0.027161m was used.

ω (RPS)	f_1	f_2	f_3	f_4
0	73.93	231.87	464.33	1308.73
100	70.74	230.90	464.02	1311.05
200	59.14	227.91	462.67	1317.97
300	23.29	222.76	459.00	1329.32

Table 7 – Rotating natural frequencies (Hz)

ω (RPS)	fr_1	fr_2	fr_3	fr_4
0	1.00	3.14	6.28	17.70
100	0.96	3.12	6.28	17.73
200	0.80	3.08	6.26	17.83
300	0.32	3.01	6.21	17.98

Table 8 – Rotating frequency ratios

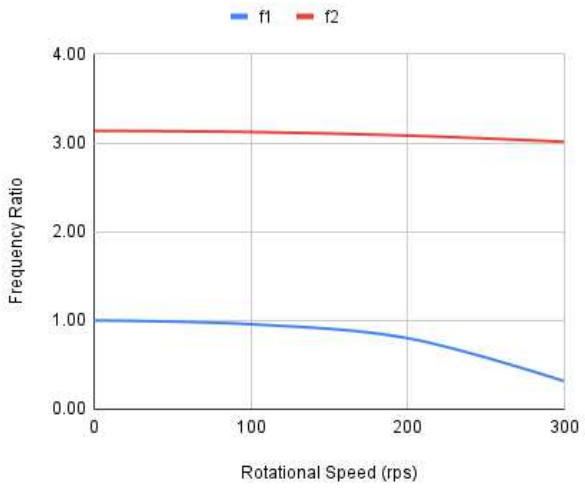

Figure 48 – Frequency ratio for first and second modes

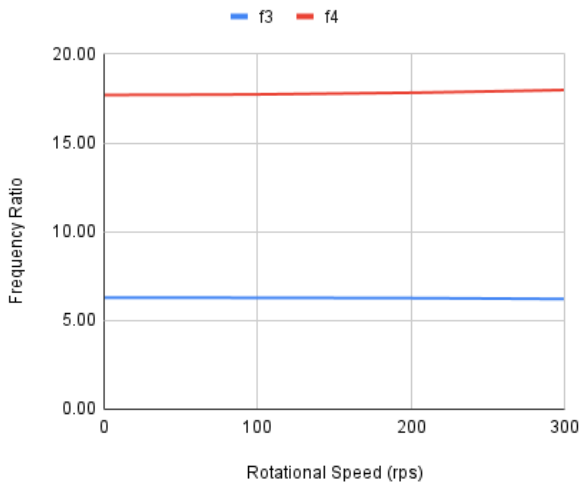

Figure 49 – Frequency ratio for third and fourth modes

Figures 21 and 23 show the results obtained by Rao [8]. As the author does not specify all the characteristics of the beam, a configuration that approximated the results

was used. Comparing the results obtained, it is possible to observe the same behavior in both cases. The rotation has a big influence on the decrease of the first natural frequency, a small influence on the decrease in the second, as well as a small increase in the fourth frequency. The third frequency of the bibliography showed a small increase, while the proposed approximate beam remained with almost no difference. Such behavior can be explained by the impossibility of knowing which beam dimensions were used by Rao [8].

5.3.3 Propeller Validation

As the last validation test for the structural code, it was proposed a propeller that, like the beams, was simulated by the created structural analysis and the FEM analysis of Modal/ANSYS.

The propeller used, shown in Figure 50, has two blades, a diameter of 2 m, a maximum chord of 20 cm, a root twist angle of 54°, and the airfoil used is NACA2415. The diameter of the hub in relation to the diameter of the propeller is 8%.

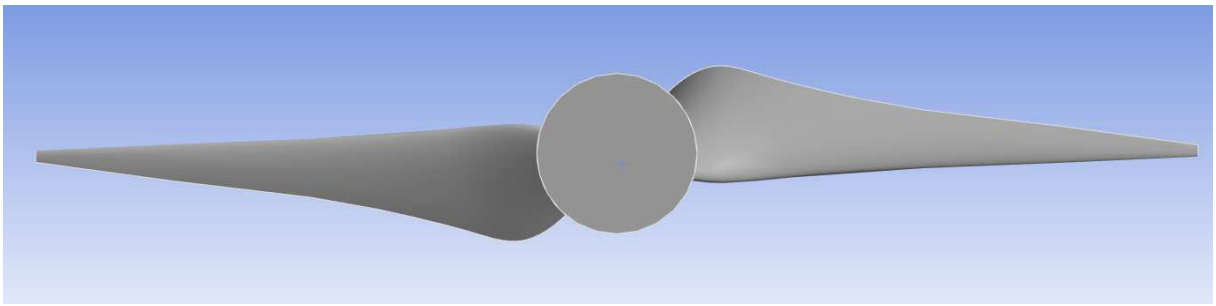

Figure 50 – Propeller used for structural validation

The mesh generated for use in Modal/ANSYS has 111,306 nodes and 69,123 elements. The simulation setup was performed using the rotational frequency of 314.16 rad/s.

		Modal/ANSYS		Structural Code	
Rotational Velocity (rad/s)		0	314.16	0	314.16
Mode (Hz)	1	55.8	55.3	56.0	57.4
	2	144.7	146.0	150.5	150.9

Table 9 – Comparative table of modal frequency data obtained by propeller simulation

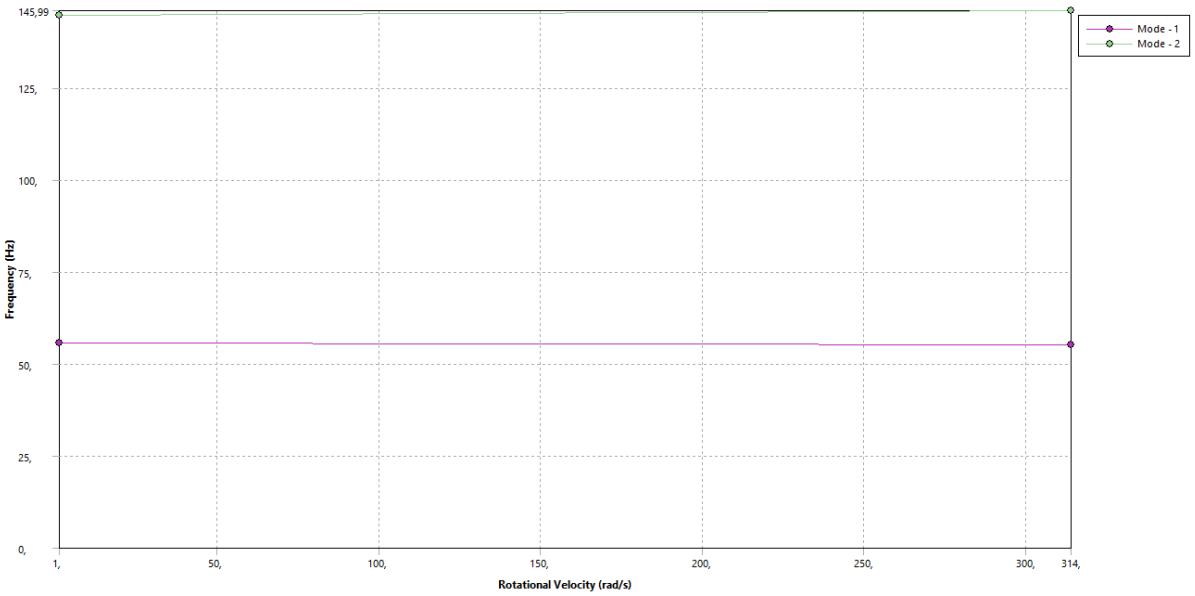

Figure 51 – Campbell diagram generated by Modal/ANSYS for the proposed propeller

The obtained data are shown in Table 9 and Figure 51. The difference between the values obtained between the two methods is less than 5% for all points.

6 Multi-objective Optimum Design of Propellers using BEMT and Evolutionary Algorithms

In this Chapter, the first set of results obtained by OptProp will be displayed. Section 6.1 executes a validation between the results obtained by the chosen BEMT code (JAVAPROP), Computational Fluid Dynamics (CFX - ANSYS), and experimental results. In Section 6.2 general optimizations of propeller dimensionless parameters are performed.

6.1 Method Validation - SR2 Propeller

In this Section, the validation of the BEMT method used to obtain the characteristics of propellers will be dealt with. The SR2 propeller will be used for this, as this has been exhaustively treated in the literature, and the validation will be executed using CFD.

Tan [18] provides a geometry analysis of the SR2 propeller based on the literature ([116, 117, 118, 119]). The blade section profile consists of a NACA65 2D section from root to 37% span and a NACA 16 2D airfoil from 44% to the blade tip. A transition of cross-sections lies between 37% to 44%. The blade reference angles used in this work are 59 and 53.8 degrees, measured at 75% blade span location. The geometric data are shown in Figure 52.

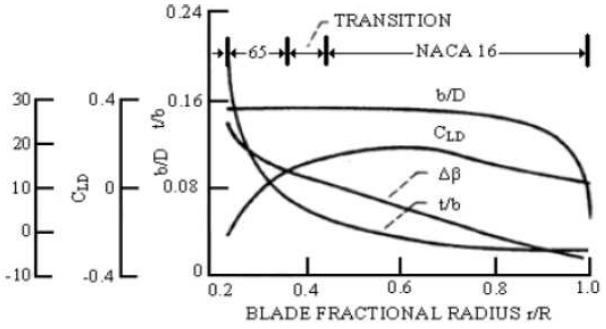

Figure 52 – SR2 Propeller Geometry - Withdrawal from [18]

Through such data, it was possible to create a three-dimensional mesh of the SR2 Propeller that can be visualized in Figure 53:

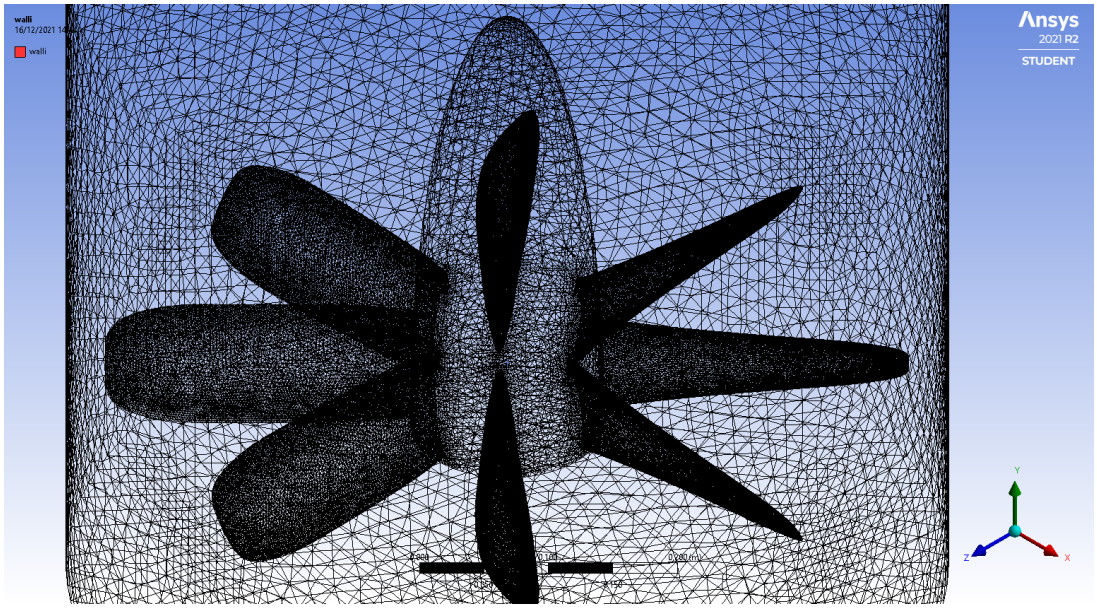

Figure 53 – 3D Mesh - SR2 Propeller

Two simulation groups were performed. The first with a fixed Advance Ratio of 3.06 and Mach ranging from 0.6 to 0.9. The second was with Mach fixed at 0.34 and varying the Advance Ratio from 1.3 to 3.2. Simulation results are shown in Figures 54 and 55 and Tables 10 and 11:

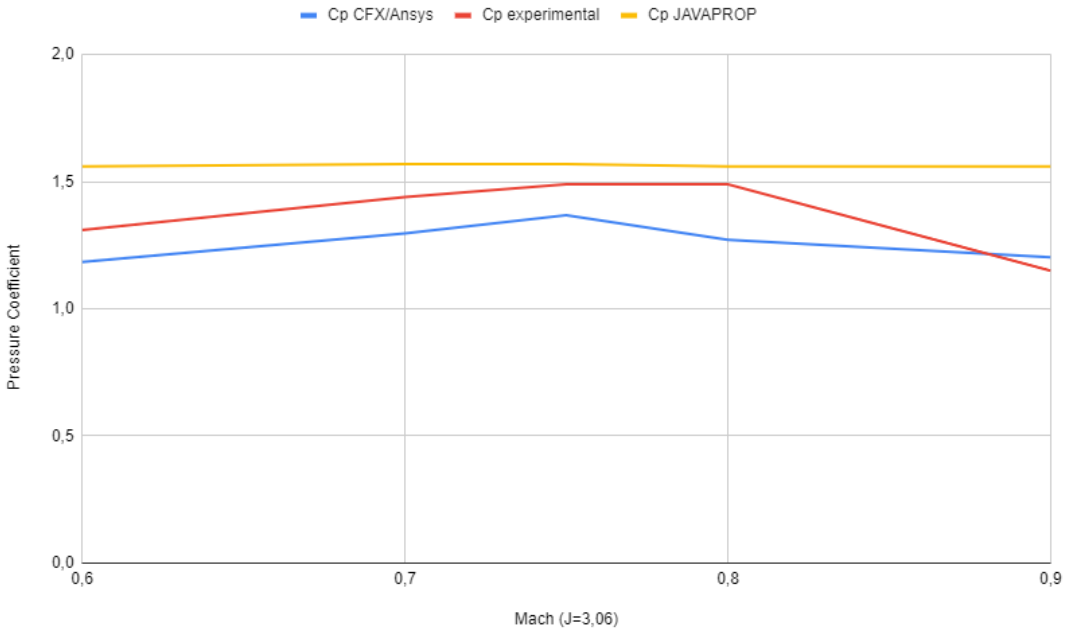

Figure 54 – C_P - experimental wind tunnel, CFX/ANSYS, and JAVAPROP results for high Mach numbers and $J = 3.06$

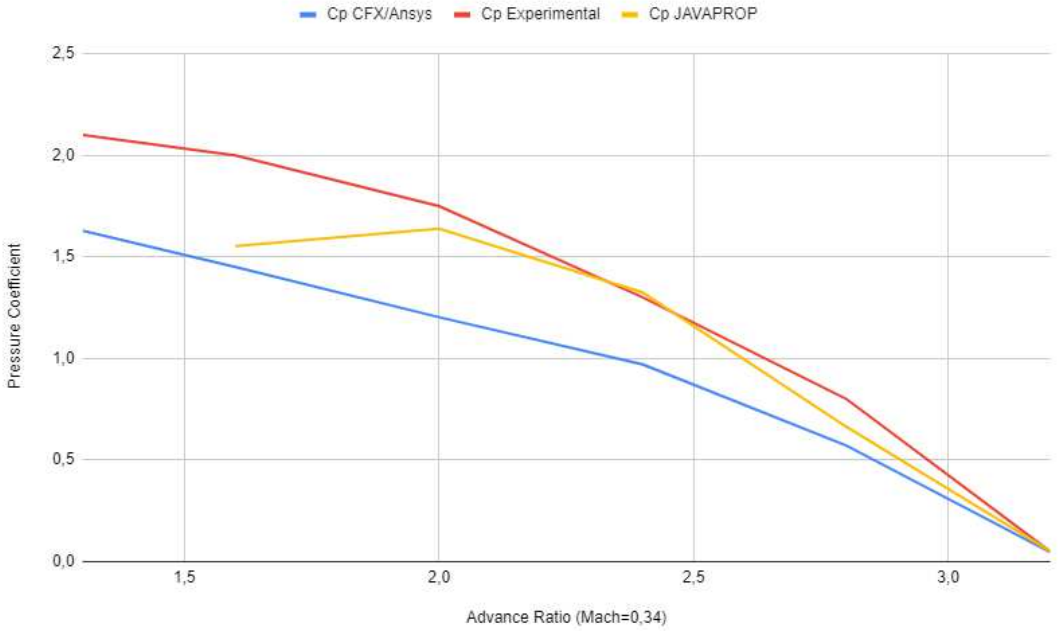

Figure 55 – C_P - experimental wind tunnel, CFX/ANSYS, and JAVAPROP results for Mach number 0.34

$\beta_{3/4}$ (º)	J	Mach	C_P CFX	C_P JP	C_P Exp [119]	ϵ Exp-CFD	ϵ Exp-JP
59	3.06	0.60	1.184	1.56	1.31	9.6%	-19%
59	3.06	0.70	1.296	1.57	1.44	10.0%	-9%
59	3.06	0.75	1.368	1.57	1.49	8.2%	-5%
59	3.06	0.80	1.272	1.56	1.49	14.7%	-5%
59	3.06	0.90	1.203	1.56	1.15	-4.6%	-36%

Table 10 – C_P - experimental wind tunnel, CFX/ANSYS, and JAVAPROP results for higher Mach numbers and $J = 3.06$

$\beta_{3/4}$ (º)	J	Mach	C_P CFX	C_P JP	C_P Exp [118]	ϵ Exp-CFD	ϵ Exp-JP
53.8	1.3	0.34	1.629	-	2.1	22.4%	-
53.8	1.6	0.34	1.450	1.553	2	27.5%	22%
53.8	2	0.34	1.203	1.639	1.75	31.2%	6%
53.8	2.4	0.34	0.970	1.325	1.3	25.3%	-2%
53.8	2.8	0.34	0.571	0.663	0.8	28.7%	17%
53.8	3.2	0.34	0.046	0.051	0.05	7.8%	-2%

Table 11 – C_P - experimental wind tunnel, CFX/ANSYS, and JAVAPROP results for Mach number 0.34

For the group of simulations with $J = 3.06$, it can be observed that the results obtained in CFD were similar in value and presented similar behavior. For JAVAPROP, better results were observed close to the middle of the range, but the method had difficulties in approaching experimental results behavior. This was probably caused by its limitations

in terms of compressibility, since JAVAPROP is only able to handle two-dimensional adjustments in this aspect.

For the group of simulations with $Ma = 0.34$, JAVAPROP obtained good results in most points and followed the behavior of the curve of the experimental results. The CFD simulations had the same behavior as the experimental ones, however, they were not so close in values.

To investigate this issue, a new mesh (Figure 56) was generated, taking into account a boundary layer for the case $Ma = 0.34$. The results, as can be seen in Figure 57 and Table 12, were much closer to the experimental results.

$\beta_{3/4}$ (º)	J	Mach	C_P CFX	C_P JP	C_P Exp [118]	ϵ Exp-CFD	ϵ Exp-JP
53.8	1.3	0.34	1.870	-	2.1	11.0%	-
53.8	1.6	0.34	1.735	1.553	2	13.1%	22%
53.8	2	0.34	1.407	1.639	1.75	19.6%	6%
53.8	2.4	0.34	1.128	1.325	1.3	13.3%	-2%
53.8	2.8	0.34	0.734	0.663	0.8	8.3%	17%
53.8	3.2	0.34	0.208	0.051	0.05	-%	-2%

Table 12 – C_P - experimental wind tunnel, CFX/ANSYS, and JAVAPROP results for Mach number 0.34 - New mesh

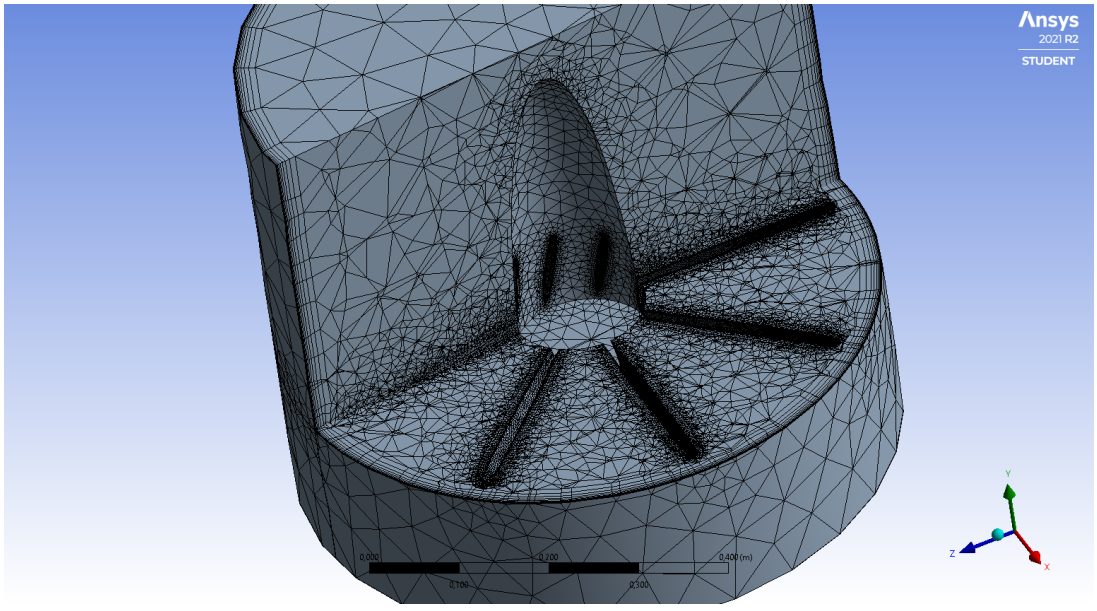

Figure 56 – New mesh generated taking into account the boundary layer

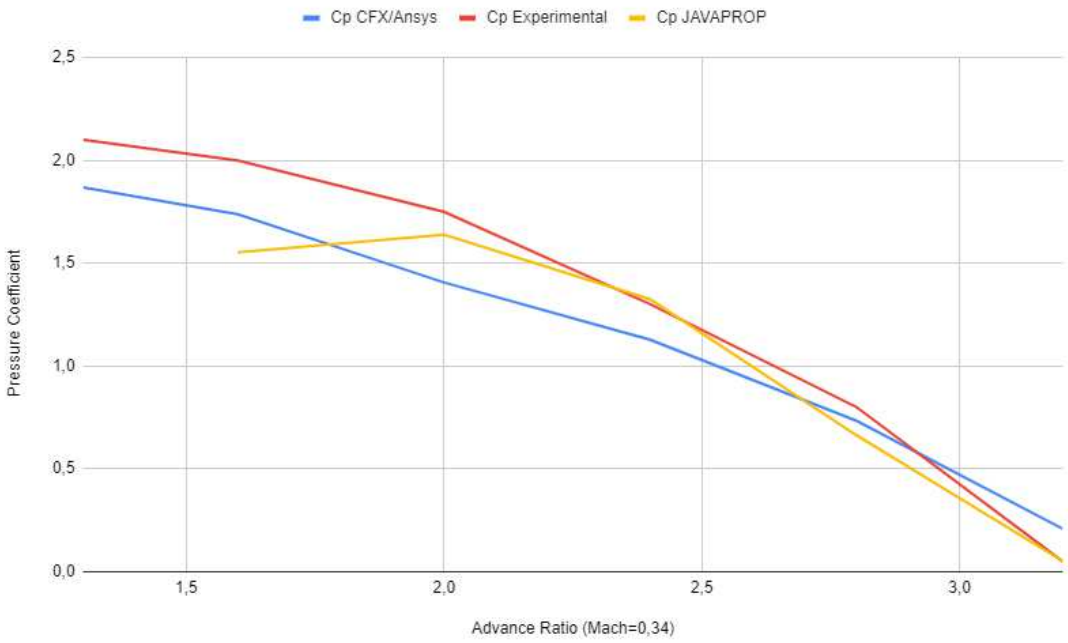

Figure 57 – C_P - experimental wind tunnel, CFX/ANSYS, and JAVAPROP results for Mach number 0.34 - New mesh

In this Section, each of the tabulated points concerns a different CFD simulation. In such simulations, meshes with between 500,000 and 512,000 nodes were used, due to the limitation of the student software license. To account for compressibility effects, the Total Energy model from CFX/ANSYS was adopted and the k-ω was adopted as the turbulence model.

6.2 Aerodynamic Propeller Parameters Optimization

In this Section, were performed on OptProp seven proposed multi-objective optimization problems (MOOPs), in which the negative value of an objective function means maximizing this function, are written as follows:

$$\begin{aligned}
&\text{MOOP1} \quad \min \quad F(-C_T, -\eta) && (6.1)\\
&\text{MOOP2} \quad \min \quad F(-C_T, C_M) && (6.2)\\
&\text{MOOP3} \quad \min \quad F(Vol, -\eta) && (6.3)\\
&\text{MOOP4} \quad \min \quad F(-C_T, -\eta, C_M) && (6.4)\\
&\text{MOOP5} \quad \min \quad F(-C_T, -\eta, Vol) && (6.5)\\
&\text{MOOP6} \quad \min \quad F(-C_T, Vol, C_M) && (6.6)\\
&\text{MOOP7} \quad \min \quad F(-C_T, Vol, C_M, -\eta) && (6.7)
\end{aligned}$$

$$\begin{aligned}
\text{subject to} \quad & \frac{CR_{max}}{\overline{CR}_{max}} - 1 \leq 0, && (6.8)\\
& -\frac{CR_{min}}{\overline{CR}_{min}} + 1 \leq 0, && (6.9)\\
& -\frac{\alpha_{min}(i)}{\overline{\alpha}_{min}(i)} + 1 \leq 0, \qquad i = [1,4] && (6.10)\\
& -\frac{\alpha_{max(i)}}{\overline{\alpha}_{max}(i)} + 1 \leq 0, \qquad i = [1,4] && (6.11)\\
& -ReC(i) + 1 \leq 0, \qquad i = [1,4] && (6.12)\\
& peak(i) - 1 \leq 0, \qquad i = [1,4] && (6.13)\\
& 1 \leq x(i) \leq 6110, \qquad i = [1,4] && (6.14)\\
& 0.2 \leq x(5) \leq 0.5, && (6.15)\\
& 2 \leq x(6) \leq 3, && (6.16)\\
& 0.1 \leq x(7) \leq 0.15, && (6.17)
\end{aligned}$$

where Vol is the propeller blade's volume and CR_{max}, and CR_{min} are the maximum and the minimum chord-to-radius ratio of a given propeller; $\overline{CR}_{max}$ and $\overline{CR}_{min}$ are the allowable values of chord and radius, set equal to 0.4 and 0.02, respectively; $\alpha_{min}(i)$ and $\alpha_{max}(i)$ are the minimum and the maximum angles for each section; and $\overline{\alpha}_{min}(i)$ and $\overline{\alpha}_{max}(i)$ are the allowable angle values. The required maximum angles are 40°, 30°, 20°, and 15°, for each section. The required minimum angles are −20°, −20°, −15°, and −15°. $ReC(i)$ is the constraint for checking if a certain section has its Reynolds number calculated compatible with the Reynolds number of a polar used by it. $peak(i)$ ensures that the

propeller has no discontinuities, eliminating geometrically bad propellers. $x(i)$, $i = [1, 4]$ are the design variables for the assignment of an airfoil in each of the four sections. These design variables are to be chosen from the airfoil database with 1,610 options (Equation 6.14). $x(5)$ is the design variable concerning the propeller diameter in meters. $x(6)$ is the number of propeller blades, and $x(7)$ is the hub diameter to propeller diameter ratio. The design variables are depicted in Figure 58.

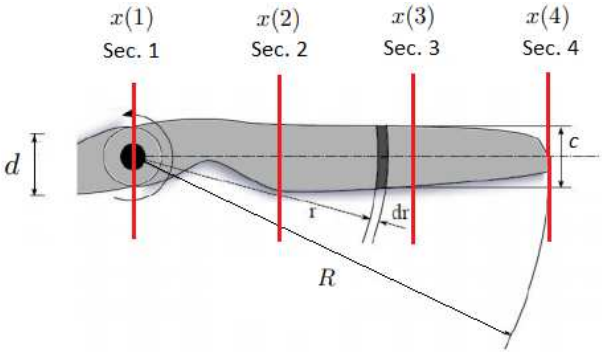

Figure 58 – Design variables for a candidate solution where d is $x(5) \times x(7)$ and R is $x(5)/2$.

Each one of the seven MOOPs defined was performed for two different engines. The first engine used was the MAX-61SX-H RING WC combustion engine [120], called OS Engine. This engine has a power of 1,195.5 W and a rotation of 16,000 rpm and was simulated at a speed of 20 m/s. The second was the electric motor E-flite Power 60 Brushless Outrunner Motor, called BL Engine [121], which has a power of 1,800 W and a rotation of 9,400 rpm. Simulations were performed at a speed of 30 m/s. The air properties were referred to 25°C, with a density equal to 1.1839 kg/m^3, kinematic viscosity equal to 1.562×10^{-4} m^2/s, and speed of sound equal to 346.3 m/s.

The population size was set equal to 100 for MOOPs 1, 2, and 3 and 200 for MOOPs 4, 5, 6, and 7. The maximum number of function evaluations is set equal to 10,000 for MOOPs 1 and 2 and 30,000 for MOOPs 3, 4, 5, 6, and 7.

6.2.1 Pareto fronts

Figures 59 to 73 present the Pareto fronts for MOOP1 to MOOP6 concerning the OS Engine, while Figures 79 to 93 present the Pareto fronts for the BL Engine. To view Pareto fronts with four or more objective functions, parallel coordinates that display multidimensional data in a two-dimensional graph are adopted, as used in Li *et al.* [122]. The original data are translated into a vertical axis in the graph, and a poly-line with vertices on the axes represents the vector with the objective functions [122]. In this way, Figures 74 to 78 and 94 to 98 depict the Pareto fronts for MOOP7 concerning the OS Engine and the BL Engine, respectively.

Considering the OS Engine and MOOP1 (Figure 59), one notices a very similar and uniform distribution of the non-dominated solutions obtained by NSGAIIARSBX, NSGAII, AGEMOEA, and ARMOEA. These algorithms distributed the solutions on the Pareto Front with greater diversity. Also, NSGAIIARSBX and MSOPSII achieved some solutions at the bottom of the Pareto fronts of this problem. The minimum and maximum values for C_T are 0.03 and 0.23, respectively, and for η, 0.52 and 0.69. For MOOP2 (Figure 60), two well-defined Pareto fronts were obtained, in which the NSGAII presents, almost in its entirety, the solutions of one of these fronts, which also has solutions obtained by the other algorithms in the part where the C_T presents its smallest values. On the other Pareto front, the NSGAIIARSBX shows a more continuous distribution of non-dominated solutions. On this front, solutions are also obtained by the other algorithms. In the "superior" front, the minimum value of C_T is close to 0.025 and the maximum to 0.17, while in the "lower" front, C_T has a minimum value close to 0.04 and a maximum value near 0.24.

Observing the Pareto fronts of MOOP3 (Figure 61), it is noted that the MSOPSII algorithm obtained a distribution of non-dominant solutions with greater diversity, achieving the best performance. The other algorithms concentrated their solutions on an extreme of the Pareto fronts. The extreme solutions are approximately 0.1×10^{-3} m^3 and 1.8×10^{-3} m^3 for volume and 0.54 and 0.7 for the efficiency η.

Figure 62 shows the Pareto front for MOOP4 for the OS Engine. Figures 63, 64, and 65 present the projections in two axes of this Pareto front. It is possible to observe a distribution of non-dominated solutions in three regions. At one end of the front, at the bottom, the non-dominated solutions are presented by the AGEMOEA algorithm while at the top by the ARMOEA algorithms and MSOPSII. The other algorithms found solutions in the middle of the Pareto front. The minimum value of η is approximately 0.3 and 0.67 for the maximum, minimum of 0.004 and maximum of 0.03 for C_M, and minimum of 0.03 and maximum of 0.023 for C_T.

Figure 66 shows the Pareto fronts obtained for MOOP5 (OS Engine). The projections of the fronts are shown in Figures 67, 68, and 69. There is a good diversity of non-dominated solutions obtained by the algorithms ARMOEA, NSGAII, and NSGAIIARSBX in the lower region of the fronts. The MSOPSII algorithm concentrated the solutions on a front and with less diversity. The minimum value of C_T is approximately 0.03 and the maximum 0.23, a minimum of 0.52, and maximum of 0.68 for η, and minimum of 0.1×10^{-3} m^3 and maximum of 3.2×10^{-3} m^3 for volume.

Figure 70 shows the Pareto fronts obtained for MOOP6 (OS Engine). The projections of the fronts are shown in Figures 71, 72, and 73. A varied distribution of non-dominated solutions was found by the algorithms. The algorithms that presented the lowest diversity were MSOPSII and AGEMOEA. In the projection showing the objective

functions C_T and C_M, there are two distinct sets of non-dominated solutions, where one of them with less diversity presents almost all the solutions obtained by MSOPSII. The maximum value obtained for C_T is close to 0.24 and a minimum of 0.03. The volume varies between 0.02×10^{-3} m^3 and 4×10^{-3} m^3 and C_M between 0.05 and 0.028. Figures 74 to 78 show the Pareto fronts for MOOP7 OS analysis, with the non-dominated solutions normalized with values between 0 and 1 for each of the algorithms independently. Note that there is a great diversity of non-dominated solutions, except those obtained by MSOPSII concerning the objective functions, 2, 3, and 4, as shown in Figure 76.

Considering the BL Engine and MOOP1 (Figure 79), a very similar and uniform distribution of the non-dominated solutions obtained by NSGAIIARSBX, NSGAII, AGE-MOEA, and ARMOEA is observed, as in the case in which the OS Engine was adopted. These algorithms distributed the solutions on the Pareto front with greater diversity. It is also noted that NSGAIIARSBX and NSGAII found a set of solutions at the bottom of the Pareto fronts of this problem. The minimum value of C_T is close to 0.05 whereas the maximum is near 0.42, and 0.6 and 0.82 are approximately the minimum and the maximum values for η.

For MOOP2 (Figure 80), again, two well-defined Pareto fronts were obtained, in which MSOPSII reached the non-dominated solutions almost independently in each one of these fronts, but with low diversity. The minimum and maximum values for C_T are 0.03 and 0.4 and 0.004 and 0.055 for C_M. From the Pareto fronts of MOOP3 (Figure 81), it is noted that the MSOPSII algorithm obtained a distribution of non-dominant solutions with greater diversity, but in some regions, there were no non-dominated solutions. The other algorithms concentrated their solutions on an extreme of the Pareto fronts. The extreme solutions are approximately 0.1×10^{-3} m^3 and 1.5×10^{-3} m^3 for volume and 0.73 and 0.84 for the efficiency η, respectively.

Figure 82 shows the Pareto front for MOOP4 for the BL Engine. Figures 83, 84, and 85 present the projections in two axes of this Pareto front. It is possible to observe a similar distribution of non-dominated solutions in the Pareto front, except for MSOPSII, and some solutions of NSGAII, that concentrated their solutions in two separate regions with low diversity, as shown in Figure 63. The NSGAIIARSBX and NSGAII were able to find non-dominated solutions in an extreme of the Pareto front, presenting high values of C_T and C_M. 0.03 and 0.45 are the minimum and the maximum values for C_T; 0.03 and 0.064 for C_M, and 0.57 and 0.83 for η, respectively.

Figure 86 shows the Pareto fronts obtained for MOOP5 (BL Engine). The projections of the fronts are shown in Figures 87, 88, and 89. A good diversity of non-dominated solutions obtained by the algorithms is observed, except for the MSOPSII algorithm, which concentrated the solutions on a front and with less diversity. The minimum value of C_T is approximately 0.03 and the maximum 0.52, a minimum of 0.53 and maximum of 0.83 for

η, and a minimum of 0.1×10^{-3} m^3 and a maximum of 4×10^{-3} m^3 for volume.

Figure 90 shows the Pareto fronts obtained for MOOP6 (BL Engine). The projections of the fronts are shown in Figures 91, 92, and 93. Figure 90 shows a convergence of solutions at the same points near the origin of the axis. Throughout the Pareto front, the non-dominated solutions spread in several directions. Figure 91 shows two different Pareto fronts, in which one of them the great majority are from MSOPSII and NSGAIIARSBX algorithms. The minimum and maximum values for C_T are 0.05 and 0.51, 0.05 and 0.072 for C_T, and 0.1×10^{-3} m^3 and 5.8×10^{-3} m^3 for volume, respectively. Figures 94 to 98 show the Pareto fronts for MOOP7 experiments, with the non-dominated solutions normalized with values between 0 and 1 for each of the algorithms independently. Note that there is a great diversity of non-dominated solutions.

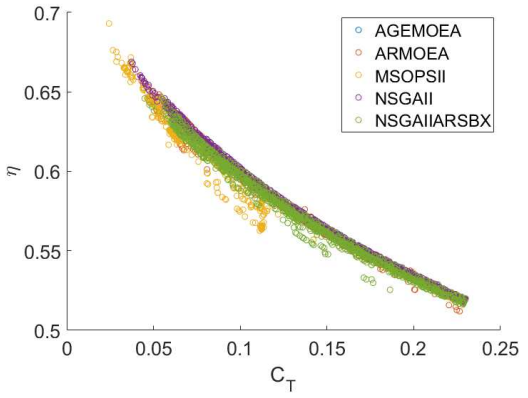

Figure 59 – MOOP1 for OS Engine.

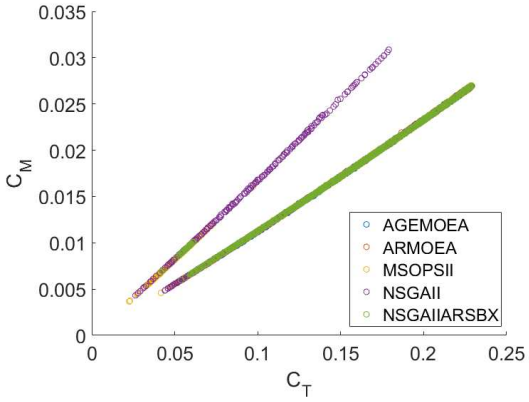

Figure 60 – MOOP2 for OS Engine.

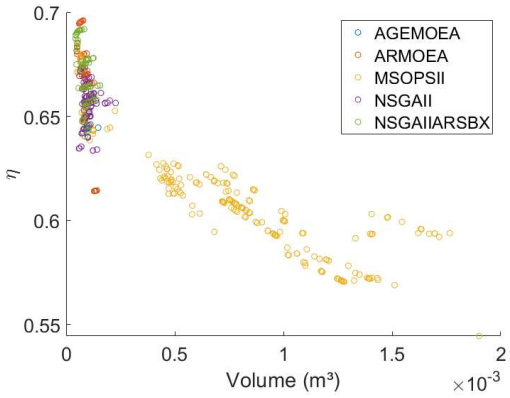

Figure 61 – MOOP3 for OS Engine.

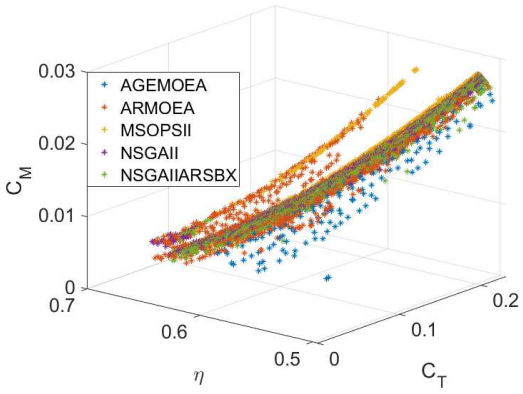

Figure 62 – MOOP4 for OS Engine.

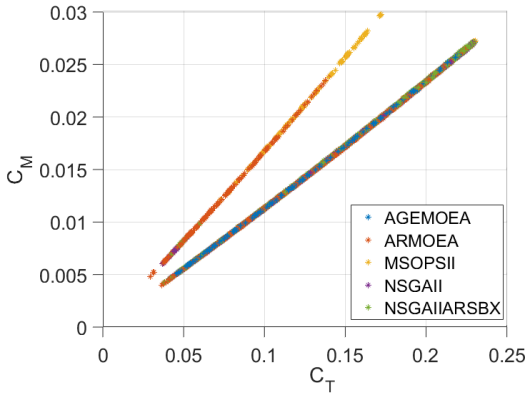

Figure 63 – MOOP4 for OS Engine - $C_T \times C_M$

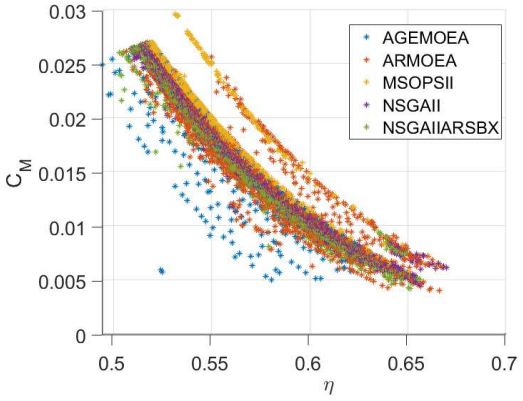

Figure 64 – MOOP4 for OS Engine - $\eta \times C_M$

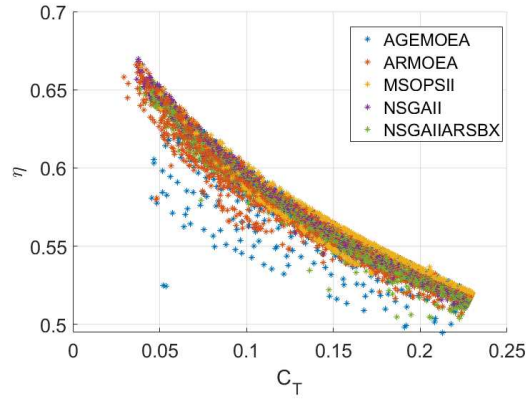

Figure 65 – MOOP4 for OS Engine - $C_T \times \eta$

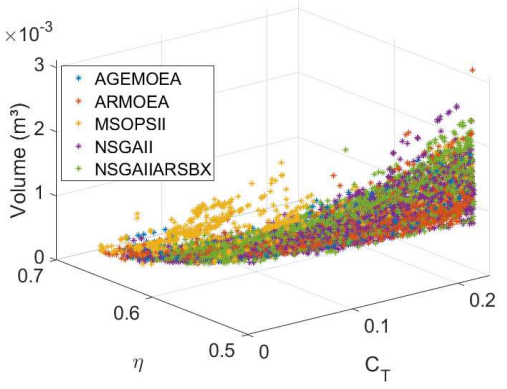

Figure 66 – MOOP5 for OS Engine

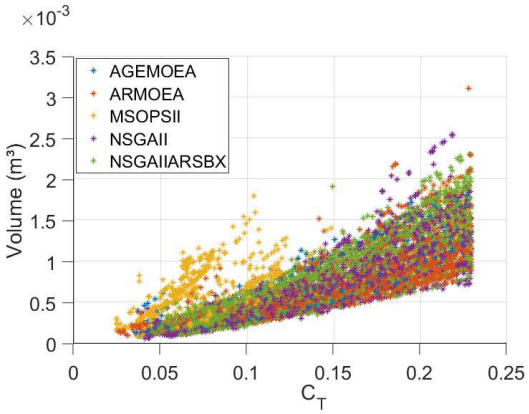

Figure 67 – MOOP5 for OS Engine - $C_T \times Vol(m^3)$

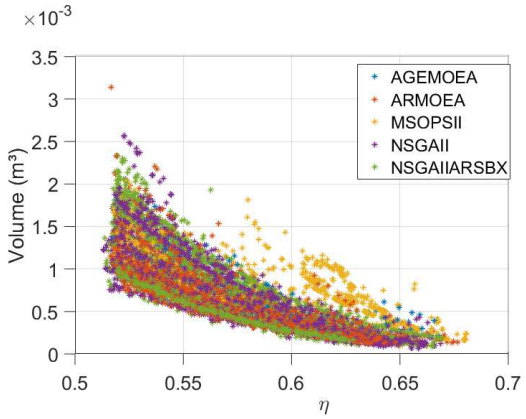

Figure 68 – MOOP5 for OS Engine - $\eta \times Vol(m^3)$

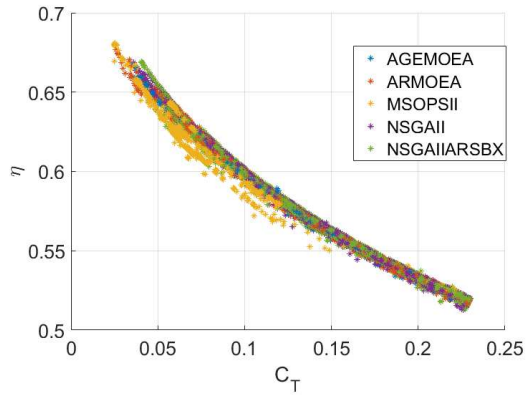

Figure 69 – MOOP5 for OS Engine - $C_T \times \eta$

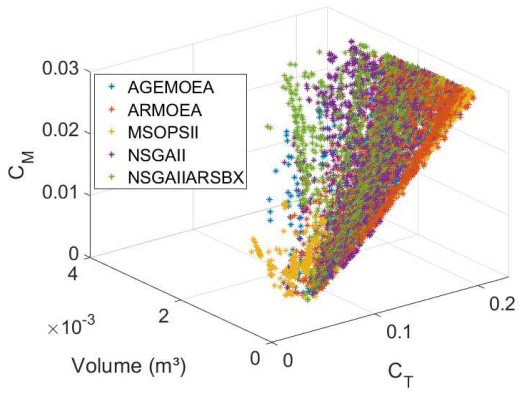

Figure 70 – MOOP6 for OS Engine

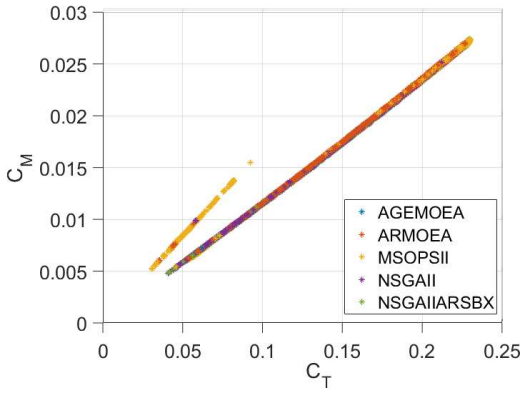

Figure 71 – MOOP6 for OS Engine - $C_T \times C_M$

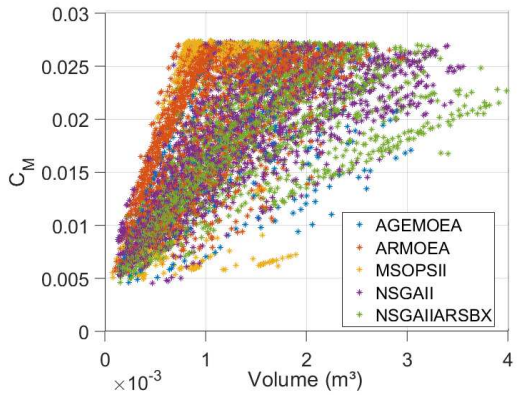

Figure 72 – MOOP6 for OS Engine - $Vol(m^3) \times C_M$

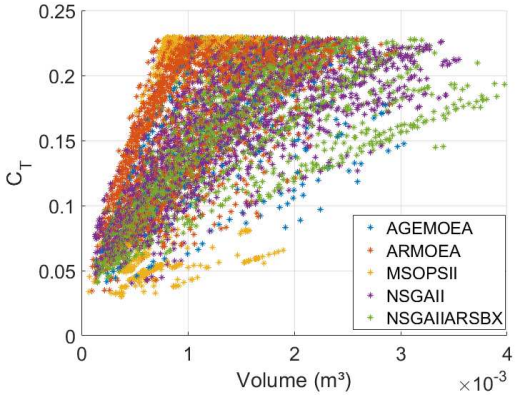

Figure 73 – MOOP6 for OS Engine - $Vol(m^3) \times C_T$

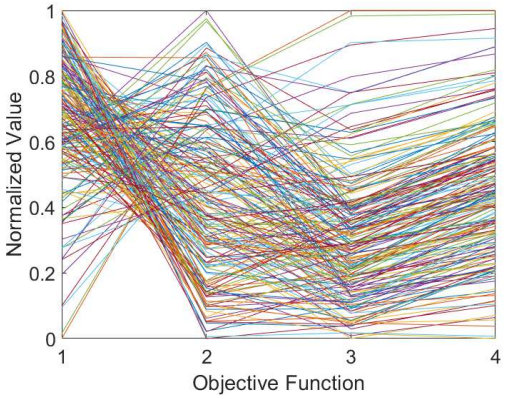

Figure 74 – MOOP7 - AGEMOEA for OS Engine

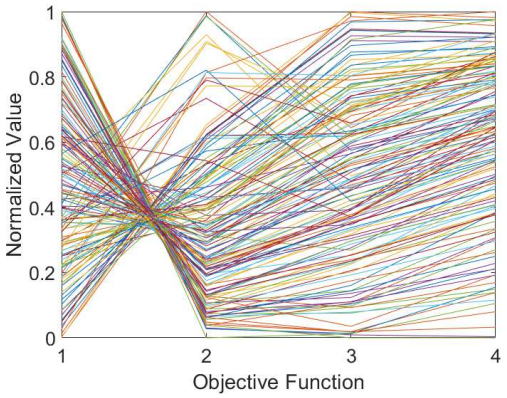

Figure 75 – MOOP7 - ARMOEA for OS Engine

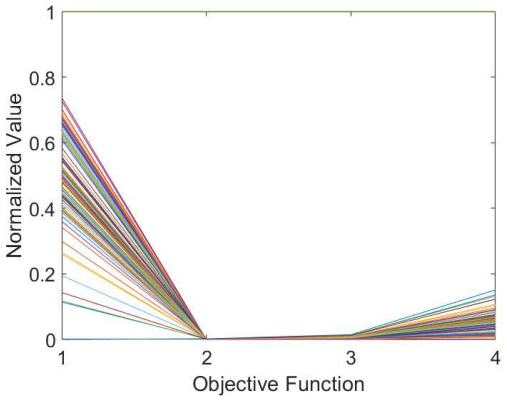

Figure 76 – MOOP7 - MSOPSII for OS Engine

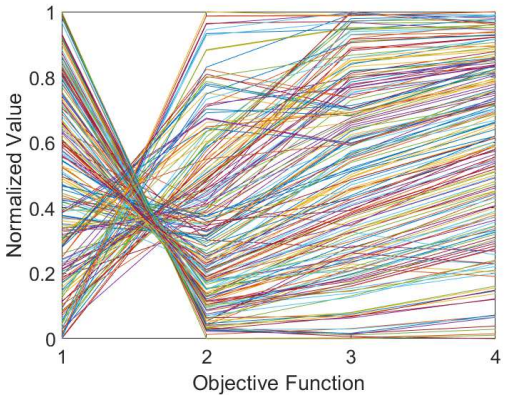

Figure 77 – MOOP7 - NSGAII for OS Engine

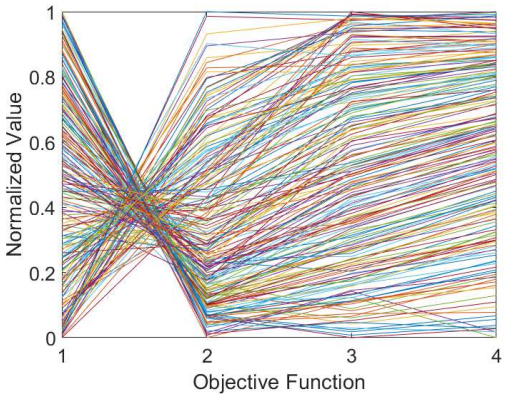

Figure 78 – MOOP7 - NSGAIIARSBX for OS Engine

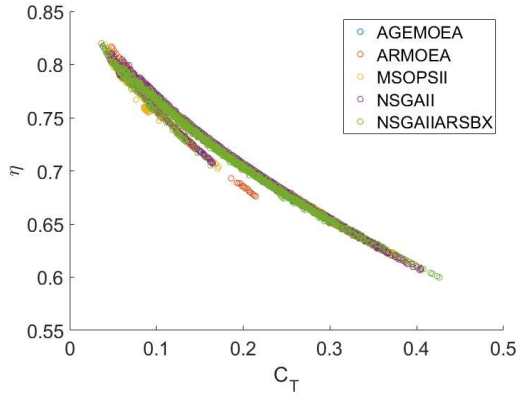

Figure 79 – MOOP1 for BL Engine

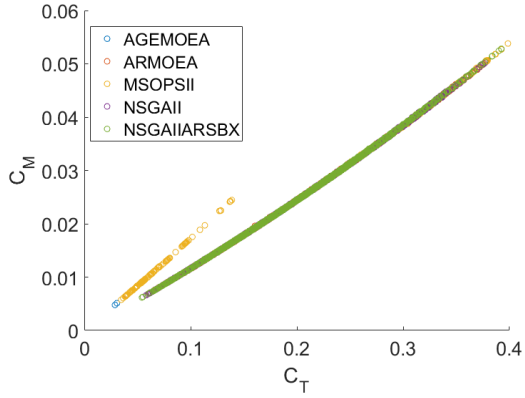

Figure 80 – MOOP2 for BL Engine

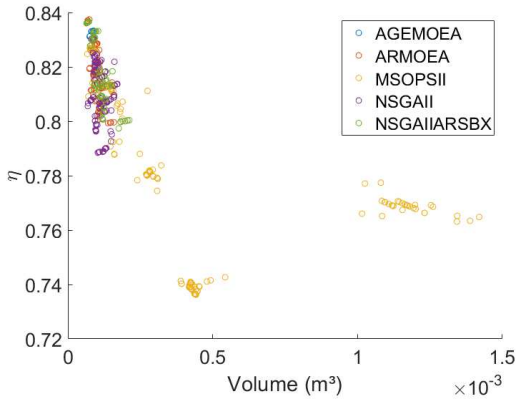

Figure 81 – MOOP3 for BL Engine

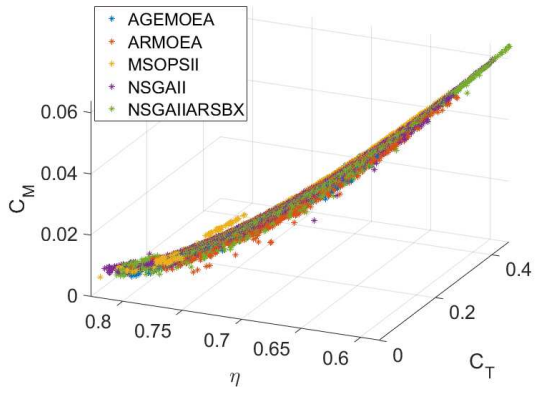

Figure 82 – MOOP4 for BL Engine

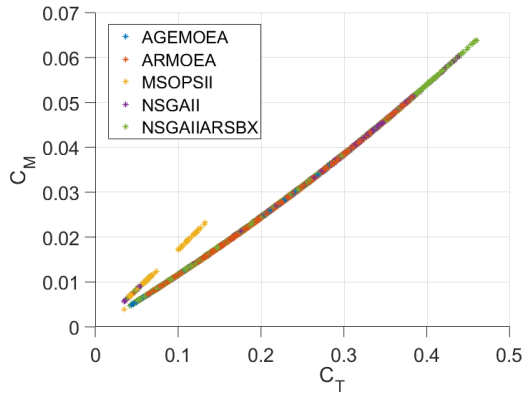

Figure 83 – MOOP4 for BL Engine - $C_T \times C_M$

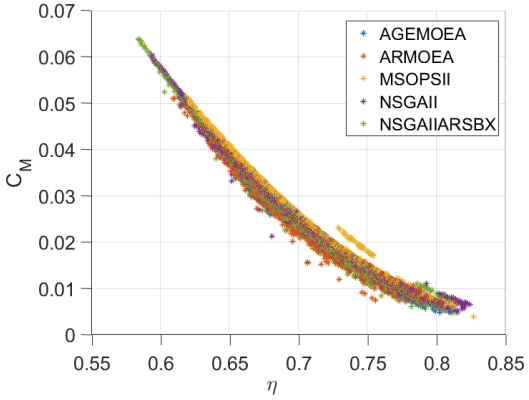

Figure 84 – MOOP4 for BL Engine - $\eta \times C_M$

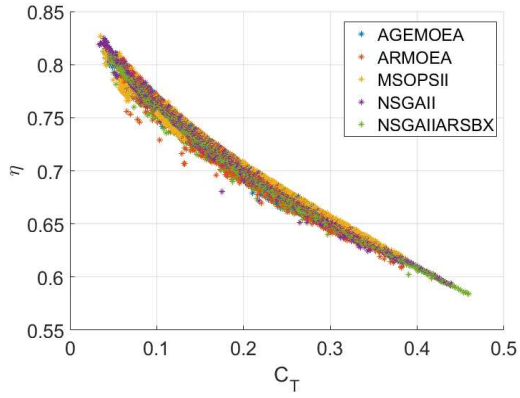

Figure 85 – MOOP4 for BL Engine - $C_T \times \eta$

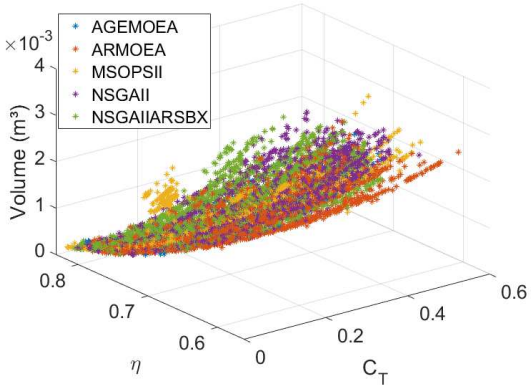

Figure 86 – MOOP5 for BL Engine

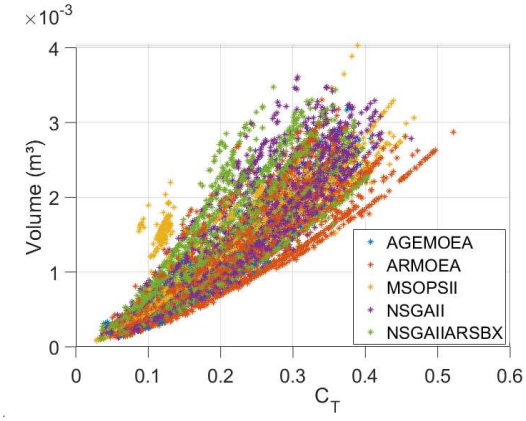

Figure 87 – MOOP5 for BL Engine - $C_T \times Vol(m^3)$

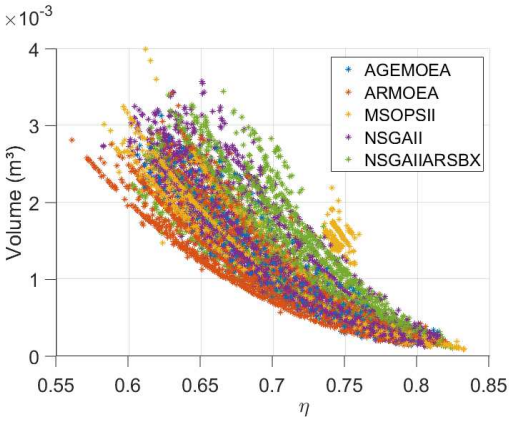

Figure 88 – MOOP5 for BL Engine - $\eta \times Vol(m^3)$

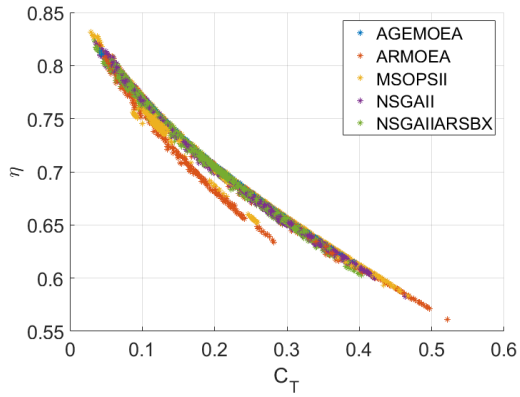

Figure 89 – MOOP5 for BL Engine - $C_T \times \eta$

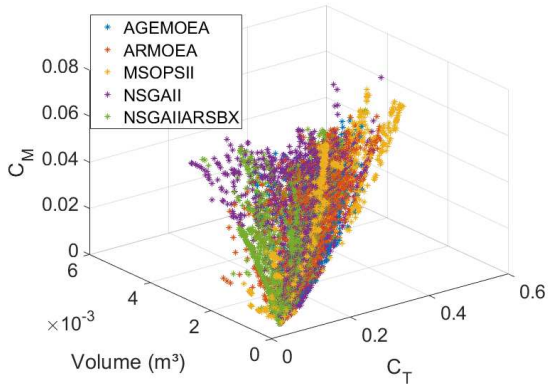

Figure 90 – MOOP6 for BL Engine

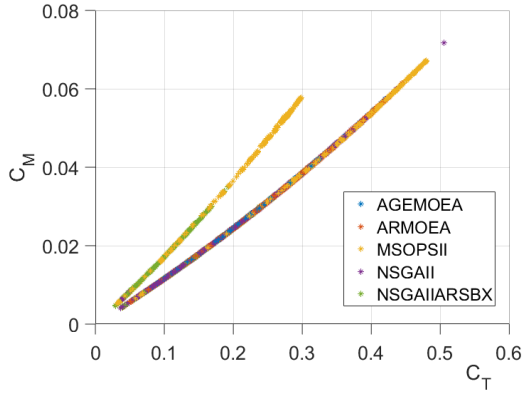

Figure 91 – MOOP6 for BL Engine - $C_T \times C_M$

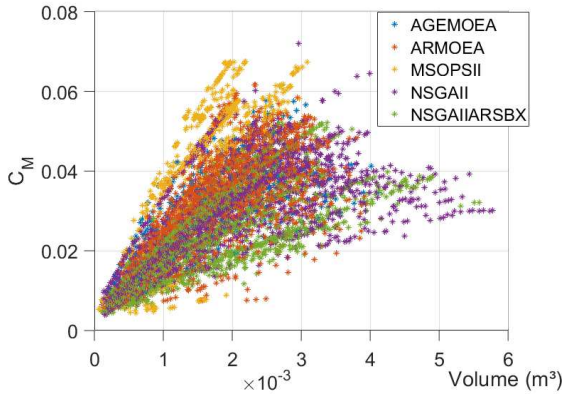

Figure 92 – MOOP6 for BL Engine - $Vol(m^3) \times C_M$

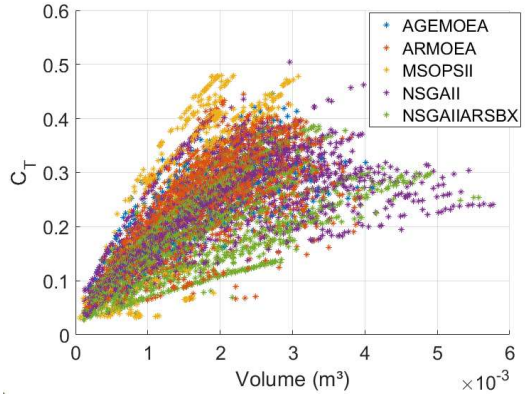

Figure 93 – MOOP6 for BL Engine - $Vol(m^3) \times C_T$

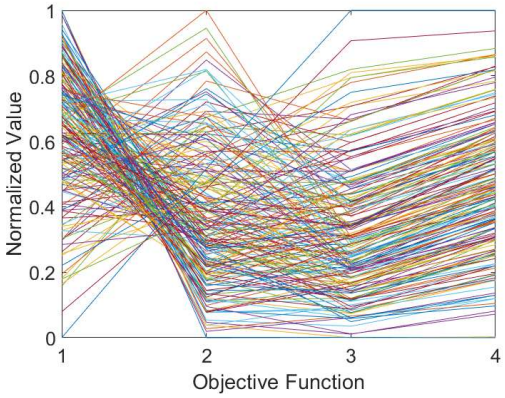

Figure 94 – MOOP7 - AGEMOEA for BL Engine

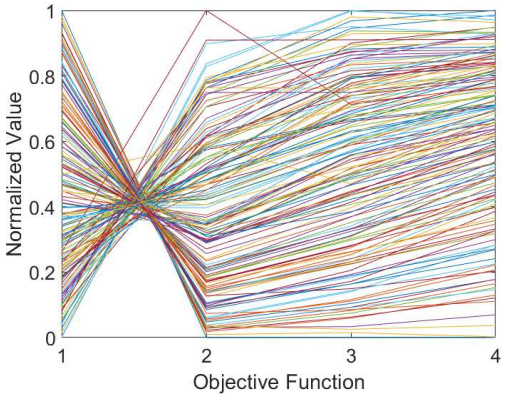

Figure 95 – MOOP7 - ARMOEA for BL Engine

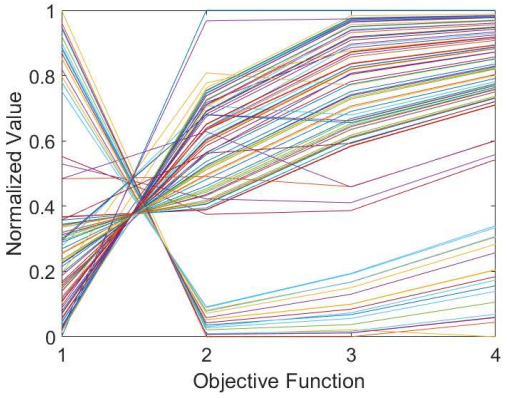

Figure 96 – MOOP7 - MSOPSII for BL Engine

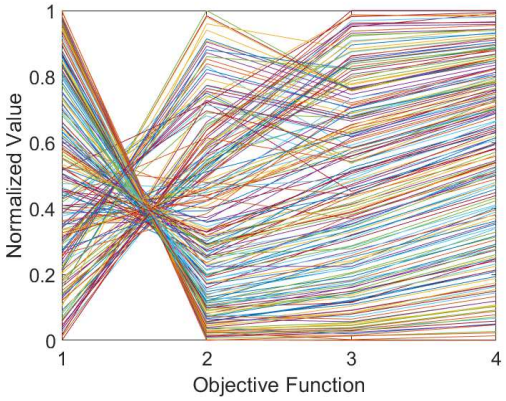

Figure 97 – MOOP7 - NSGAII for BL Engine

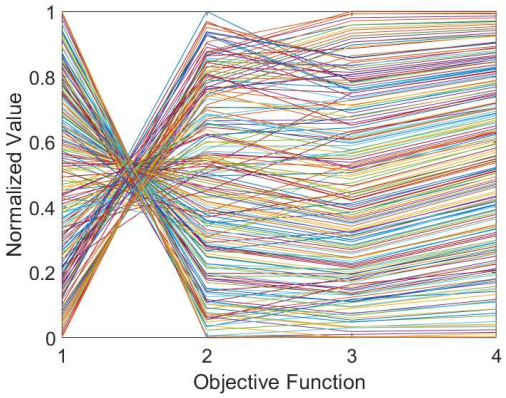

Figure 98 – MOOP7 - NSGAIIARSBX for BL Engine

6.2.2 Performance indicators

Four metrics are adopted to evaluate the performance of the multi-objective algorithms, such as Inverted Generational Distance (IGD) [123], Hypervolume (HV) [124], Feasible Rate (FR) (meaning the ratio of runs where the algorithm finds a feasible solution), and Spacing (S) [125]. The average values and the standard deviation (in parentheses) of these performance indicators are presented in Tables 20 to 27 for both engines, provided in Appendix B.

Also, Tables 20 to 27 provide a statistical analysis using the non-parametric Wilcoxon rank sum test (p-value < 0.05). The symbols $+, -$ and $\approx$ indicate the best, worst, and similar ranks, respectively, obtained by an algorithm in the comparison, in which the best performances are highlighted in yellow.

From the performance indicators concerning the OS Engine, one can observe the following conclusions: For IGD, AGEMOEA and MSOPII achieved the best performance.

For HV, AGEMOEA outperformed all the algorithms. All the algorithms presented the same performance considering the feasible rate, and finally, NSGAII presented the best performance in the Spacing indicator.

From the performance indicators concerning the BL Engine, one can observe the following conclusions: For IGD, AGEMOEA, MSOPII, and NSGAIIARSBX achieved the best performance. For HV, AGEMOEA, ARMOEA, and NSGAIIARSBX presented a similar performance. All the algorithms showed the same performance considering the feasible rate, and finally, AGEMOEA presented the best performance in the Spacing indicator, followed by ARMOEA and NSGAII.

Overall, the AGEMOEA can be considered the multi-objective algorithm that presented the best performance.

6.2.3 Extracted solutions from the Pareto fronts

Figures 99, 100, 101, and 102 show the Pareto fronts of MOOP5 for both engines. These Pareto fronts contain the whole set of non-dominated solutions obtained by the AGEMOEA, NSGA II, and NSGAIIARSBX algorithms, which performed best in the comparisons and similar Pareto fronts concerning MOOP5. These fronts are used to illustrate how multi-criteria decision-making (MCDM) is able to extract solutions according to his preferences. MCDM is based on w_i weights assigned by the decision-maker for each objective function according to his preferences. Each weight w_i must be in the range between 0 and 1, and their sum must be equal to 1. This strategy is fully detailed and used in the references [126, 127, 128, 129]. Two cases are suggested, such as: Case I – $w_1 = 0.7$, $w_2 = 0.1$, and $w_3 = 0.2$ and Case II – $w_1 = 0.2$, $w_2 = 0.7$, and $w_3 = 0.1$. A point in red marks the extracted solutions. Certainly, other combinations of weights w_i can be made, and other solutions can be extracted according to the different preferences of the decision-maker.

Table 13 provides the final design variables for each of the extracted solutions and Table 14 presents the geometric aspects of the section, in which r/R is the dimensionless section, c/R is the dimensionless chord, and β is the cross-sectional pitch angle. Figures 103, 104, 105, and 106 show their respective shapes.

The performance curves of the optimized propellers for Case I and Case II are depicted in Figures 107 and 108, respectively. In each curve, a comparison between OS and BL engines is provided. Information about these curves are provided in Tables 15 to 18. It is noted that using the same criteria for the choices, the BL electric motor provided propellers at a higher advance ratio with slightly higher performances.

The results presented in this Chapter are published in [130].

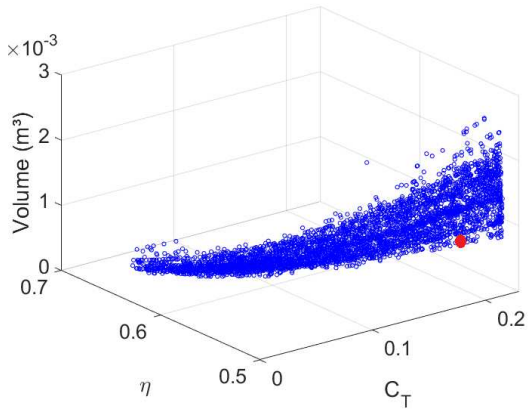

Figure 99 – Extracted Solution 1 - MOOP5 - OS Engine

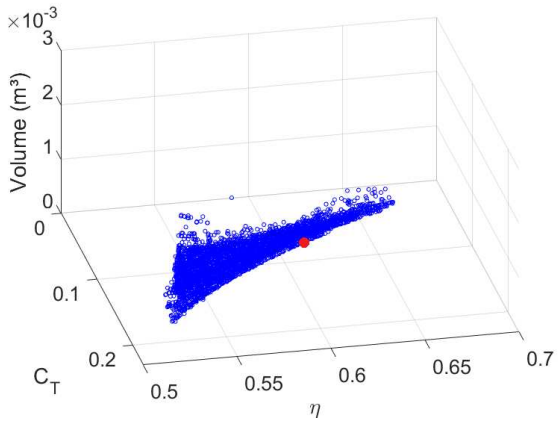

Figure 100 – Extracted Solution 2 - MOOP5 - OS Engine

	Case	$x(1)$	$x(2)$	$x(3)$	$x(4)$	$x(5)$	$x(6)$	$x(7)$
OS Engine	I	397 GOE 596	1140 BOEING 106	4888 EPPLER 435	1836 FX 83-W-108	0.21	3	0.071
	II	2401 MH 95	2052 GOE 304	1896 GOE 63	744 E193 (10.22%)	0.26	3	0.081
Brushless Engine	I	5855 GOE 399	3340 St. CYR 171	4788 NACA M8	376 BE50 smooth	0.26	3	0.084
	II	529 GOE 795	3372 CLARK X	160 AH 79-100 B	3736 HQ 3.5 10	0.33	3	0.073

Table 13 – Design variables of the extracted solutions using the MCDM ($d = x(5) \times x(7)$). Case I - $w_1 = 0.7$, $w_2 = 0.1$, and $w_3 = 0.2$; Case II $w_1 = 0.2$, $w_2 = 0.7$, and $w_3 = 0.1$.

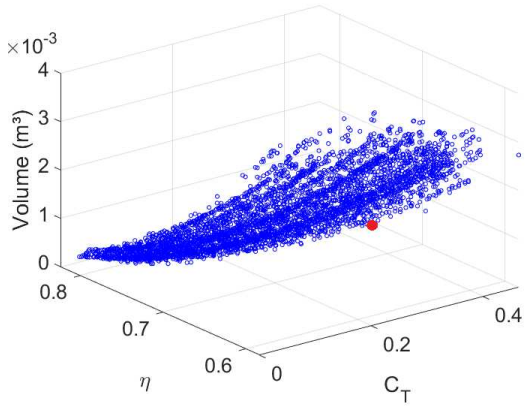

Figure 101 – Extracted Solution 1 - MOOP5 - BL engine

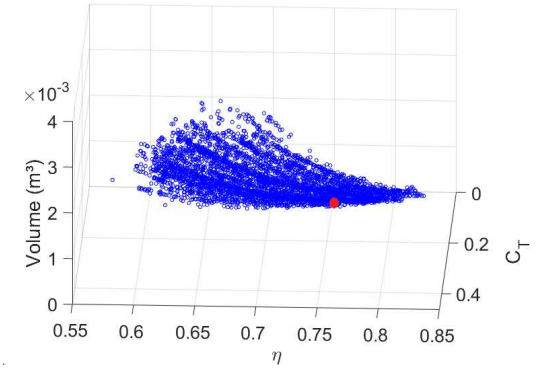

Figure 102 – Extracted Solution 1 - MOOP5 - BL engine

	OS - Case I		OS - Case II		Brushless - Case I		Brushless - Case II	
r/R	c/R	$\beta(°)$	c/R	$\beta(°)$	c/R	$\beta(°)$	c/R	$\beta(°)$
0.000	-	-	-	-	-	-	-	-
0.042	-	-	-	-	-	-	-	-
0.083	0.058	88.2	0.041	83.3	-	-	0.038	78.1
0.125	0.130	82.9	0.089	76.6	0.099	82.5	0.075	68.7
0.167	0.219	78.2	0.141	70.6	0.147	75.4	0.108	60.5
0.208	0.313	73.9	0.190	65.1	0.189	68.8	0.131	53.4
0.250	0.403	69.9	0.229	60.1	0.227	62.9	0.144	47.1
0.292	0.487	66.1	0.257	55.7	0.261	57.5	0.148	41.7
0.333	0.557	62.4	0.276	51.6	0.287	52.4	0.147	37.0
0.375	0.613	59.6	0.286	48.1	0.297	49.5	0.145	34.1
0.417	0.653	56.9	0.290	45.0	0.298	47.0	0.141	31.6
0.458	0.678	54.4	0.287	42.2	0.294	44.7	0.136	29.5
0.500	0.690	52.0	0.281	39.7	0.285	42.7	0.130	27.7
0.542	0.691	49.8	0.271	37.4	0.273	41.0	0.124	26.1
0.583	0.681	47.8	0.258	35.3	0.259	39.5	0.118	24.8
0.625	0.662	45.9	0.244	33.4	0.243	38.1	0.111	23.6
0.667	0.636	44.1	0.229	31.7	0.226	37.0	0.104	22.6
0.708	0.632	42.3	0.225	30.3	0.222	35.0	0.102	21.5
0.750	0.620	40.6	0.220	29.1	0.216	33.2	0.099	20.5
0.792	0.598	39.1	0.212	28.0	0.208	31.5	0.095	19.7
0.833	0.564	37.6	0.201	26.9	0.196	29.8	0.089	18.9
0.875	0.516	36.2	0.185	26.0	0.180	28.3	0.082	18.2
0.917	0.444	34.9	0.161	25.1	0.156	26.9	0.072	17.5
0.958	0.332	33.7	0.122	24.4	0.117	25.5	0.054	16.9
1.000	0.197	32.5	0.075	23.6	0.071	24.2	0.033	16.4

Table 14 – Geometric aspects of the section, r/R is the dimensionless section, c/R is the dimensionless chord, and β the cross-sectional pitch angle.

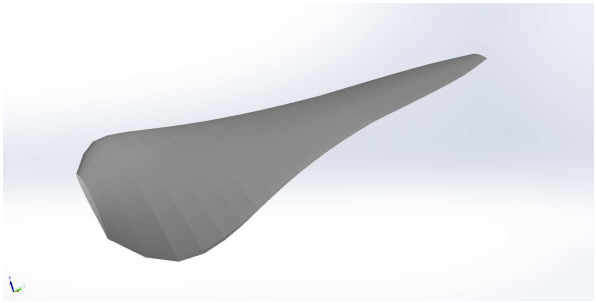

Figure 103 – Optimized Propeller for OS Engine & Case I

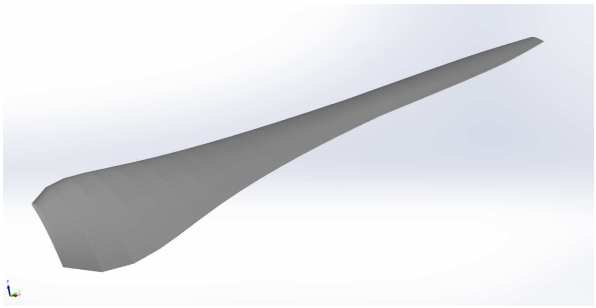

Figure 104 – Optimized Propeller for OS Engine & Case II

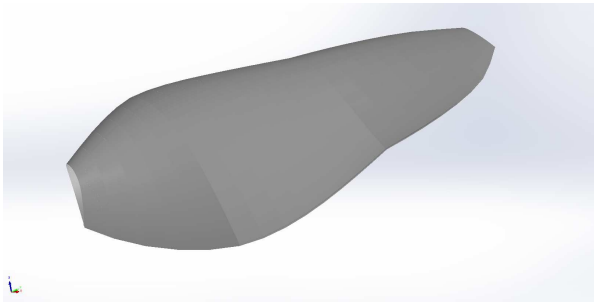

Figure 105 – Optimized Propeller for Brushless Engine & Case I

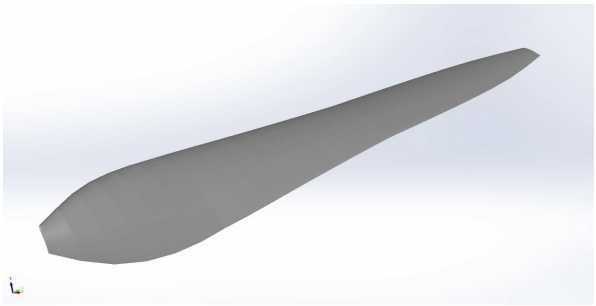

Figure 106 – Optimized Propeller for Brushless Engine & Case II

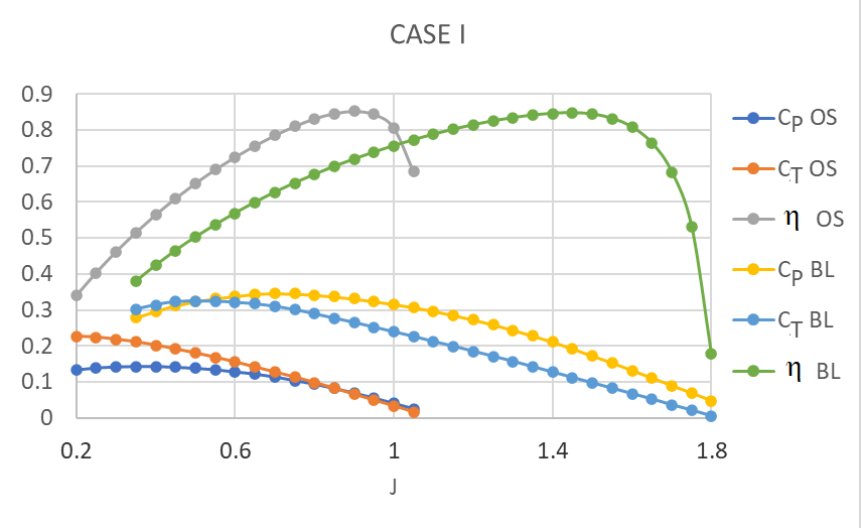

Figure 107 – Performance curves for Case I

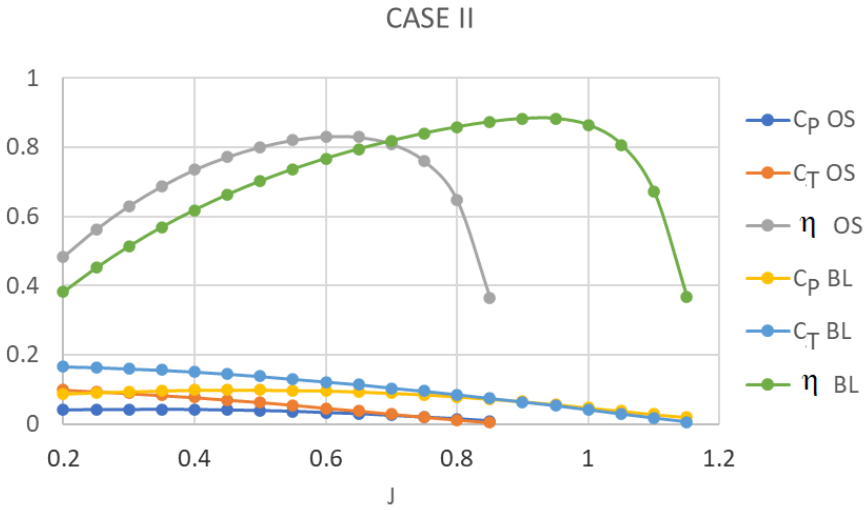

Figure 108 – Performance curves for Case II

J	C_P	C_T	η (%)	Stalled (%)	$V(m/s)$	Power (W)	Thrust (N)
0.2	0.133	0.226	33.94	3	10.99	1110.42	34.30
0.25	0.139	0.224	40.31	1	13.73	1159.64	34.04
0.3	0.142	0.218	46.14	0	16.48	1181.70	33.08
0.35	0.143	0.211	51.49	0	19.23	1193.90	31.98
0.4	0.143	0.202	56.44	0	21.97	1190.84	30.59
0.45	0.141	0.191	60.96	0	24.72	1176.93	29.02
0.5	0.138	0.180	65.15	0	27.47	1150.28	27.28
0.55	0.134	0.168	68.98	0	30.21	1115.02	25.46
0.6	0.128	0.155	72.48	0	32.96	1068.64	23.50
0.65	0.122	0.141	75.64	0	35.71	1012.55	21.45
0.7	0.114	0.127	78.50	0	38.45	946.12	19.31
0.75	0.104	0.113	81.03	0	41.20	869.10	17.09
0.8	0.094	0.098	83.16	0	43.95	781.81	14.79
0.85	0.082	0.082	84.61	0	46.69	683.69	12.39
0.9	0.069	0.065	85.22	0	49.44	576.05	9.93
0.95	0.055	0.049	84.40	0	52.19	460.00	7.44
1	0.040	0.033	80.68	0	54.93	336.47	4.94
1.05	0.025	0.016	68.50	0	57.68	205.01	2.43

Table 15 – Performance characteristics for optimized propeller for OS engine & Case I

J	C_P	C_T	η (%)	Stalled (%)	$V(m/s)$	Power (W)	Thrust (N)
0.2	0.041	0.099	48.22	1	14.03	1161.10	39.92
0.25	0.042	0.094	56.16	0	17.53	1179.68	37.79
0.3	0.042	0.089	62.96	0	21.04	1198.77	35.87
0.35	0.043	0.083	68.70	0	24.55	1200.88	33.61
0.4	0.042	0.077	73.49	0	28.05	1188.62	31.14
0.45	0.041	0.070	77.19	0	31.56	1159.36	28.36
0.5	0.039	0.063	80.04	0	35.07	1108.40	25.30
0.55	0.037	0.055	82.08	0	38.57	1033.88	22.00
0.6	0.033	0.046	83.10	0	42.08	943.70	18.64
0.65	0.030	0.038	82.89	0	45.59	838.48	15.25
0.7	0.025	0.029	80.93	0	49.09	714.20	11.77
0.75	0.020	0.020	75.95	0	52.60	569.38	8.22
0.8	0.015	0.012	64.66	0	56.11	419.24	4.83
0.85	0.009	0.004	36.46	0	59.61	267.61	1.64

Table 16 – Performance characteristics for optimized propeller for OS engine & Case II

J	C_P	C_T	η (%)	Stalled (%)	$V(m/s)$	Power (W)	Thrust (N)
0.35	0.278	0.302	37.93	69	14.15	1448.03	38.82
0.4	0.296	0.314	42.38	62	16.17	1540.95	40.39
0.45	0.312	0.323	46.51	62	18.19	1624.82	41.55
0.5	0.323	0.324	50.21	53	20.21	1681.22	41.77
0.55	0.332	0.324	53.67	44	22.23	1725.45	41.65
0.6	0.338	0.321	56.89	25	24.25	1761.28	41.31
0.65	0.344	0.317	59.90	20	26.27	1789.17	40.79
0.7	0.346	0.310	62.69	5	28.29	1803.01	39.95
0.75	0.345	0.301	65.26	0	30.32	1797.83	38.70
0.8	0.342	0.289	67.63	0	32.34	1779.81	37.22
0.85	0.337	0.277	69.85	0	34.36	1755.29	35.68
0.9	0.331	0.265	71.90	0	36.38	1724.16	34.08
0.95	0.324	0.252	73.82	0	38.40	1686.99	32.43
1	0.316	0.239	75.60	0	40.42	1644.56	30.76
1.05	0.307	0.226	77.25	0	42.44	1596.91	29.07
1.1	0.297	0.212	78.77	0	44.46	1543.54	27.35
1.15	0.285	0.199	80.16	0	46.48	1484.32	25.60
1.2	0.273	0.185	81.41	0	48.50	1419.17	23.82
1.25	0.259	0.171	82.49	0	50.53	1348.35	22.01
1.3	0.244	0.157	83.38	0	52.55	1270.31	20.16
1.35	0.228	0.142	84.11	0	54.57	1185.67	18.28
1.4	0.211	0.127	84.58	0	56.59	1096.21	16.39
1.45	0.192	0.112	84.73	0	58.61	999.13	14.44
1.5	0.172	0.097	84.37	0	60.63	896.94	12.48
1.55	0.153	0.082	83.17	0	62.65	793.90	10.54
1.6	0.132	0.067	80.76	0	64.67	687.97	8.59
1.65	0.111	0.052	76.35	0	66.69	579.27	6.63
1.7	0.090	0.036	68.36	0	68.71	468.92	4.67
1.75	0.069	0.021	53.20	0	70.74	357.45	2.69
1.8	0.048	0.005	17.70	0	72.76	248.73	0.61

Table 17 – Performance characteristics for the optimized propeller for BL Engine & Case I

J	C_P	C_T	η (%)	Stalled (%)	$V(m/s)$	Power (W)	Thrust (N)
0.2	0.087	0.166	38.16	6	10.43	1621.93	59.32
0.25	0.091	0.164	45.13	4	13.04	1694.77	58.64
0.3	0.093	0.160	51.34	4	15.65	1740.37	57.09
0.35	0.096	0.156	56.91	3	18.26	1789.43	55.77
0.4	0.098	0.151	61.85	1	20.87	1822.24	54.01
0.45	0.098	0.145	66.30	0	23.48	1833.98	51.80
0.5	0.098	0.138	70.20	0	26.09	1831.95	49.30
0.55	0.097	0.130	73.67	0	28.69	1814.31	46.58
0.6	0.096	0.122	76.75	0	31.30	1781.70	43.69
0.65	0.093	0.114	79.47	0	33.91	1732.85	40.61
0.7	0.089	0.104	81.87	0	36.52	1664.02	37.30
0.75	0.085	0.095	84.00	0	39.13	1576.77	33.85
0.8	0.079	0.085	85.82	0	41.74	1472.93	30.29
0.85	0.072	0.074	87.29	0	44.34	1351.24	26.60
0.9	0.065	0.064	88.25	0	46.95	1211.02	22.76
0.95	0.057	0.053	88.20	0	49.56	1054.24	18.76
1	0.047	0.041	86.34	0	52.17	883.76	14.63
1.05	0.038	0.029	80.70	0	54.78	706.10	10.40
1.1	0.028	0.017	67.08	0	57.39	529.33	6.19
1.15	0.020	0.006	36.87	0	60.00	366.21	2.25

Table 18 – Performance characteristics for the optimized propeller for BL engine & Case II

7 Operational Optimization for a Typical Mission

In this Chapter, the second set of results obtained from OptProp is displayed. In Section 7.1 is displayed how some propeller parameters behave for a general mission. In Section 7.2 an optimization is performed for a given mission and then chosen a propeller among the solutions obtained. In Section 7.3, the chosen propeller is used for operational optimization. Then, the process is repeated considering structural constraints.

7.1 Design Exploration

A multi-objective optimization will be performed in the next Section 7.2 with two different objectives: power at the Takeoff point ($PowerToff$) and at the Top of Climb point ($PowerTOC$). In this Section, we seek to understand how such objectives will behave with the variation of design variables through design exploration. The first four design variables adopted are related to the airfoils used in four different propeller stations. As two airfoils of neighboring indexes can have completely different characteristics, it is not feasible to explore these first four design variables. Therefore, the variables propeller Diameter, Number of Blades, and the ratio between hub diameter and propeller diameter (HubDiameter/Diameter) will be adopted for design exploration.

The first two design explorations charts can be seen in Figures 109 and 110. In these cases, the influences of the Number of Blades and Diameter on the takeoff and Top of Climb powers were observed. It can be seen, through Figure 109, that the Diameter has a great influence on the value of the Top of Climb power, and the greater the value, the smaller the objective in question. The increase in the Number of Blades also causes a drop in the objective value, however, in a more subtle way.

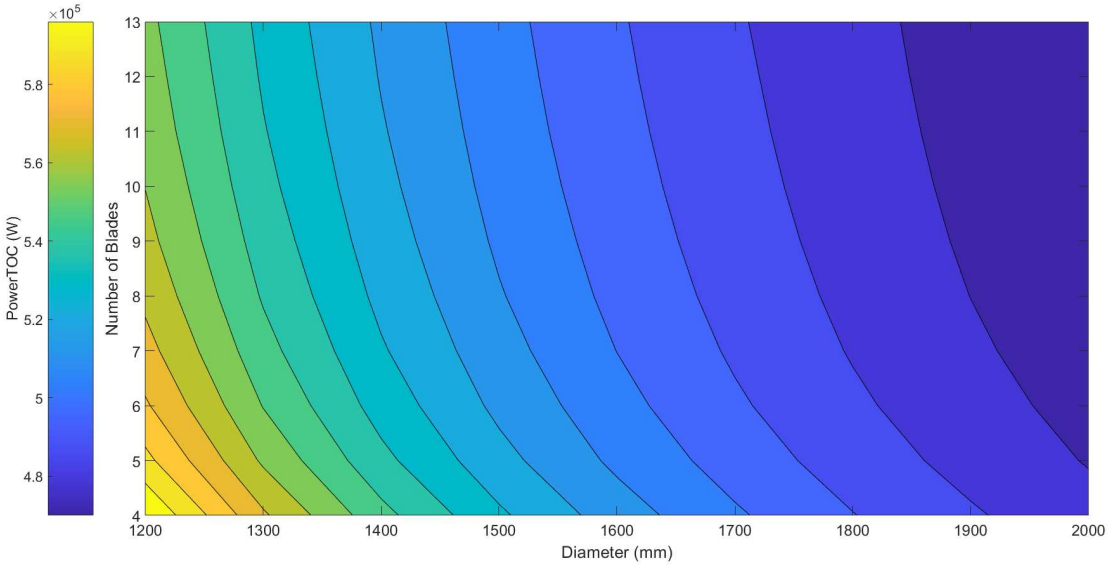

Figure 109 – Design Exploration - Number of Blades × Diameter - Top of Climb Power

Observing Figure 110, it is noticed that here also the increase in Diameter causes an important drop in the takeoff power value. The increase in the Number of Blades also causes a drop in objective value, but in an even more timid way than it did in Top of Climb power.

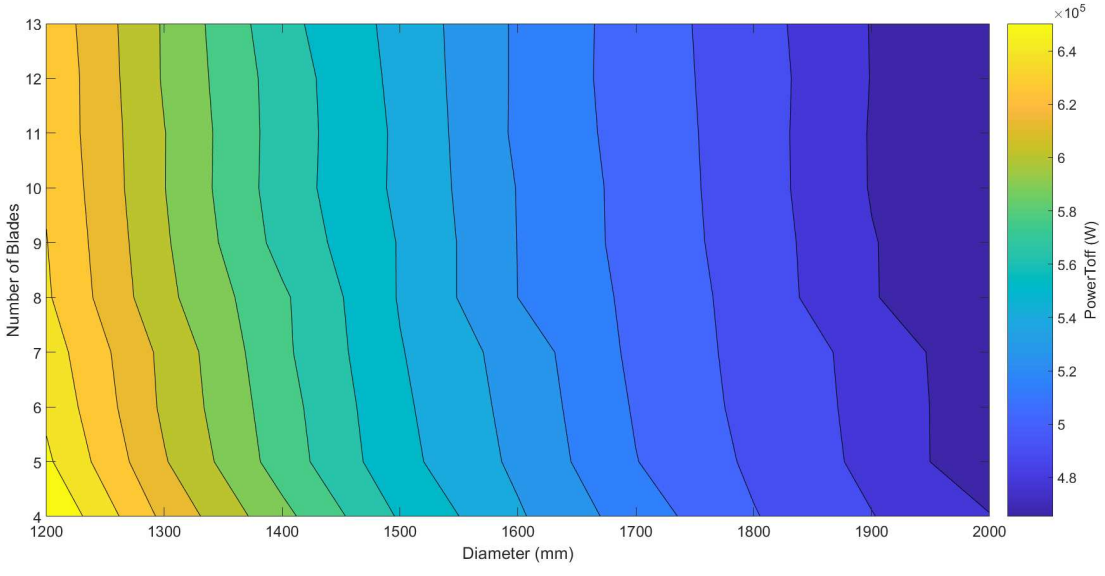

Figure 110 – Design Exploration - Number of Blades × Diameter - Takeoff Power

Figures 111 and 112 place the HubDiamater/Diameter and Diameter variables in design exploration for the two objective powers. In Figure 111 it can be seen that again

the Diameter has a great influence on the Top of Climb power. Increasing HubDiameter/Diameter causes a small increase in the objective.

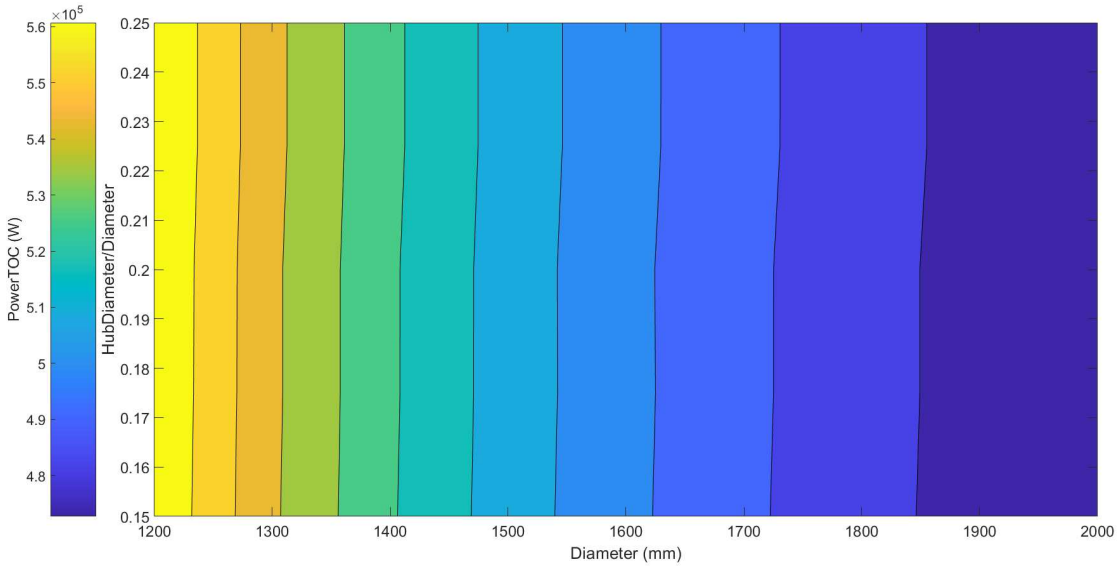

Figure 111 – Design Exploration - Hub Diameter (%) × Diameter - Top of Climb Power

Figure 112 shows similar results as the previous one: a larger Diameter causes a large decrease in takeoff power, while increasing HubDiameter/Diameter causes a small increase in objective.

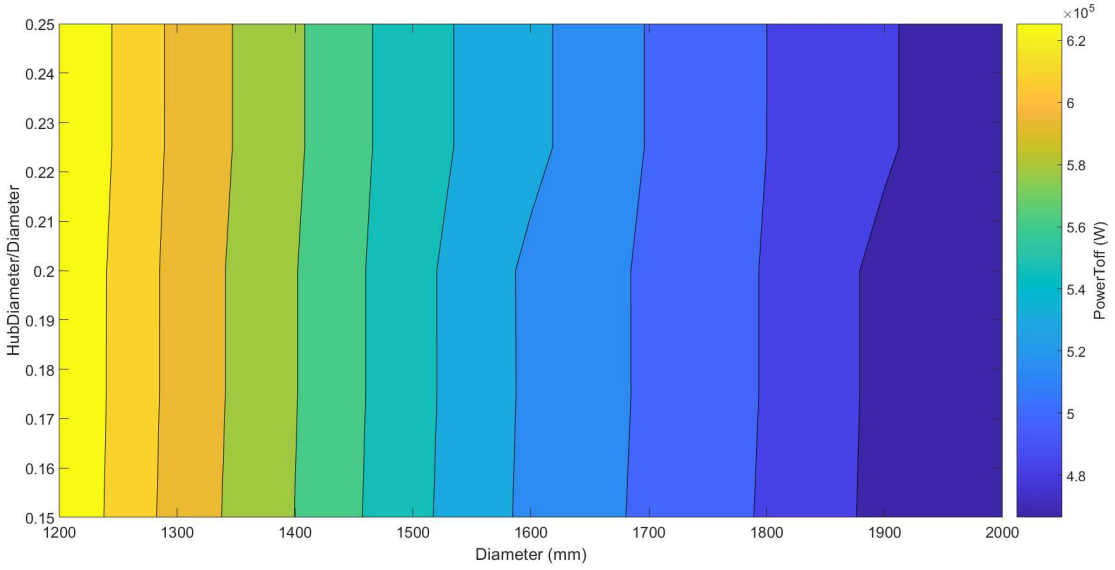

Figure 112 – Design Exploration - Hub Diameter (%) × Diameter - Takeoff Power

Through the design exploration, it is understood that increasing the Diameter and Number of Blades and decreasing the HubDiameter/Diameter will cause the minimization of both objectives. The main variable influence found was the Diameter, so the larger this variable is, the smaller the minimized objectives will be. In the first instance, one might think that propellers with the Diameter at the upper limit will be selected, but some constraints, such as the Mach number at the tip of the propeller, will limit this variable.

7.2 Propeller Optimization for a Typical Mission

This Section will present another optimization philosophy. Propeller Optimization for a Typical Mission will not care about dimensionless values, as done in the previous Section 6.2, but about absolute values of a mission. Mission data from a turboprop aircraft with two engines were used for the optimization carried out here. The chosen optimization points were Takeoff and Top of Climb:

- Takeoff
  - Total Thrust: 23.88 kN
  - Flight Mach Number: 0.135 (47.30 m/s)
  - Altitude: 0 m
- Top of Climb
  - Total Thrust: 7.01 kN
  - Flight Mach Number: 0.35 (114.15 m/s)
  - Altitude: 3048 m

The objective in this Section is to minimize the required values of power at the Takeoff point ($PowerToff$) and at the Top of Climb point ($PowerTO$). As the considered aircraft has two engines, the necessary value of total thrust was divided by two. Therefore, the multi-objective optimization problem can be written as:

$$\min \quad F(PowerTO, PowerToff) \tag{7.1}$$

$$
\begin{aligned}
\text{subject to} \quad & \frac{CR_{max}}{\overline{CR}_{max}} - 1 \leq 0, && && (7.2)\\
& -\frac{CR_{min}}{\overline{CR}_{min}} + 1 \leq 0, && && (7.3)\\
& -\frac{\alpha_{min}(i)}{\overline{\alpha}_{min}(i)} + 1 \leq 0, && i = [1,4] && (7.4)\\
& -\frac{\alpha_{max(i)}}{\overline{\alpha}_{max}(i)} + 1 \leq 0, && i = [1,4] && (7.5)\\
& -ReC(i) + 1 \leq 0, && i = [1,4] && (7.6)\\
& peak(i) - 1 \leq 0, && i = [1,4] && (7.7)\\
& RPM\_constraint \leq 0, && i = [1,4] && (7.8)\\
& 1 \leq x(i) \leq 4993, && i = [1,4] && (7.9)\\
& 1200 \leq x(5) \leq 2000, && && (7.10)\\
& 4 \leq x(6) \leq 13, && && (7.11)\\
& 0.150 \leq x(7) \leq 0.250, && && (7.12)\\
& 1000 \leq x(8) \leq 3000, && && (7.13)
\end{aligned}
$$

As can be seen in the optimization statement, some parameters were modified to more realistic values relative to the intended optimization, taking into account propeller characteristics used for turboprop aircraft with compatible dimensions. An eighth variable relative to the Rotational Speed value (RPM) for the Top of Climb point has been added. The Takeoff Rotational Speed point is found using the propeller designed by changing the pitch angle and Rotational Speed, looking for the lowest possible power within the limits. It was added a new constraint function called $RPM\_constraint$; this function has a value of 1 when the Mach number at the propeller tip assumes values equal to or greater than 0.8, and a value of 0 for smaller values. Such function is important to prevent noisy propellers due to the creation of shock waves. Excessively thin or thick profiles have been removed from the database, so the first four design variables can have their value up to 4932. The Diameter has been set to limits of $1200mm$ and $2000mm$. The number of possible blades was also modified for the range of 4 to 13, as well as the ratio of hub diameter and total diameter had its limits modified to 0.150 and 0.250. In order to reduce structural problems, the value of $\overline{CR}_{min}$ was changed to 0.04. In the present studies, the philosophy of integer optimization was adopted. In this way, values that were not integers by definition, such as Diameter, Hub/Diameter Ratio, and Rotational Speed, are treated as integers. In this way, computational errors arising from many decimal places are avoided. The diameter was treated in millimeters, the Hub/Diameter ratio minimum step was 0.1%, and the Rotational Speed minimum step is $1RPM$.

Thrust, Mach Speed, and Altitude for the design points are set on the objective

function. The proprieties related to the change in altitude, such as air density, kinematic viscosity, and speed of sound were also considered. Due to the good results demonstrated in the previous Section 6.2, NSGAII, AGEMOEA, and ARMOEA algorithms were chosen. For each run, 10,000 solutions were evaluated across 100 generations and populations with 100 individuals. For each of the three algorithms, 5 evaluations were performed, thus totaling 150,000 solutions. Such executions took approximately 125 hours and were performed on two different computers, with Intel Core i7-11800H and Intel Core i7-7700HQ processors. The results can be seen in Figure 113 below:

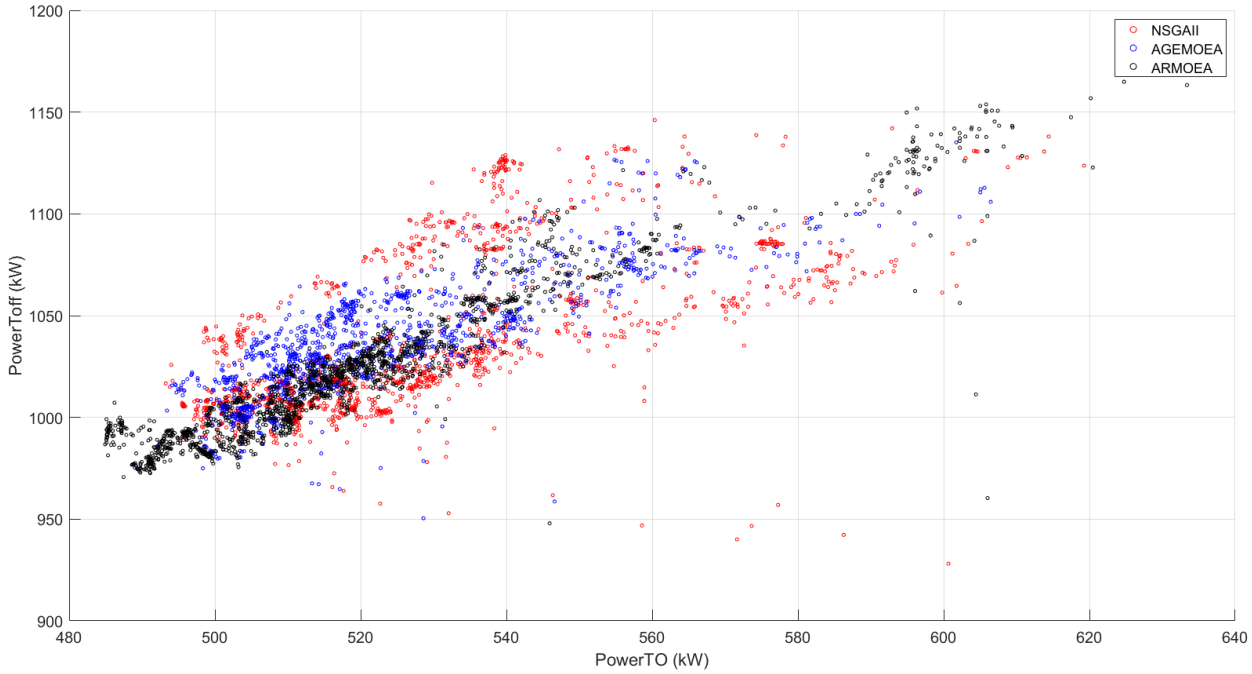

Figure 113 – Pareto for Propeller Optimization - PowerTO $\times PowerToff$

Through Figure 113, one can see that there is a tendency for the best solutions to be as good for $PowerTO$ as for $PowerToff$. Figure 114 below highlights the best objectives values:

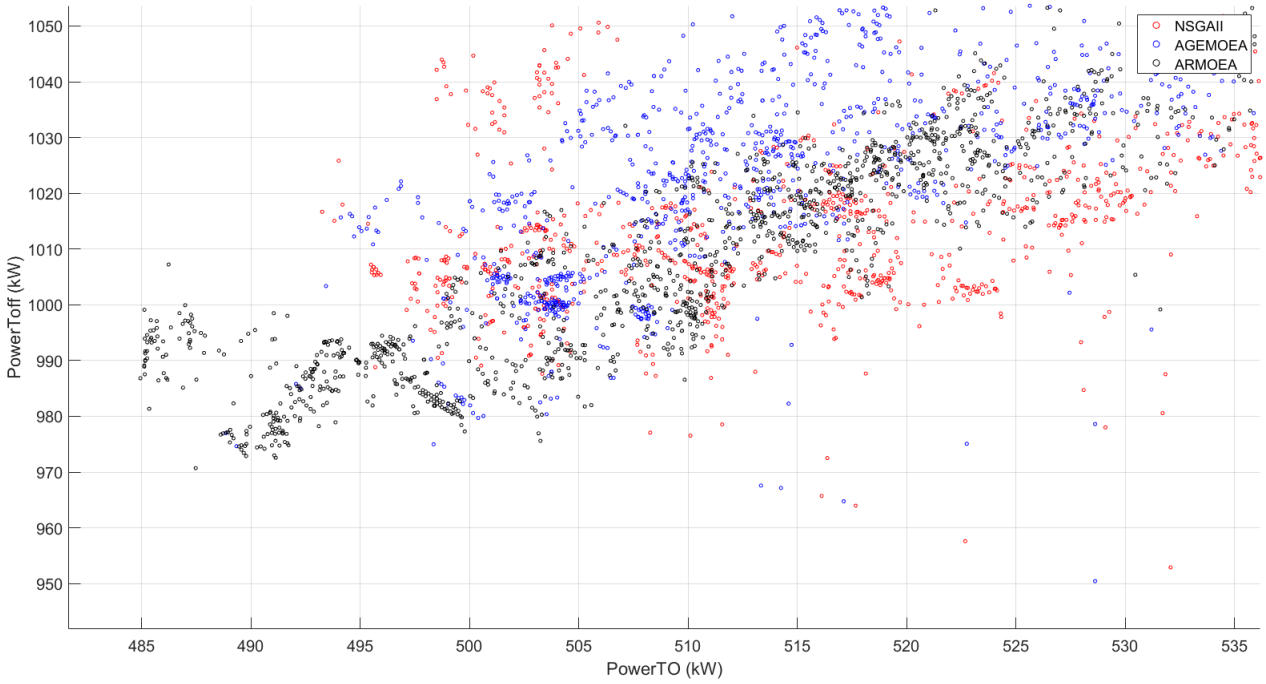

Figure 114 – Highlighted Pareto for Propeller Optimization - PowerTO $\times PowerToff$

It is possible to see that ARMOEA was successful in creating a large density of points to the left of the graph, providing solutions with lower powers at Top of Climb, while NSGAII and AGEMOEA were able to evaluate some points further down the graph, therefore providing solutions with lower Takeoff powers:

The solution extracted from the Pareto front in this Section was:

$$x = [1421, 4091, 3648, 3796, 1879, 8, 225, 1337] \tag{7.14}$$

representing a propeller with profiles FX 74-CL6-140, NPL ARC CP 1372, NACA 65(3)-218, and NACA M5, with a diameter of $1.879m$, with 8 blades, hub diameter ratio of 22.5%, and a rotational speed of $1337RPM$ at Top of Climb.

7.3 Operational Optimization

In this Section, a comparative study of two mission philosophies is proposed. In both cases, data related to the same standard mission of a turboprop aircraft divided into 103 different steps is considered. In Figure 115 below, it is possible to see how the altitude varies during the mission:

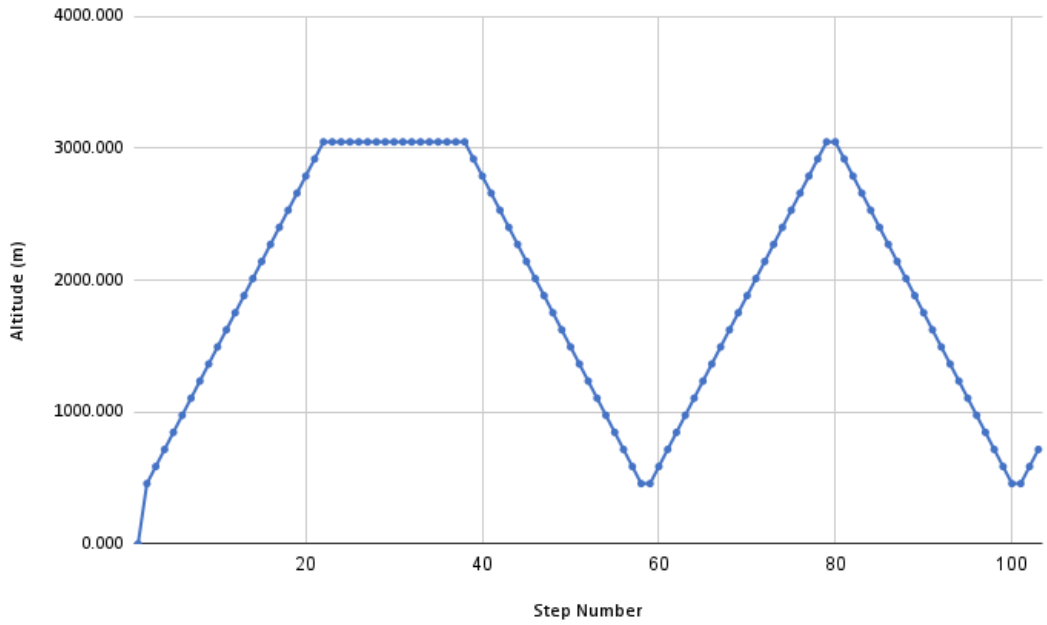

Figure 115 – Altitude versus Flight Mission Step

The mission can be divided into the following phases:

- 1) Takeoff: Step 1
- 2) Climb: Steps 2-22
- 3) Cruise: Steps 23-37
- 4) Descend: 38-58
- 5) Second Climb: 59-79
- 6) Second Descend: 80-100
- 7) Hold: 101-103

The first four items can be considered a typical mission for a turboprop aircraft. Items 5-7 refer to a situation where, for whatever reason, the aircraft cannot land and needs to regain its altitude to maneuver for the next landing. In order to carry out such a

mission, the values of aircraft velocity and thrust shown in Figures 116 and 117 must be achieved in each of the steps of the mission. The values shown for thrust are relative to each of the two engines, so the total aircraft thrust value is double that shown below.

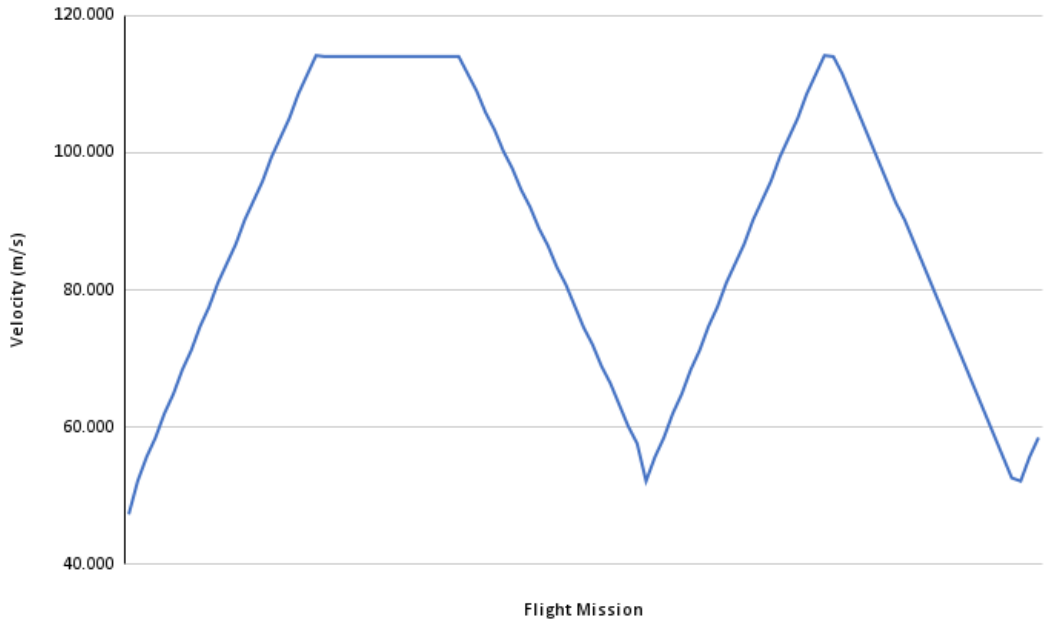

Figure 116 – Velocity versus Flight Mission Step

Figure 117 – Thrust versus Flight Mission Step

To carry out these missions, the propeller optimized in the previous Section 7.2 was

considered. The first mission philosophy, which is going to be called 3 Rotational Speed Flight, considers something that is already quite conventional in the current aeronautical industry, which is the use of three different points for the rotational speed of the engines. The second mission philosophy, called Multi Rotational Speed Flight, aims to use different values of rotational speed to minimize the power in each of the mission steps. Such a philosophy is not conventional in the aeronautical industry, however, it generates power savings and, therefore, fuel savings. This Section aims to demonstrate and measure this economy using different propeller rotational speeds throughout the flight mission. For this, in addition to the rotational speed changing at every step of the flight, it is also necessary to change the pitch angle of the propeller blades.

In this way, both mission philosophies were executed and the result for propeller rotational speeds are shown in Figure 118. For case 3 Rotational Speed Flight, the rotational speed levels were found, as well as the pitch angles, which minimize the power for each of the steps. The same was done for the Multi Rotational Speed Flight case. It can be seen when comparing Figures 117 and 118, that there is a shape correlation between required thrust and rotational speed for the Multi Rotational Speed Flight case.

Figure 118 – Propeller Rotational Speeds (RPM) for both philosophies

Figure 119 shows the savings generated in power when comparing the two cases. In some points, there is basically no difference, but in others, it can reach almost 10%.

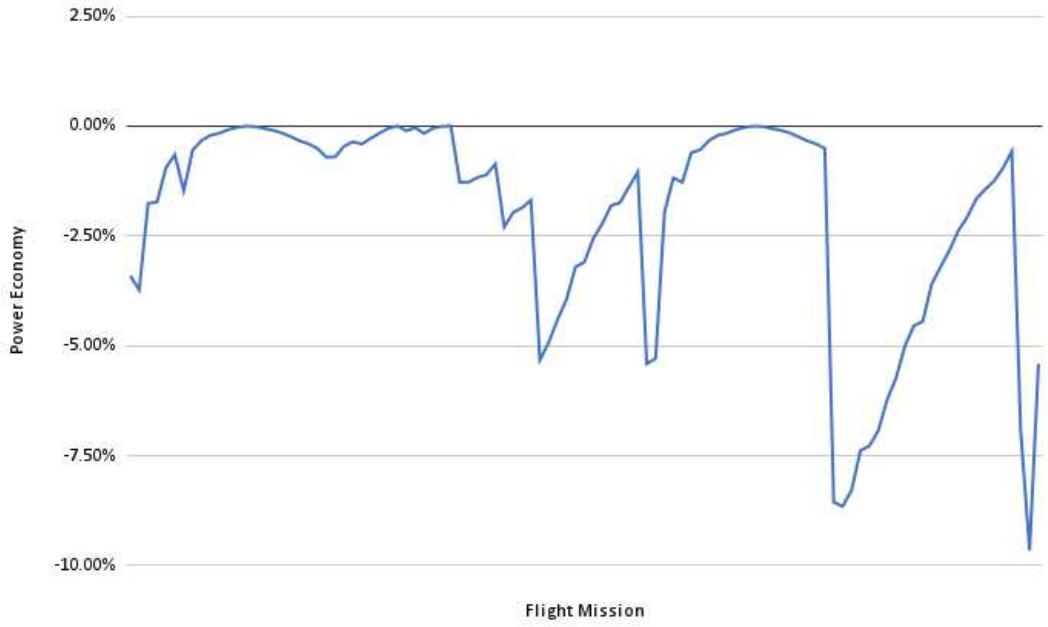

Figure 119 – Power economy comparing Multi Rotational Speed Flight and 3 Rotational Speed Flight

Propeller Efficiency (η) for both cases is shown in Figure 120. It is observed that these values are very close for both cases, with the Multi Rotational Speed Flight propeller efficiency showing a little higher efficiency in some regions. It is also possible to notice that the propeller efficiency is lower at points with high power requirements, such as Takeoff and Climb, and greater at points where the power requirement is lower, such as Cruise and Descend.

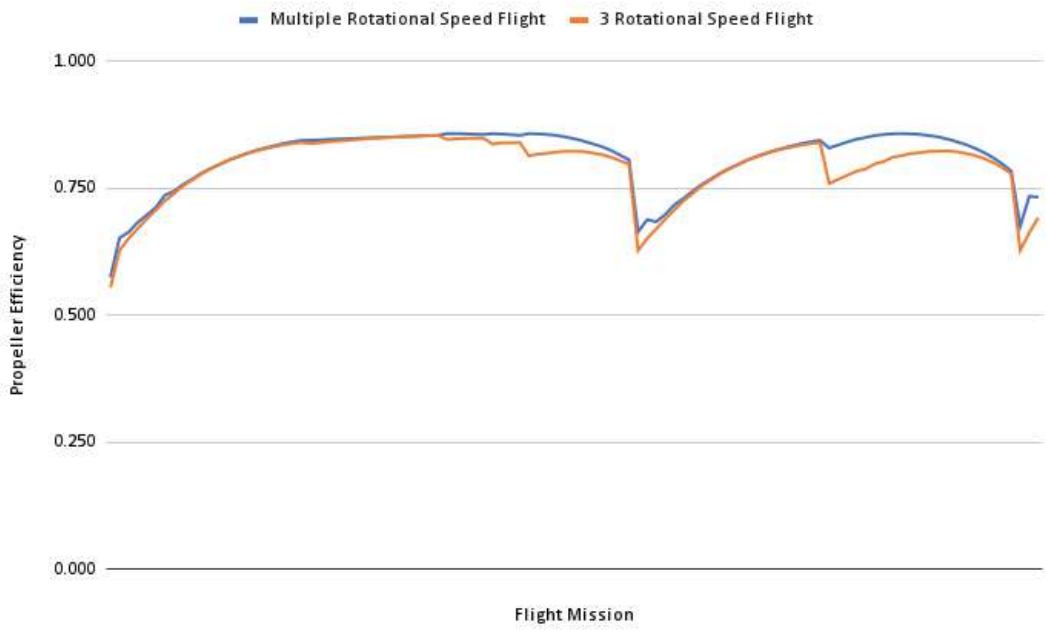

Figure 120 – Propeller Efficiency (η) for Multi Rotational Speed Flight and 3 Rotational Speed Flight

Figure 121 shows the variation of the coefficients of thrust (C_T) and power (C_P) along the flight for both cases. The values of the coefficients vary within the same range, however, it is noted that the coefficient values for the Multi Rotational Speed Flight vary more smoothly than in the 3 Rotational Speed Flight case. Such behavior can be attributed to the condition that the propeller rotational speed can assume any value.

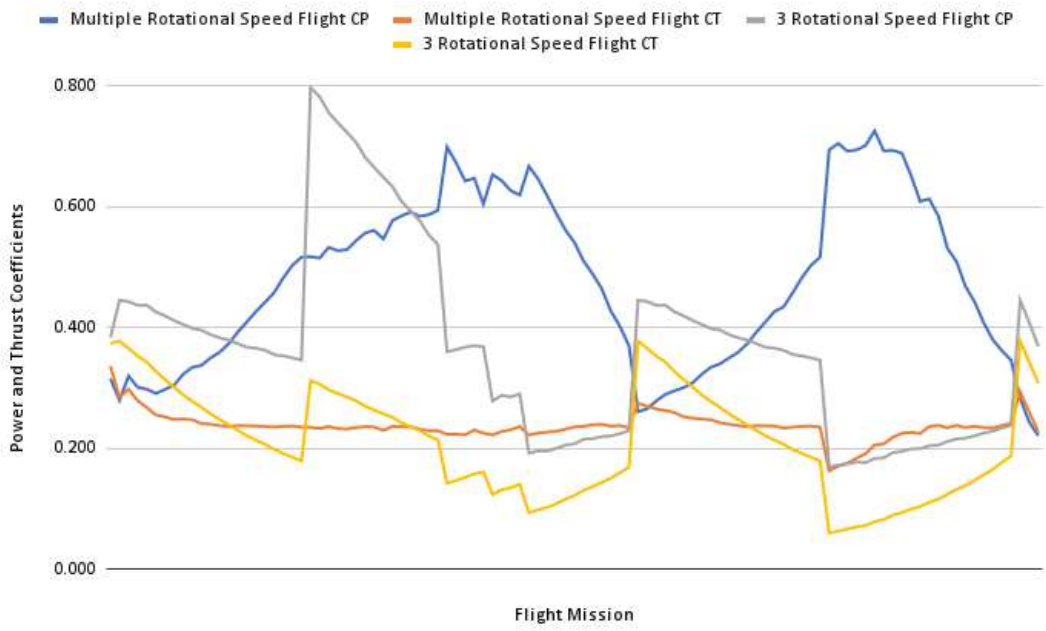

Figure 121 – Thrust (C_T) and Power (C_P) coefficients for Multi Rotational Speed Flight and 3 Rotational Speed Flight

Figure 122 shows how the Pitch Angle (β) behaves along the missions. As expected, where the rotational speed values are the same for both cases in Figure 118, the Pitch Angle values are also the same in Figure 122.

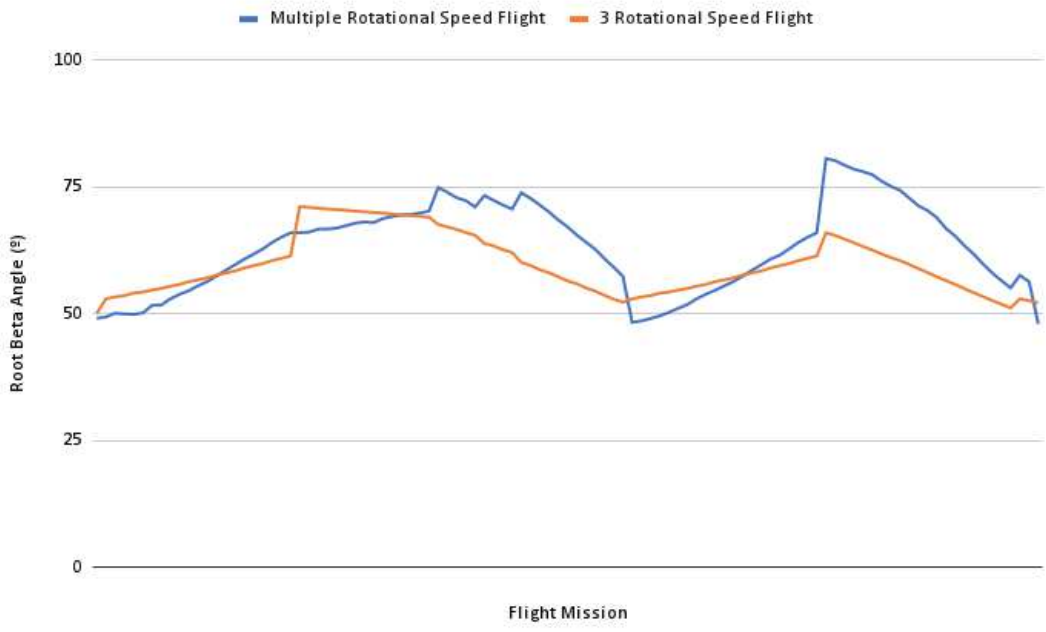

Figure 122 – Pitch Angle variation for Multi Rotational Speed Flight and 3 Rotational Speed Flight

Regarding the Total Energy used in a flight mission, it can be written as:

$$E_T = \sum_{i=1}^{i=103} Power_i \Delta t_i \tag{7.15}$$

where E_T is the Total Energy for a mission, $Power_i$ is the power, and Δt_i is the time for each of the steps. The percentage energy savings, therefore, can be written as:

$$Energy\_Economy(\%) = \frac{E_{TMulti} - E_{T3}}{E_{T3}} \tag{7.16}$$

where E_{TMulti} and E_{T3} are the Total Energies for each of the missions. Developing the Equations 7.16 and 7.15:

$$Energy\_Economy(\%) = \frac{\sum_{i=1}^{i=103} Power_{iMulti} \Delta t_{iMulti} - \sum_{i=1}^{i=103} Power_{i3} \Delta t_{i3}}{\sum_{i=1}^{i=103} Power_{i3} \Delta t_{i3}} \tag{7.17}$$

Assuming that all Δi time step values are equal, the Equation can be reduced to:

$$Energy\_Economy(\%) = \frac{\sum_{i=1}^{i=103} Power_{iMulti} - \sum_{i=1}^{i=103} Power_{i3}}{\sum_{i=1}^{i=103} Power_{i3}} \tag{7.18}$$

All values used in the Figures of this Section can be found in Appendix C. Applying these values to Equation 7.18 saves 1.47% in the Total Energy of the proposed mission, proving that the Multi Rotational Flight Speed philosophy can generate economic gains. Depending on the type of mission, these power-saving values can be even greater, since the more erratic a flight is, the less suitable the fixed rotational speed bands will be. Therefore, Multi Rotational Speed Flight can mean even lower flight energies and therefore lower fuel consumption for more complex missions.

7.3.1 Structural Constrained Operational Optimization

By applying the algorithm developed and presented in Section 5.3 to the optimized propeller in Section 7.2 its natural frequencies are obtained. Figure 123 presents the Campbell diagram for the propeller, where the first four-engine orders were considered, engine order equivalent to the number of blades, and twice the number of blades, that is, $EO = (1, 2, 3, 4, 8, 16)$

Through Figure 123, it is possible to see that there are some areas of intersection between the curves of the natural frequencies with the straight lines related to the engine order. These regions are called no-go zones, since they are rotation regions in which the

engines must not operate. It is possible to notice that in the region between $350RPM$ and $750RPM$ there are some intersections between natural frequencies and EO=16 (Figure 124), however, as the engine only operates passing through these frequencies and does not practice them in any part of the flight, for clarity on the chart, it was not marked as a no-go zone. In rotation $1244RPM$, the first vibration frequency coincides with $EO = 8$, as well as in rotation $2736RPM$, the intersection between the first frequency and $EO = 4$ occurs. As these are rotation frequencies in the aircraft operating range, two no-go zones are generated considering errors of $\pm 2\%$ in natural frequencies, resulting in the ranges $1213 - 1275RPM$ and $2668 - 2804RPM$.

When analyzing the flight data presented in Section 7.3, it is observed that the rotations used in some segments are within the no-go zones: Step Take Off (Step 1), Descent (Steps 42, 52, and 53), and Second Descent (Steps 93 and 94). To fix this issue, the rotations of these segments are swapped with the closest allowed rotation, and the referring data is recalculated, as can be seen in Table 19 and Figure 125 shows the rotations along the mission when the structural constraint is considered.

Segment (Step Number)	Velocity	Thrust	RPM	Power	CP	CT	Eta	Beta
[-]	[m/s]	[N]	[rpm]	[kW]	[-]	[-]	[-]	[°]
TakeOff (1)	47.30	11137.3	2668	942.1	0.373	0.369	0.559	49.79
Descent (42)	100.21	1417.0	1275	165.9	0.645	0.220	0.858	73.22
Descent (52)	74.53	1445.9	1213	127.0	0.555	0.240	0.848	67.49
Descent (53)	72.03	1555.3	1275	132.7	0.498	0.233	0.843	65.28
Second Descent (93)	74.53	1467.9	1213	129.2	0.567	0.245	0.847	67.59
Second Descent (94)	71.40	1567.1	1275	132.8	0.500	0.236	0.842	65.13

Table 19 – New flight mission points considering structural constraints

Due to the structural constraint applied and some segments no longer being in minimum power rotation, the energy saving obtained here (1.40%) is slightly smaller than that obtained in Section 7.3 (1.47%), where there are no structural constraints. However, because few segments were affected by the constraint, there was no major change in energy savings.

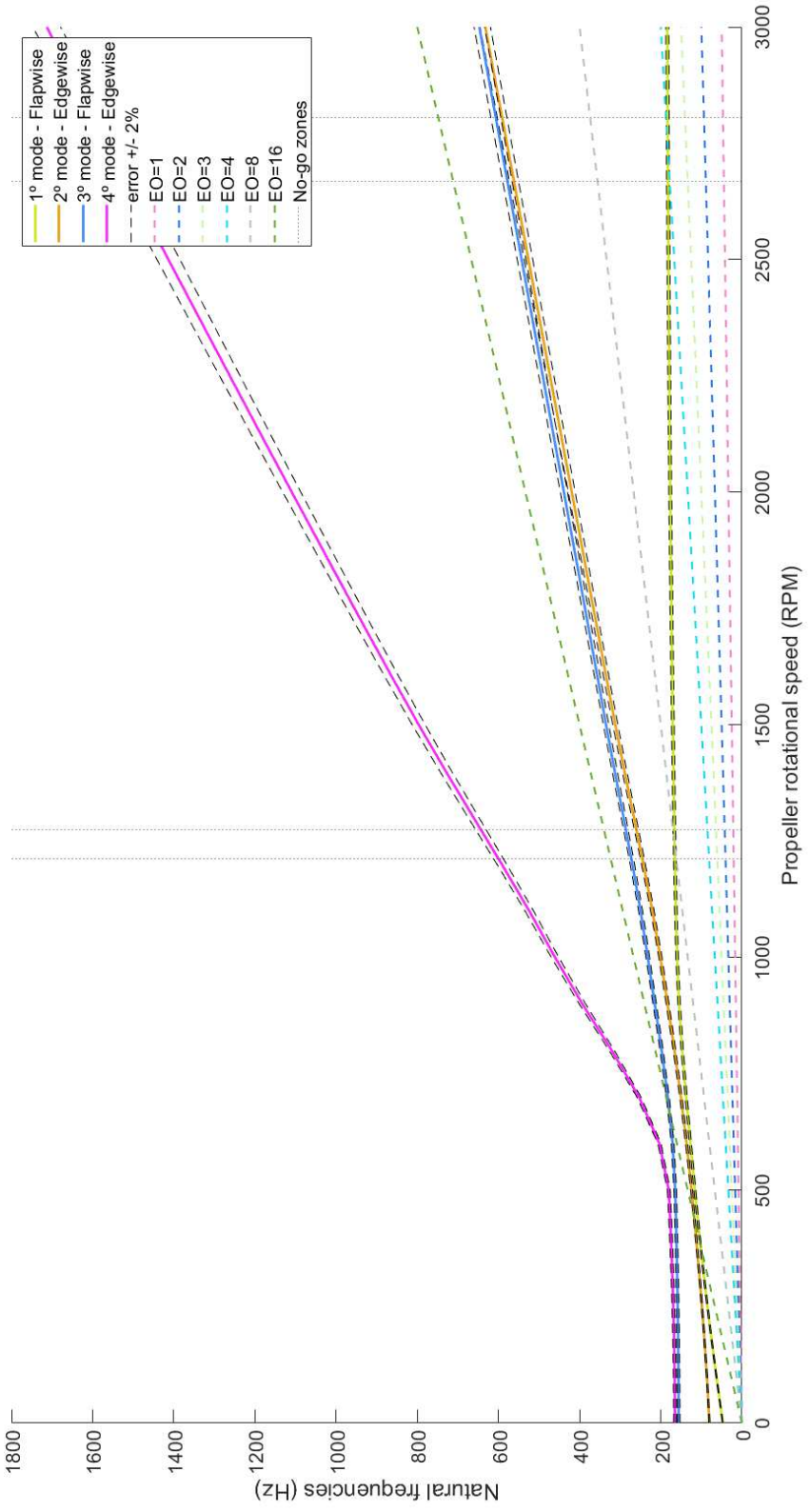

Figure 123 – Campbell Diagram

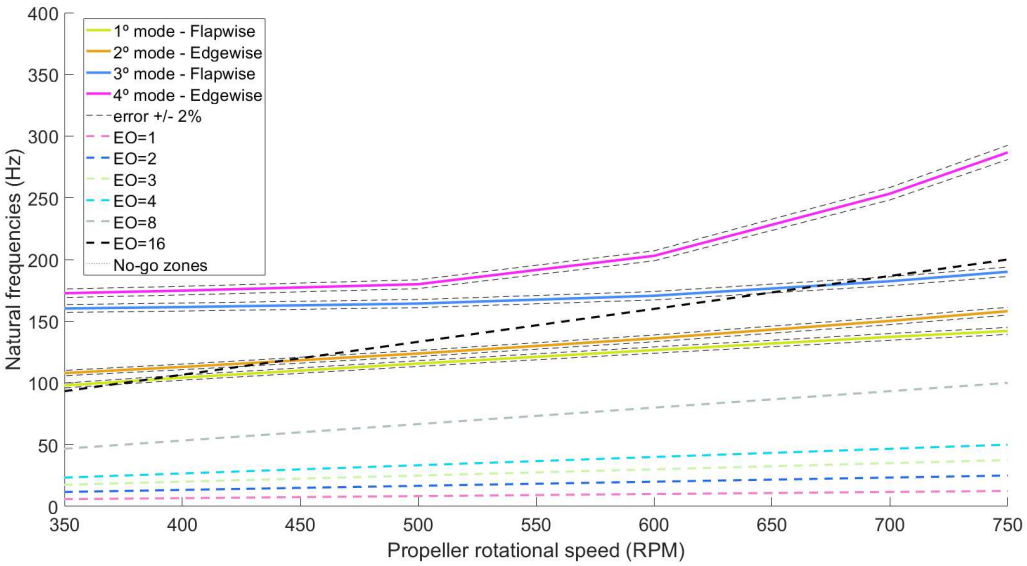

Figure 124 – Campbell Diagram - 350-750RPM range

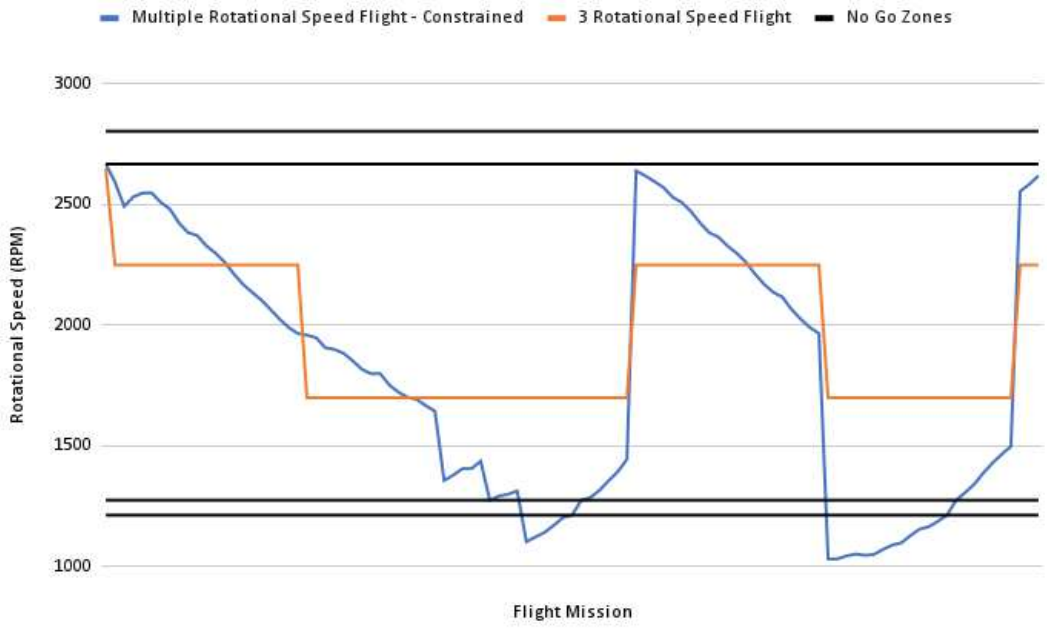

Figure 125 – Propeller Rotational Speeds (RPM) for No Go Zones

8 Final Considerations

This work presented a multi-objective optimum design of propellers using BEMT and evolutionary algorithms called OptProp.

At first, seven multi-objective optimization problems were formulated considering various conflicting objective functions, such as C_T, C_M, η, and the propeller volume. This process, called Propeller Parameters Optimization (6.2), was carried out through dimensionless parameters. Five evolutionary algorithms were used to solve these problems, and with the results, the Pareto fronts in two, three, and four dimensions were obtained. Performance analyses were carried out considering these Pareto fronts through four metrics, in which it was possible to detect the algorithms that presented the best performance in the comparisons.

The possibility of extracting solutions from these Pareto fronts according to some criterion is considered an essential aspect. A visual inspection was not used for this, but a strategy based on weights defined by the decision-maker according to his preferences (multi-criteria decision-making). Four types of extractions were illustrated in one of the problems analyzed in this paper. Two scenarios were simulated with weights chosen by the decision-maker concerning both engines adopted in the experiments. Analyzes were carried out regarding the resolution capacity of the proposed problems for each of the five evolutionary algorithms used.

Then, another optimization was performed, this time considering absolute values, specifically the powers required at two points of the flight mission: Takeoff and Top of Climb. This process was called Propeller Optimization (Section 7.2). Three different evolutionary algorithms were used to obtain a Pareto front, from which a propeller was extracted.

Finally, another optimization called Operational Optimization (Section 7.3) was performed. From the propeller obtained in Section 7.2, a flight mission was optimized in search of the minimum power required for each mission point by varying the values of rotational speed and pitch angle. This process was performed freely and constrained, obtaining the general flight energy reduction values of (1.47%) and (1.40%), respectively.

The proposed methodology enabled the design of efficient propellers systematically and pragmatically. The results obtained demonstrate its potential, providing feasible non-dominated solutions and significantly reducing computational costs using the BEMT theory. Furthermore, it corroborates with the various studies in the area that aim, above all, to improve the efficiencies of aeronautical systems while trying to mitigate environmental and economic impacts.

For future work, applying high-fidelity methods to the obtained propeller with

multi-criteria decision-making is of great interest. Another point of improvement is creating a new coupled propeller analysis code that allows the inclusion of Boundary Layer Ingestion effects.

Acknowledgments

The author wishes to thank CAPES (Finance Code 001) for their financial support. For academic development and guidance, the author thanks the Graduate Program in Computational Modeling (PGMC) at the Federal University of Juiz de Fora (UFJF), and the Future Energy Center (FEC) at Mälardalen University (MDU).

Bibliography

1 Barnes W McCormick. Aerodynamics aeronautics and flight mechanics john wiley & sons. *Inc., New York*, 1979.

2 David Wall. *Optimum propeller design for electric UAVS*. PhD thesis, Auburn University, 2012.

3 Regina Mitsue Azuma et al. Otimização multiobjetivo em problema de estoque e roteamento gerenciados pelo fornecedor. 2011.

4 MK Benhachmi, D Ouazar, A Naji, AHD Cheng, and K Harrouni. Pumping optimization in saltwater intruded aquifers by simple genetic algorithm—deterministic model. In *2nd International Conference on Saltwater Intrusion and Coastal Aquifers–Monitoring, Modelling and Management*, 2003.

5 Walter Ramberg and Sam Levy. Calculation of stresses and natural frequencies for a rotating propeller blade vibrating flexurally. *Journal of Research, National Bureau of Standards*, 21, 1938.

6 Jungang Lü, Jiadao Wang, and Darong Chen. Transverse vibration of the blade for unmanned micro helicopter using rayleigh-ritz method. *International Journal of Minerals, Metallurgy and Materials*, 10(6):40–43, 2003.

7 Ajinkya Baxy and Abhijit Sarkar. Natural frequencies of a rotating curved cantilever beam: A perturbation method-based approach. *Proceedings of the Institution of Mechanical Engineers, Part C: Journal of Mechanical Engineering Science*, 234(9):1706–1719, 2020.

8 SS Rao and RS Gupta. Finite element vibration analysis of rotating timoshenko beams. *Journal of Sound and vibration*, 242(1):103–124, 2001.

9 Meherwan P Boyce. *Gas turbine engineering handbook*. Elsevier, 2011.

10 Martin Hepperle. Java prop website, 2020 (accessed September 12, 2020). `https://www.mh-aerotools.de/airfoils/javaprop.htm`.

11 J. P. Morgado. Guidelines jblade v5.17, 2020 (accessed September 12, 2020). `https://sites.google.com/site/joaomorgado23/downloads`.

12 M Drela. Qprop theory document. *web. mit. edu/drela/Public/Qprop*, 2006.

13 Érica da Costa Reis Carvalho. Um algoritmo por enxame de partículas para a solução de problemas de otimização estrutural multiobjetivo considerando frequências naturais de vibração. 2018.

14 Evan J Hughes. Msops-ii: A general-purpose many-objective optimiser. In *2007 IEEE Congress on Evolutionary Computation*, pages 3944–3951. IEEE, 2007.

15 Jun Yi, Junren Bai, Haibo He, Jun Peng, and Dedong Tang. ar-moea: A novel preference-based dominance relation for evolutionary multiobjective optimization. *IEEE Transactions on Evolutionary Computation*, 23(5):788–802, 2018.

16 Annibale Panichella. An adaptive evolutionary algorithm based on non-euclidean geometry for many-objective optimization. In *Proceedings of the Genetic and Evolutionary Computation Conference*, pages 595–603, 2019.

17 Linqiang Pan, Wenting Xu, Lianghao Li, Cheng He, and Ran Cheng. Adaptive simulated binary crossover for rotated multi-objective optimization. *Swarm and Evolutionary Computation*, 60:100759, 2021.

18 Chun Hern Tan, Keng Soon Voo, Wei Long Siauw, James Alderton, Amel Boudjir, and Fred Mendonça. Cfd analysis of the aerodynamics and aeroacoustics of the nasa sr2 propeller. In *Turbo Expo: Power for Land, Sea, and Air*, volume 45608, page V02AT41A010. American Society of Mechanical Engineers, 2014.

19 RM Bass. An historical review of propeller developments. *The Aeronautical Journal*, 87(867):255–267, 1983.

20 John F Keane and Stephen S Carr. A brief history of early unmanned aircraft. *Johns Hopkins APL Technical Digest*, 32(3):558–571, 2013.

21 Nanyaporn Intaratep, William N Alexander, William J Devenport, Sheryl M Grace, and Amanda Dropkin. Experimental study of quadcopter acoustics and performance at static thrust conditions. In *22nd AIAA/CEAS Aeroacoustics Conference*, page 2873, 2016.

22 IPCC IPCC. Special report on aviation and the global atmosphere, 1999.

23 Egbert Torenbeek. *Synthesis of subsonic airplane design: an introduction to the preliminary design of subsonic general aviation and transport aircraft, with emphasis on layout, aerodynamic design, propulsion and performance*. Springer Science & Business Media, 2013.

24 W. J. Macquorn Rankine. On the mechanical principles of the action of propellers. *Transactions of the Institution of Naval Architects.*, Vol 6:13–39, 1865.

25 Robert Edmund Froude. On the part played in propulsion by differences of fluid pressure. *Transactions of the Institution of Naval Architects*, Vol. 30:390, 1889.

26 Quentin R Wald. The aerodynamics of propellers. *Progress in Aerospace Sciences*, 42(2):85–128, 2006.

27 C Adkins and R LIEBECK. Design of optimum propellers. In *21st Aerospace Sciences Meeting*, page 190, 1983.

28 Charles N Adkins and Robert H Liebeck. Design of optimum propellers. *Journal of Propulsion and Power*, 10(5):676–682, 1994.

29 Stefan Drzewiecki. *Théorie générale de l'hélice: hélices aériennes et hélices marines*. Gauthier-Villars, Paris, 1920.

30 Hermann Glauert. Airplane propellers. In *Aerodynamic theory*, pages 169–360. Springer, 1935.

31 Theodore Theodorsen. *Theory of propellers*. McGraw-Hill Book Company, 1948.

32 Martin Beaudoin and Hrvoje Jasak. Development of a generalized grid interface for turbomachinery simulations with openfoam. In *Open source CFD International conference*, volume 2. Berlin, 2008.

33 R Malki, AJ Williams, TN Croft, M Togneri, and I Masters. A coupled blade element momentum–computational fluid dynamics model for evaluating tidal stream turbine performance. *Applied Mathematical Modelling*, 37(5):3006–3020, 2013.

34 S Bahrami, C Tribes, C Devals, TC Vu, and F Guibault. Multi-fidelity shape optimization of hydraulic turbine runner blades using a multi-objective mesh adaptive direct search algorithm. *Applied mathematical modelling*, 40(2):1650–1668, 2016.

35 Thomas Pulliam, Marian Nemec, Terry Holst, and David Zingg. Comparison of evolutionary (genetic) algorithm and adjoint methods for multi-objective viscous airfoil optimizations. In *41st Aerospace Sciences Meeting and Exhibit*, page 298, 2003.

36 Masahiro Kanazaki, Kentaro Tanaka, Shinkyu Jeong, and Kazuomi Yamamoto. Multi-objective aerodynamic optimization of elements' setting for high-lift airfoil using kriging model. In *44th AIAA Aerospace Sciences Meeting and Exhibit*, page 1471, 2006.

37 Sumeet Parashar, Valentino Pediroda, and Carlo Poloni. Self organizing maps (som) for design selection in robust multi-objective design of aerofoil. In *46th AIAA Aerospace Sciences Meeting and Exhibit*, page 914, 2008.

38 Lee Cameron, Juiana Early, and Richard McRoberts. Metamodel assisted multi-objective global optimisation of natural laminar flow aerofoils. In *29th AIAA Applied Aerodynamics Conference*, page 3001, 2011.

39 Ernesto Benini, Rita Ponza, and Andrea Massaro. High-lift multi-element airfoil shape and setting optimization using multi-objective evolutionary algorithms. *Journal of aircraft*, 48(2):683–696, 2011.

40 AFP Ribeiro, AM Awruch, and HM Gomes. An airfoil optimization technique for wind turbines. *Applied Mathematical Modelling*, 36(10):4898–4907, 2012.

41 Sheng Qiu, Wenbin Song, and Hong Liu. Multi-objective optimization of airfoil trailing edge noise with three different measures. In *18th AIAA/CEAS aeroacoustics conference (33rd AIAA aeroacoustics conference)*, page 2182, 2012.

42 Slawomir Koziel and Leifur T Leifsson. Multi-objective airfoil design using variable-fidelity cfd simulations and response surface surrogates. In *10th AIAA Multidisciplinary Design Optimization Conference*, page 0289, 2014.

43 Aleksandar Kovačević, Jelena Svorcan, Mohammad Sakib Hasan, Toni Ivanov, and Miroslav Jovanović. Optimal propeller blade design, computation, manufacturing and experimental testing. *Aircraft Engineering and Aerospace Technology*, 2021.

44 Li Ko Chang and John P Sullivan. Optimization of propeller blade twist by an analytical method. *AIAA journal*, 22(2):252–255, 1984.

45 Jinsoo Cho and Seung-Chul Lee. Propeller blade shape optimization for efficiency improvement. *Computers & fluids*, 27(3):407–419, 1998.

46 Johann Dorfling and Kamran Rokhsaz. Constrained and unconstrained propeller blade optimization. *Journal of Aircraft*, 52(4):1179–1188, 2015.

47 Sydney Goldstein. On the vortex theory of screw propellers. *Proceedings of the Royal Society of London. Series A, Containing Papers of a Mathematical and Physical Character*, 123(792):440–465, 1929.

48 Markus E Schatz, Andreas Hermanutz, and Horst J Baier. Multi-criteria optimization of an aircraft propeller considering manufacturing. *Structural and Multidisciplinary Optimization*, 55(3):899–911, 2017.

49 Usama T Toman, Abdel-Karim SO Hassan, Farouk M Owis, and Ahmed SA Mohamed. Blade shape optimization of an aircraft propeller using space mapping surrogates. *Advances in Mechanical Engineering*, 11(7):1687814019865071, 2019.

50 Ali Alshahrani. *Analysis and Initial Optimization of The Propeller Design for Small, Hybrid-Electric Propeller Aircraft.* PhD thesis, Aeronautical and Vehicle Engineering KTH Royal Institute of Technology, Stockholm, Sweden, 2020.

51 Antonio Pagano, Luigi Federico, Mattia Barbarino, Fabio Guida, and Marco Aversano. Multi-objective aeroacoustic optimization of an aircraft propeller. In *12th AIAA/ISSMO multidisciplinary analysis and optimization conference*, page 6059, 2008.

52 Benoit Marinus, Michel Roger, and René Van Den Braembussche. Aeroacoustic and aerodynamic optimization of aircraft propeller blades. In *16th AIAA/CEAS aeroacoustics conference*, page 3850, 2010.

53 Rens MacNeill and Dries Verstraete. Optimal propellers for a small hybrid electric fuel-cell uas. In *2018 AIAA/IEEE Electric Aircraft Technologies Symposium (EATS)*, pages 1–16. IEEE, 2018.

54 Svatomir Slavik, Jan Klesa, and Jiri Brabec. Propeller selection by means of pareto-optimal sets applied to flight performance. *Aerospace*, 7(3):21, 2020.

55 Timothy Ganesan, Mohd Shiraz Aris, and Pandian Vasant. Extreme value metaheuristics for optimizing a many-objective gas turbine system. *International Journal of Energy Optimization and Engineering (IJEOE)*, 7(2):76–96, 2018.

56 M Gul, MA Kalam, MA Mujtaba, Saira Alam, M Nasir Bashir, Iqra Javed, Umair Aziz, M Rizwan Farid, M Tahir Hassan, and Shahid Iqbal. Multi-objective-optimization of process parameters of industrial-gas-turbine fueled with natural gas by using grey-taguchi and ann methods for better performance. *Energy Reports*, 6:2394–2402, 2020.

57 Mohsen Sadeghi, Ata Chitsaz, Parisa Marivani, Mortaza Yari, and SMS Mahmoudi. Effects of thermophysical and thermochemical recuperation on the performance of combined gas turbine and organic rankine cycle power generation system: Thermoeconomic comparison and multi-objective optimization. *Energy*, 210:118551, 2020.

58 Xiaoyi Ding, Wei Sun, Gareth P Harrison, Xiaojing Lv, and Yiwu Weng. Multi-objective optimization for an integrated renewable, power-to-gas and solid oxide fuel cell/gas turbine hybrid system in microgrid. *Energy*, 213:118804, 2020.

59 Dave P Witkowski, Alex KH Lee, and John P Sullivan. Aerodynamic interaction between propellers and wings. *Journal of Aircraft*, 26(9):829–836, 1989.

60 John Brandt and Michael Selig. Propeller performance data at low reynolds numbers. In *49th AIAA Aerospace Sciences Meeting including the New Horizons Forum and Aerospace Exposition*, page 1255, 2011.

61 Robert W. Deters, Gavin K. Ananda, and Michael S. Selig. Reynolds Number Effects on the Performance of Small Scale Propellers. *In Proceedings of the 32nd AIAA Applied Aerodynamics Conference*, 2014.

62 Nowrouz Mohammad Nouri, Saber Mohammadi, and Masoud Zarezadeh. Optimization of a marine contra-rotating propellers set. *Ocean Engineering*, 167:397–404, 2018.

63 Ya-Jung Lee and Ching-Chieh Lin. Optimized design of composite propeller. *Mechanics of advanced materials and structures*, 11(1):17–30, 2004.

64 Ohad Gur and Aviv Rosen. Optimization of propeller based propulsion system. *Journal of Aircraft*, 46(1):95–106, 2009.

65 Eric Vargas Loureiro, Nicolas Lima Oliveira, Patricia Habib Hallak, Flávia de Souza Bastos, Lucas Machado Rocha, Rafael Grande Pancini Delmonte, and Afonso Celso de Castro Lemonge. Evaluation of low fidelity and cfd methods for the aerodynamic performance of a small propeller. *Aerospace Science and Technology*, 108:106402, 2021.

66 Jurij Sodja, Domen Stadler, and Tadej Kosel. Computational fluid dynamics analysis of an optimized load-distribution propeller. *Journal of aircraft*, 49(3):955–961, 2012.

67 Stefano Gaggero, Giorgio Tani, Diego Villa, Michele Viviani, Pierluigi Ausonio, Piero Travi, Giovanni Bizzarri, and Francesco Serra. Application of multi-objective optimization based design to high-speed craft propellers. In *Proceedings of Fifth International Symposium on Marine Propulsors. Espoo, Finland*, volume 1, pages 278–290, 2017.

68 Stefano Gaggero, Giorgio Tani, Diego Villa, Michele Viviani, Pierluigi Ausonio, Piero Travi, Giovanni Bizzarri, and Francesco Serra. Efficient and multi-objective cavitating propeller optimization: an application to a high-speed craft. *Applied Ocean Research*, 64:31–57, 2017.

69 Jingwei Jiang, Haopeng Cai, Cheng Ma, Zhengfang Qian, Ke Chen, and Peng Wu. A ship propeller design methodology of multi-objective optimization considering fluid–structure interaction. *Engineering Applications of Computational Fluid Mechanics*, 12(1):28–40, 2018.

70 Manudha T Herath, Sundararajan Natarajan, B Gangadhara Prusty, and Nigel St John. Smoothed finite element and genetic algorithm based optimization for shape adaptive composite marine propellers. *Composite Structures*, 109:189–197, 2014.

71 Arne Stuermer. Unsteady cfd simulations of propeller installation effects. In *42nd AIAA/ASME/SAE/ASEE Joint Propulsion Conference & Exhibit*, page 4969, 2006.

72 Hrvoje Jasak and Martin Beaudoin. Openfoam turbo tools: From general purpose cfd to turbomachinery simulations. In *ASME-JSME-KSME 2011 Joint Fluids Engineering Conference*, pages 1801–1812. American Society of Mechanical Engineers, 2011.

73 Hyunbum Park. Advanced turboprop composite propeller design and analysis using fluid–structure interaction method. *Composites Part B: Engineering*, 97:111 – 119, 2016.

74 MH Mohamed. Reduction of the generated aero-acoustics noise of a vertical axis wind turbine using cfd (computational fluid dynamics) techniques. *Energy*, 96:531–544, 2016.

75 Hairuniza Ahmed Kutty and Parvathy Rajendran. 3d cfd simulation and experimental validation of small apc slow flyer propeller blade. *Aerospace*, 4(1):10, 2017.

76 Kurt Mizzi, Yigit Kemal Demirel, Charlotte Banks, Osman Turan, Panagiotis Kaklis, and Mehmet Atlar. Design optimisation of propeller boss cap fins for enhanced propeller performance. *Applied Ocean Research*, 62:210–222, 2017.

77 Giulia Chirico, George N Barakos, and Nicholas Bown. Numerical aeroacoustic analysis of propeller designs. *The Aeronautical Journal*, 122(1248):283–315, 2018.

78 Giulia Chirico, George N Barakos, and Nicholas Bown. Propeller installation effects on turboprop aircraft acoustics. *Journal of Sound and Vibration*, 424:238–262, 2018.

79 Przemysław Król and Krzysztof Tesch. Experimental and numerical validation of the improved vortex method applied to cp745 marine propeller model. *Polish Maritime Research*, 25(2):57–65, 2018.

80 Jurij Sodja, Roeland De Breuker, Dejan Nozak, Radovan Drazumeric, and Pier Marzocca. Assessment of low-fidelity fluid–structure interaction model for flexible propeller blades. *Aerospace Science and Technology*, 78:71–88, 2018.

81 José D Hoyos, Jesús H Jiménez, Camilo Echavarría, Juan P Alvarado, and Germán Urrea. Aircraft propeller design through constrained aero-structural particle swarm optimization. *Aerospace*, 9(3):153, 2022.

82 Yang Zhang, Yifan Fu, Peng Wang, and Min Chang. Aerodynamic configuration optimization of a propeller using reynolds-averaged navier–stokes and adjoint method. *Energies*, 15(22):8588, 2022.

83 Xiaopeng Yang, Dongli Ma, Liang Zhang, Yayun Yu, Yuan Yao, and Muqing Yang. High-fidelity multi-level efficiency optimization of propeller for high altitude long endurance uav. *Aerospace Science and Technology*, 133:108142, 2023.

84 Heyecan Koyuncuoglu and Ping He. Cfd based multi-component aerodynamic optimization for wing propeller coupling. In *AIAA SCITECH 2023 Forum*, page 1844, 2023.

85 Xin Geng, Peiqing Liu, Tianxiang Hu, Qiulin Qu, Jiahua Dai, Changhao Lyu, Yunsong Ge, and Rinie AD Akkermans. Multi-fidelity optimization of a quiet propeller based on deep deterministic policy gradient and transfer learning. *Aerospace Science and Technology*, page 108288, 2023.

86 Guan Guan, Xiangyu Zhang, Panpan Wang, and Qu Yang. Multi-objective optimization design method of marine propeller based on fluid-structure interaction. *Ocean Engineering*, 252:111222, 2022.

87 Pranav Sumanth Doijode, Stefan Hickel, Tom van Terwisga, and Klaas Visser. A machine learning approach for propeller design and optimization: Part i. *Applied Ocean Research*, 124:103178, 2022.

88 Hang Meng, Danyang Jin, Li Li, and Yongqian Liu. Analytical and numerical study on centrifugal stiffening effect for large rotating wind turbine blade based on nrel 5 mw and windpact 1.5 mw models. *Renewable Energy*, 183:321–329, 2022.

89 John David Anderson Jr. *Fundamentals of aerodynamics*. Tata McGraw-Hill Education, 2010.

90 Charles Hirsch. *Numerical computation of internal and external flows: The fundamentals of computational fluid dynamics*. Elsevier, 2007.

91 J Peraire, OC Zienkiewicz, and K Morgan. Shallow water problems: a general explicit formulation. *International Journal for Numerical Methods in Engineering*, 22(3):547–574, 1986.

92 Maria de Lourdes Moreira et al. Simulação computacional de escoamentos viscosos compressíveis/quase incompressíveis. 1998.

93 PAB De Sampaio and M de L Moreira. A new finite element formulation for both compressible and nearly incompressible fluid dynamics. *International journal for numerical methods in fluids*, 32(1):43–67, 2000.

94 Emil Simiu and Robert H Scanlan. Wind effects on structures: fundamentals and applications to design. 1996.

95 Kalyanmoy Deb. *Multi-objective optimization using evolutionary algorithms*, volume 16. John Wiley & Sons, 2001.

96 Licheng Jiao, Juanjuan Luo, Ronghua Shang, and Fang Liu. A modified objective function method with feasible-guiding strategy to solve constrained multi-objective optimization problems. *Applied Soft Computing*, 14:363–380, 2014.

97 Aimin Zhou, Bo-Yang Qu, Hui Li, Shi-Zheng Zhao, Ponnuthurai Nagaratnam Suganthan, and Qingfu Zhang. Multiobjective evolutionary algorithms: A survey of the state of the art. *Swarm and Evolutionary Computation*, 1(1):32–49, 2011.

98 Theodore Theodorsen. *Theory of Propellers*. McGraw-Hill, New York, 1ª edition, 1948.

99 MM Bicak and H Temel Belck. Modeling of rotating blades for vibration analysis. In *INTER-NOISE and NOISE-CON Congress and Conference Proceedings*, volume 2011, pages 2460–2477. Institute of Noise Control Engineering, 2011.

100 A Daniel Antony, M Gopalsamy, Chaparala BV Viswanadh, and R Krishnaraj. Structural dynamic analysis of turbine blade. In *IOP Conference Series: Materials Science and Engineering*, volume 247, page 012007. IOP Publishing, 2017.

101 Domenico Piccirillo. *Tool development for preliminary design of next generation low pressure turbines*. PhD thesis, Politecnico di Torino, 2019.

102 Mark Drela. Xfoil 6.9 user primer, 2020 (accessed September 12, 2020). `https://web.mit.edu/drela/Public/web/xfoil/xfoil_doc.txt`.

103 Martin Hepperle. Javaprop users guide. Technical report, 2010.

104 Miguel A Silvestre, João P Morgado, and Jose Pascoa. Jblade: a propeller design and analysis code. In *2013 International Powered Lift Conference*, page 4220, 2013.

105 D. Marten. Qblade guidelines, 2012.

106 D. Marten and J. Wendler. Qblade guidelines v0.6, 2013.

107 A Betz. Airscrews with minimum energy loss. *Report, Kaiser Wilhelm Institute for Flow Research*, 1919.

108 Theodore Theodorsen. Theory of propellers. *Skipsmodelltankens meddelelse nr. 33, April 1954*, 1954.

109 E Eugene Larrabee and Susan E French. Minimum induced loss windmills and propellers. *Journal of Wind Engineering and Industrial Aerodynamics*, 15(1-3):317–327, 1983.

110 Evan J Hughes. Multiple single objective pareto sampling. In *The 2003 Congress on Evolutionary Computation, 2003. CEC'03.*, volume 4, pages 2678–2684. IEEE, 2003.

111 Michael Selig. *UIUC Airfoil Coordinates Database*, 2020 (accessed September 12, 2020). `https://m-selig.ae.illinois.edu/ads/coord_database.html`.

112 J D'Errico. Interparc function. *MATLAB Central File Exchange*, 2012.

113 André Deperrois. Xflr5 analysis of foils and wings operating at low reynolds numbers. *Guidelines for XFLR5*, 142, 2009.

114 Song Lin. Javaprop - programmers guide, 2020 (accessed September 12, 2020). `https://www.mh-aerotools.de/airfoils/jp_programming.htm`.

115 Ye Tian, Ran Cheng, Xingyi Zhang, and Yaochu Jin. Platemo: A matlab platform for evolutionary multi-objective optimization [educational forum]. *IEEE Computational Intelligence Magazine*, 12(4):73–87, 2017.

116 Daniel C Mikkelson, Bernard J Blaha, Glenn A Mitchell, and Joseph E Wikete. Design and performance of energy efficient propellers for mach 0.8 cruise. 1977.

117 Robert J Jeracki, Daniel C Mikkelson, and Bernard J Blaha. Wind tunnel performance of four energy efficient propellers designed for mach 0.8 cruise. Technical report, SAE Technical Paper, 1979.

118 G Stefko and R Jeracki. Wind tunnel results of advanced high speed propellers in the takeoff, climb, and landing operating regimes. In *21st Joint Propulsion Conference*, page 1259, 1985.

119 James H Dittmar. Cruise noise of the sr-2 model in a wind tunnel. *NASA Technical Memorandum*, 101480:29, 1989.

120 OS Engines. Manual - max-61sx-h ring wc, 2001.

121 Horizon Hobby Inc. Manual - e-flite power 60 brushless outrunner motor, 2013.

122 Miqing Li, Liangli Zhen, and Xin Yao. How to read many-objective solution sets in parallel coordinates [educational forum]. *IEEE Computational Intelligence Magazine*, 12(4):88–100, 2017.

123 Margarita Reyes Sierra and Carlos A Coello Coello. Improving pso-based multi-objective optimization using crowding, mutation and ϵ-dominance. In *International conference on evolutionary multi-criterion optimization*, pages 505–519. Springer, 2005.

124 Eckart Zitzler and Lothar Thiele. Multiobjective evolutionary algorithms: a comparative case study and the strength pareto approach. *IEEE transactions on Evolutionary Computation*, 3(4):257–271, 1999.

125 Jason Ramon Schott. *Fault tolerant design using single and multicriteria genetic algorithm optimization*. PhD thesis, Massachusetts Institute of Technology, 1995.

126 RO Parreiras and JA Vasconcelos. Decision making in multiobjective optimization aided by the multicriteria tournament decision method. *Nonlinear Analysis: Theory, Methods & Applications*, 71(12):e191–e198, 2009.

127 Jaqueline S. Angelo, Heder S. Bernardino, and Helio J.C. Barbosa. Ant colony approaches for multiobjective structural optimization problems with a cardinality constraint. *Advances in Engineering Software*, 80:101–115, 2015.

128 Afonso CC Lemonge, Jose PG Carvalho, Patrícia H Hallak, and Denis EC Vargas. Multi-objective truss structural optimization considering natural frequencies of vibration and global stability. *Expert Systems with Applications*, 165:113777, 2021.

129 José Pedro G Carvalho, Érica CR Carvalho, Dênis EC Vargas, Patrícia H Hallak, Beatriz SLP Lima, and Afonso CC Lemonge. Multi-objective optimum design of truss structures using differential evolution algorithms. *Computers & Structures*, 252:106544, 2021.

130 Nícolas Lima Oliveira, Manuel Arturo Rendón, Afonso Celso Lemonge, and Patricia Habib Hallak. Multi-objective optimum design of propellers using the blade element theory and evolutionary algorithms. *Evolutionary Intelligence*, 2023.

131 Lucas Machado Rocha. *Estudo e dimensionamento de hélices para propulsão aeronáutica*. PhD thesis, Master's thesis, Federal University of Juiz de Fora, Juiz de Fora, Brazil, 2019.

Appendix A – QPROP Theory Background

In this Section, the steps used by Rocha [131] to demonstrate the theoretical functioning of QPROP will be demonstrated. Figure 29 demonstrates how a W speed is decomposed into two other speeds: axial and tangential. The tangential velocity v_t can be written as:

$$v_t = \frac{B\Gamma}{4\pi r F\sqrt{1+(4J_w R/\pi B r)^2}} \tag{.1}$$

The correction factor for Prandtl F is given by:

$$F = \frac{2}{\pi} arccos(e^{-f}) \tag{.2}$$

The f coefficient is written in terms of the local wake advance ratio (J_w). These two coefficients are given by:

$$f = \frac{B}{2J_w(1-r/R)} \tag{.3}$$

$$J_w = (r/R)(W_a/W_t) \tag{.4}$$

The use of the local advance ratio will provide better results for the analysis of flows subjected to high loading, as recommended by Theodorsen [31]. For the calculation of the axial component v_a, observing the perpendicularity of the vector v with the vector W, it is obtained quickly by the relationship $v_a = v_t(W_t/W_a)$. Each propeller blade element will be subjected to an angle of attack α, which will be equated as:

$$\alpha(r) = \beta - arctan(\frac{W_a}{W_t}) \tag{.5}$$

With the study of each section of the airfoil, it is possible to find a pair of variables C_L and C_D that varies with the value α, Reynolds number, and Mach number. With the value of C_L, it is possible to obtain the result of the circulation equation:

$$\Gamma = \frac{1}{2} W c\, C_L \tag{.6}$$

Although C_L is known, there is still no calculation parameter for the total speed W. Knowing the chord values c and geometric torsion angle β for each of the sessions, in addition to the aerodynamic variables and the propeller operating constants V and ω, the circulation function $\Gamma(r)$ can be calculated for each of the sections of interest. For

this, Drela [12] uses a Newton iteration with the introduction of a new variable Ψ. All variables are parameterized as a function of Ψ, using Equation .6 to calculate the residual of the method and correcting the value of Ψ for each iteration. This variable is shown in Figure 126.

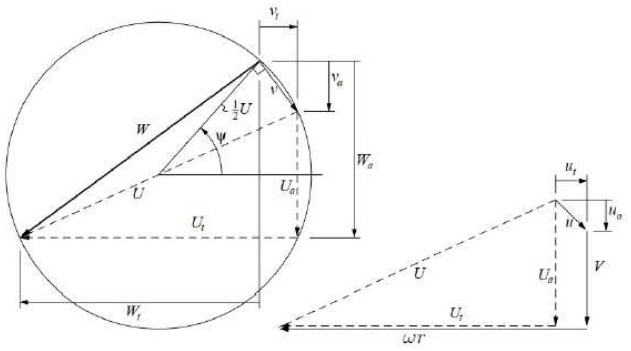

Figure 126 – Variables parametrization on ϕ - Withdrawn of [12]

Rewriting the variables according to the new parametrization variable, it's possible to write the following equations:

$$U_a = V + u_a \tag{.7}$$

$$U_t = \omega r - u_t \tag{.8}$$

$$U = \sqrt{U_a^2 + U_t^2} \tag{.9}$$

$$W_a(\psi) = \frac{1}{2}(U_a + U sen\psi) \tag{.10}$$

$$W_t(\psi) = \frac{1}{2}(U_t + U cos\psi) \tag{.11}$$

$$u_a(\psi) = W_a - U_a \tag{.12}$$

$$u_t(\psi) = U_t - W_t \tag{.13}$$

$$\alpha(\psi) = \beta - arctan(W_a/W_t) \tag{.14}$$

$$W(\psi) = \sqrt{W_a^2 + W_t^2} \tag{.15}$$

$$Re(\psi) = \rho W c/\mu \tag{.16}$$

$$Ma(\psi) = W/a \tag{.17}$$

Rewriting Equation .1 in terms of the circulation Γ and with the parameterized variables:

$$\Gamma(\psi) = v_t \frac{4\pi r}{B} F \sqrt{1 + (4\lambda_w R/\pi B r)^2} \tag{.18}$$

The residual $\Re$ of Newton's iteration is then calculated with the difference between the previous Equation and Equation .6:

$$\Re(\psi) = \Gamma - \frac{1}{2} W c \; C_{L(\alpha,Re,Ma)} \tag{.19}$$

Thus, the value of Ψ can be rewritten by adding a $\delta\Psi$ differential to this variable:

$$\delta\phi = -\frac{\Re}{d\Re/d\phi} \tag{.20}$$

The algorithm is repeated until the residual $\Re$ converges until its nullity through a convergence criterion. Using the method for each section of the airfoil, it is possible to determine a distribution of radial circulation $\Gamma(r)$, which allows the calculation of the total thrust T and total torque Q performed by the propeller. Through the developments carried out by Drela [12], dT and dQ are rewritten in order to take into account more than one blade and add the variable $\epsilon = C_D/C_L$. Thus, it is possible to write:

$$dT = \rho B \Gamma (W_t - \epsilon W_a) dr \tag{.21}$$

$$dQ = \rho B \Gamma (W_a - \epsilon W_t) r \; dr \tag{.22}$$

Through the equations above, it is possible to define the local efficiency in a given propeller section, being useful for the detailed analysis required in the development of a new propeller geometry that provides the highest possible efficiency. Thus:

$$\eta = \frac{V}{\omega R} \frac{W_t - \epsilon W_a}{W_a - \epsilon W_t} \tag{.23}$$

The thrust and total torque can be obtained by radially integrating Equations .21 and .22, respectively. These integrals can be approximated by:

$$T \simeq \rho B \sum_r \Gamma (W_t - \epsilon W_a) \Delta r \tag{.24}$$

$$Q \simeq \rho B \sum_r \Gamma (W_a - \epsilon W_t) r \Delta r \tag{.25}$$

Although the formulation presented satisfies the radial conditions of the sections, some global variables will not be calculated, but imposed by the user as a calculation parameter. Just as the residual calculation for circulation was used in Equation .19, it will also be necessary to calculate it for the multiple combinations that may be requested in the execution of the QPROP.

For the situation of analysis of a propeller, where the geometries are known and passed as input data of the program, the calculation model assumes that there may be four unknown variables: $\Gamma(r)$, V, ω and $\Delta\beta$, the last one being a condition of variation of the propeller pitch, useful for propellers that operate under the variable pitch regime. It is possible to realize at this point that the circulation will be given by a function $\Gamma(r; V; \omega; \Delta\beta)$, while the residual R defined above will not be a function of only Ψ, but will be calculated in such a way that:

$$\Re(\psi; V; \omega; \beta) = 0 \tag{.26}$$

The residual variation should be null not only in Ψ, but also for any other physical disturbances that may occur due to the other variables. This δR variation can be obtained by:

$$\delta\Re = \frac{\delta\Re}{\delta\phi}\delta\phi + \frac{\delta\Re}{\delta V}\delta V + \frac{\delta\Re}{\delta\omega}\delta\omega + \frac{\delta\Re}{\delta\Delta\beta}\delta\Delta\beta = 0 \tag{.27}$$

For the analysis problem that consists of calculating the load that exists on a propeller given the geometry, then independent plots of the residue are considered, called R_r, R_1, R_2 and R_3. While the first relates to the circulation-independent residue, the other components will depend exclusively on the type of specification that the user defines as the calculation input. The most common compositions are:

- Speed, rotation, and pitch variation;
- Speed, rotation, and torque;
- Speed, pitch variation, and thrust;
- Rotation, pitch, and thrust.

Although the torque and thrust are not defined as independent variables, it can be seen from the previous equations that these values will be found, respectively, in functions of form $Q(V, \omega, \Delta\beta)$ and $T(V, \omega, \Delta\beta)$. Thus, it is possible to rewrite these values according to the derivatives of the circulation for each of the partial derivatives required in the calculation of the residual.

Having chosen the three variables to be specified, the residuals related to these will be approximated to zero values simultaneously, through a Newton iteration for multiple variables. This condition is achieved through the following relationship:

$$\begin{Bmatrix} \delta V \\ \delta\omega \\ \delta\Delta\beta \end{Bmatrix} = [\frac{\delta(R_1, R_2, R_3)}{\delta(V, \omega, \Delta\beta}]^{-1} \begin{Bmatrix} \delta R_1 \\ \delta R_2 \\ \delta R_3\beta \end{Bmatrix} \tag{.28}$$

Finally, the overall efficiency of the propeller and the other coefficients of performance C_T and C_P can be calculated, to perform the required analysis of the studied propeller. With these developments, the use of QPROP becomes intuitive, allowing the user to interpret each of the results provided.

Appendix B – Performance indicators

Problem	AGEMOEA	ARMOEA	MSOPSII	NSGAII	NSGAIIARSBX
MOOP1	1.9357e+0 (4.49e-3) ≈	1.9367e+0 (2.11e-3) ≈	1.9356e+0 (4.53e-3) ≈	1.9386e+0 (1.55e-3) −	1.9356e+0 (3.34e-3) +
MOOP2	1.4539e+0 (1.09e-2) ≈	1.4546e+0 (9.49e-3) ≈	1.4538e+0 (9.45e-3) ≈	1.4484e+0 (1.12e-2) ≈	1.4588e+0 (1.45e-2) ≈
MOOP3	1.9298e+0 (9.67e-3) ≈	1.9414e+0 (1.92e-2) ≈	1.9244e+0 (2.85e-2) ≈	1.9288e+0 (1.02e-2) ≈	1.9392e+0 (1.41e-2) ≈
MOOP4	2.1500e+0 (1.82e-2) +	2.1561e+0 (7.65e-3) ≈	2.1724e+0 (5.25e-3) −	2.1643e+0 (4.77e-3) −	2.1604e+0 (5.74e-3) +
MOOP5	2.1771e+0 (2.05e-3) ≈	2.1788e+0 (1.49e-3) ≈	2.1759e+0 (6.19e-3) ≈	2.1779e+0 (2.31e-3) ≈	2.1782e+0 (2.41e-3) ≈
MOOP6	1.7600e+0 (3.92e-3) ≈	1.7607e+0 (6.61e-3) ≈	1.7635e+0 (1.29e-2) ≈	1.7615e+0 (4.72e-3) ≈	1.7609e+0 (4.93e-3) ≈
MOOP7	2.3750e+0 (6.29e-3) +	2.3745e+0 (5.93e-3) +	2.3867e+0 (6.06e-3) ≈	2.3810e+0 (3.45e-3) ≈	2.3837e+0 (3.48e-3) ≈
+/ − / ≈	2/0/5	1/0/6	0/1/6	0/2/5	2/0/5

Table 20 – IGD - OS

Problem	AGEMOEA	ARMOEA	MSOPSII	NSGAII	NSGAIIARSBX
MOOP1	9.9618e-1 (8.81e-4) ≈	9.9562e-1 (1.50e-3) ≈	9.9599e-1 (1.69e-3) ≈	9.9559e-1 (9.84e-4) ≈	9.9581e-1 (8.63e-4) ≈
MOOP2	9.9214e-1 (1.30e-3) ≈	9.9264e-1 (1.37e-3) ≈	9.9207e-1 (1.12e-3) ≈	9.9317e-1 (1.45e-3) +	9.9182e-1 (1.88e-3) −
MOOP3	9.9992e-1 (1.28e-5) ≈	9.9993e-1 (1.95e-5) ≈	9.9977e-1 (3.46e-4) ≈	9.9992e-1 (1.68e-5) ≈	9.9994e-1 (1.63e-5) ≈
MOOP4	9.8833e-1 (9.13e-4) ≈	9.8831e-1 (1.09e-3) ≈	9.8758e-1 (6.41e-4) −	9.8787e-1 (5.35e-4) ≈	9.8807e-1 (4.33e-4) ≈
MOOP5	9.9453e-1 (8.38e-4) ≈	9.9430e-1 (1.08e-3) ≈	9.9646e-1 (2.27e-3) ≈	9.9419e-1 (1.00e-3) ≈	9.9454e-1 (9.82e-4) ≈
MOOP6	9.9297e-1 (5.66e-4) ≈	9.9240e-1 (1.03e-3) ≈	9.9154e-1 (1.76e-3) ≈	9.9284e-1 (7.82e-4) ≈	9.9295e-1 (8.70e-4) ≈
MOOP7	9.8820e-1 (5.58e-4) +	9.8774e-1 (3.06e-4) ≈	9.8662e-1 (1.04e-3) ≈	9.8779e-1 (3.13e-4) ≈	9.8735e-1 (5.61e-4) ≈
+/ − / ≈	1/0/6	0/0/7	0/1/6	1/0/6	0/1/6

Table 21 – HV - OS

Problem	AGEMOEA	ARMOEA	MSOPSII	NSGAII	NSGAIIARSBX
MOOP1	1.0000e+0 (0.00e+0) ≈	1.0000e+0 (0.00e+0) ≈	4.0000e-1 (5.16e-1) −	1.0000e+0 (0.00e+0) ≈	1.0000e+0 (0.00e+0) ≈
MOOP2	1.0000e+0 (0.00e+0) ≈	1.0000e+0 (0.00e+0) ≈	5.0300e-1 (5.24e-1) −	1.0000e+0 (0.00e+0) ≈	1.0000e+0 (0.00e+0) ≈
MOOP3	1.0000e+0 (0.00e+0) ≈	1.0000e+0 (0.00e+0) ≈	5.1200e-1 (5.14e-1) −	1.0000e+0 (0.00e+0) ≈	1.0000e+0 (0.00e+0) ≈
MOOP4	1.0000e+0 (0.00e+0) ≈	1.0000e+0 (0.00e+0) ≈	1.0000e+0 (0.00e+0) ≈	1.0000e+0 (0.00e+0) ≈	1.0000e+0 (0.00e+0) ≈
MOOP5	1.0000e+0 (0.00e+0) ≈	1.0000e+0 (0.00e+0) ≈	6.0400e-1 (5.11e-1) −	1.0000e+0 (0.00e+0) ≈	1.0000e+0 (0.00e+0) ≈
MOOP6	1.0000e+0 (0.00e+0) ≈	1.0000e+0 (0.00e+0) ≈	5.0000e-1 (5.27e-1) −	1.0000e+0 (0.00e+0) ≈	1.0000e+0 (0.00e+0) ≈
MOOP7	1.0000e+0 (0.00e+0) ≈	1.0000e+0 (0.00e+0) ≈	6.0000e-1 (5.16e-1) −	1.0000e+0 (0.00e+0) ≈	1.0000e+0 (0.00e+0) ≈
+/ − / ≈	0/0/7	0/0/7	0/6/1	0/0/7	0/0/7

Table 22 – Feasible Rate - OS

Problem	AGEMOEA	ARMOEA	MSOPSII	NSGAII	NSGAIIARSBX
MOOP1	1.4158e-3 (1.06e-3) ≈	1.5595e-3 (5.00e-4) ≈	3.8113e-3 (1.64e-3) −	1.1759e-3 (1.60e-4) ≈	1.2277e-3 (2.75e-4) ≈
MOOP2	6.9000e-4 (2.91e-4) ≈	7.3633e-4 (4.94e-4) ≈	9.6007e-3 (5.46e-3) −	8.3256e-4 (2.20e-4) ≈	7.1306e-4 (1.08e-4) ≈
MOOP3	6.3246e-4 (1.42e-3) ≈	1.8119e-4 (2.27e-4) ≈	5.4400e-4 (6.50e-4) ≈	1.0180e-3 (1.67e-3) ≈	1.2493e-3 (1.87e-3) ≈
MOOP4	1.5846e-3 (3.61e-4) ≈	2.0920e-3 (2.17e-4) −	6.1086e-3 (2.09e-3) −	1.3385e-3 (2.03e-4) ≈	1.6670e-3 (7.12e-4) ≈
MOOP5	1.3364e-3 (3.16e-4) −	1.1044e-3 (1.98e-4) ≈	5.9236e-3 (8.49e-3) −	8.9360e-4 (1.62e-4) ≈	1.0640e-3 (2.30e-4) ≈
MOOP6	4.2145e-4 (4.25e-5) +	7.2536e-4 (1.46e-4) −	1.8404e-3 (4.66e-4) −	5.1251e-4 (5.19e-5) ≈	5.1447e-4 (6.56e-5) ≈
MOOP7	1.9959e-3 (3.40e-4) −	2.5194e-3 (3.79e-4) −	3.9466e-3 (1.82e-3) −	1.6673e-3 (4.01e-4) ≈	1.5920e-3 (4.88e-4) ≈
+/ − / ≈	1/2/4	0/3/4	0/6/1	0/0/7	0/0/7

Table 23 – Spacing - OS

Problem	AGEMOEA	ARMOEA	MSOPSII	NSGAII	NSGAIIARSBX
MOOP1	2.0783e+0 (3.54e-3) ≈	2.0772e+0 (5.74e-3) ≈	2.0794e+0 (5.67e-3) −	2.0786e+0 (4.52e-3) ≈	2.0769e+0 (4.80e-3) ≈
MOOP2	1.4526e+0 (1.14e-2) +	1.4608e+0 (1.23e-2) ≈	1.4570e+0 (9.04e-3) ≈	1.4601e+0 (6.70e-3) ≈	1.4652e+0 (1.24e-2) ≈
MOOP3	2.0679e+0 (1.30e-2) ≈	2.0707e+0 (1.05e-2) ≈	2.0586e+0 (2.28e-2) ≈	2.0685e+0 (1.10e-2) ≈	2.0727e+0 (1.13e-2) ≈
MOOP4	2.2859e+0 (5.30e-3) ≈	2.2832e+0 (5.29e-3) +	2.3009e+0 (1.04e-3) −	2.2916e+0 (7.73e-3) ≈	2.2908e+0 (3.86e-3) ≈
MOOP5	2.3047e+0 (1.91e-3) ≈	2.3048e+0 (5.19e-3) −	2.3067e+0 (4.70e-3) ≈	2.3057e+0 (2.00e-3) ≈	2.3041e+0 (1.99e-3) ≈
MOOP6	1.7671e+0 (4.74e-3) −	1.7659e+0 (5.12e-3) −	1.7587e+0 (7.03e-3) ≈	1.7630e+0 (1.06e-2) ≈	1.7592e+0 (7.16e-3) ≈
MOOP7	2.4875e+0 (8.88e-3) +	2.4928e+0 (4.43e-3) ≈	2.5057e+0 (6.77e-3) −	2.4997e+0 (1.36e-3) ≈	2.4959e+0 (6.18e-3) ≈
+/ − / ≈	2/1/4	1/2/4	0/3/4	0/0/7	0/0/7

Table 24 – IGD - BL

Problem	AGEMOEA	ARMOEA	MSOPSII	NSGAII	NSGAIIARSBX
MOOP1	9.9158e-1 (2.93e-3) ≈	9.9358e-1 (2.75e-3) ≈	9.9198e-1 (2.81e-3) ≈	9.9159e-1 (3.72e-3) ≈	9.9309e-1 (3.41e-3) ≈
MOOP2	9.9040e-1 (1.64e-3) ≈	9.8948e-1 (1.75e-3) ≈	9.8954e-1 (1.68e-3) ≈	9.8974e-1 (1.17e-3) ≈	9.8921e-1 (2.01e-3) ≈
MOOP3	9.9991e-1 (2.33e-5) ≈	9.9992e-1 (1.82e-5) ≈	9.9986e-1 (9.46e-5) ≈	9.9992e-1 (1.20e-5) ≈	9.9991e-1 (2.82e-5) ≈
MOOP4	9.8098e-1 (3.91e-3) ≈	9.8295e-1 (3.81e-3) ≈	9.8057e-1 (2.09e-3) ≈	9.7986e-1 (2.81e-3) ≈	9.7910e-1 (5.12e-3) ≈
MOOP5	9.8682e-1 (2.15e-3) −	9.8854e-1 (3.60e-3) ≈	9.8663e-1 (2.86e-3) −	9.8828e-1 (1.57e-3) ≈	9.9064e-1 (3.31e-3) ≈
MOOP6	9.8827e-1 (1.47e-3) −	9.8897e-1 (1.14e-3) ≈	9.8852e-1 (2.37e-3) ≈	9.8892e-1 (2.13e-3) ≈	9.9058e-1 (2.27e-3) ≈
MOOP7	9.8000e-1 (5.01e-3) ≈	9.7974e-1 (3.97e-3) ≈	9.7887e-1 (7.29e-3) ≈	9.7874e-1 (3.18e-3) ≈	9.7901e-1 (3.69e-3) ≈
+/ − / ≈	0/2/5	0/0/7	0/1/6	0/0/7	0/0/7

Table 25 – HV - BL

Problem	AGEMOEA	ARMOEA	MSOPSII	NSGAII	NSGAIIARSBX
MOOP1	1.0000e+0 (0.00e+0) ≈	1.0000e+0 (0.00e+0) ≈	6.0000e-1 (5.16e-1) −	1.0000e+0 (0.00e+0) ≈	1.0000e+0 (0.00e+0) ≈
MOOP2	1.0000e+0 (0.00e+0) ≈	1.0000e+0 (0.00e+0) ≈	6.0000e-1 (5.16e-1) −	1.0000e+0 (0.00e+0) ≈	1.0000e+0 (0.00e+0) ≈
MOOP3	1.0000e+0 (0.00e+0) ≈	1.0000e+0 (0.00e+0) ≈	9.0000e-1 (3.16e-1) ≈	1.0000e+0 (0.00e+0) ≈	1.0000e+0 (0.00e+0) ≈
MOOP4	1.0000e+0 (0.00e+0) ≈	1.0000e+0 (0.00e+0) ≈	6.0000e-1 (5.16e-1) −	1.0000e+0 (0.00e+0) ≈	1.0000e+0 (0.00e+0) ≈
MOOP5	1.0000e+0 (0.00e+0) ≈	1.0000e+0 (0.00e+0) ≈	8.0000e-1 (4.22e-1) ≈	1.0000e+0 (0.00e+0) ≈	1.0000e+0 (0.00e+0) ≈
MOOP6	1.0000e+0 (0.00e+0) ≈	1.0000e+0 (0.00e+0) ≈	8.0000e-1 (4.22e-1) ≈	1.0000e+0 (0.00e+0) ≈	1.0000e+0 (0.00e+0) ≈
MOOP7	1.0000e+0 (0.00e+0) ≈	1.0000e+0 (0.00e+0) ≈	7.0000e-1 (4.83e-1) ≈	1.0000e+0 (0.00e+0) ≈	1.0000e+0 (0.00e+0) ≈
+/ − / ≈	0/0/7	0/0/7	0/3/4	0/0/7	0/0/7

Table 26 – Feasible Rate - BL

Problem	AGEMOEA	ARMOEA	MSOPSII	NSGAII	NSGAIIARSBX
MOOP1	1.5967e-3 (4.31e-4) ≈	1.4510e-3 (3.61e-4) ≈	6.6519e-3 (3.26e-3) −	1.8931e-3 (6.81e-4) ≈	1.9141e-3 (8.64e-4) ≈
MOOP2	7.1830e-4 (3.01e-4) +	9.8466e-4 (4.99e-4) ≈	1.0526e-2 (5.34e-3) −	1.3059e-3 (5.80e-4) ≈	1.2829e-3 (5.76e-4) ≈
MOOP3	3.9747e-4 (7.38e-4) ≈	3.0867e-4 (3.48e-4) ≈	6.5956e-4 (4.09e-4) ≈	6.0328e-4 (9.84e-4) ≈	4.2086e-4 (6.53e-4) ≈
MOOP4	1.6773e-3 (2.25e-4) ≈	2.5641e-3 (3.99e-4) −	3.6895e-3 (1.38e-3) −	1.7395e-3 (4.71e-4) ≈	1.8295e-3 (2.73e-4) ≈
MOOP5	2.1949e-3 (1.32e-3) −	1.7682e-3 (6.44e-4) −	3.1848e-3 (1.28e-3) −	1.2215e-3 (1.00e-4) ≈	1.2589e-3 (2.37e-4) ≈
MOOP6	1.0701e-3 (3.26e-4) ≈	1.5788e-3 (6.60e-4) +	5.7197e-3 (4.70e-3) −	1.1354e-3 (8.92e-4) ≈	1.8519e-3 (3.39e-3) ≈
MOOP7	2.7822e-3 (7.65e-4) −	3.0542e-3 (3.94e-4) −	3.3366e-3 (1.15e-3) −	1.8055e-3 (1.77e-4) ≈	1.9652e-3 (5.87e-4) ≈
+/ − / ≈	1/2/4	1/3/3	0/6/1	0/0/7	0/0/7

Table 27 – Spacing - BL

Appendix C – Operational optimization

Common Data			3 Rotational Speed Flight Data						Multi Rotational Speed Flight Data						
Segment	Velocity	Thrust	RPM	Power	CP	CT	Eta	Beta	RPM	Power	CP	CT	Eta	Beta	Power_Diff
[-]	[m/s]	[N]	[rpm]	[kW]	[-]	[-]	[-]	[°]	[rpm]	[kW]	[-]	[-]	[-]	[°]	[-]
TakeOff	47.30	11137.3	2650	949.3	0.384	0.374	0.555	50.08	2795	917.0	0.316	0.337	0.575	49.14	-3.41%
Climb 1	52.14	8012.4	2250	665.3	0.446	0.378	0.628	52.97	2594	640.6	0.280	0.285	0.653	49.40	-3.73%
Climb 2	55.67	7721.8	2250	659.5	0.443	0.366	0.652	53.37	2493	647.9	0.320	0.298	0.664	50.16	-1.76%
Climb 3	58.48	7429.4	2250	647.8	0.437	0.353	0.671	53.62	2532	636.6	0.302	0.279	0.683	50.01	-1.73%
Climb 4	62.01	7187.8	2250	645.7	0.437	0.343	0.690	54.12	2548	639.6	0.298	0.268	0.698	49.94	-0.95%
Climb 5	64.83	6844.7	2250	626.9	0.426	0.328	0.708	54.32	2549	622.9	0.291	0.256	0.713	50.20	-0.65%
Climb 6	68.35	6533.4	2250	615.0	0.420	0.314	0.726	54.73	2510	605.9	0.298	0.253	0.737	51.71	-1.47%
Climb 7	71.17	6253.6	2250	601.3	0.412	0.302	0.740	55.03	2482	598.0	0.305	0.248	0.745	51.76	-0.55%
Climb 8	74.69	5962.1	2250	589.4	0.405	0.289	0.756	55.48	2424	587.5	0.323	0.249	0.758	53.00	-0.33%
Climb 9	77.51	5717.1	2250	577.7	0.399	0.278	0.767	55.83	2384	576.5	0.335	0.248	0.769	53.91	-0.21%
Climb 10	81.03	5494.6	2250	571.7	0.396	0.268	0.779	56.38	2372	570.8	0.338	0.241	0.780	54.62	-0.16%
Climb 11	83.85	5253.0	2250	558.5	0.389	0.258	0.789	56.73	2329	558.0	0.350	0.240	0.789	55.58	-0.08%
Climb 12	86.67	5049.6	2250	549.0	0.384	0.249	0.797	57.13	2299	548.8	0.359	0.238	0.797	56.41	-0.03%
Climb 13	90.19	4838.9	2250	541.5	0.380	0.239	0.806	57.68	2262	541.5	0.374	0.237	0.806	57.50	0.00%
Climb 14	93.01	4640.7	2250	531.2	0.374	0.230	0.813	58.08	2213	531.1	0.393	0.238	0.813	58.65	-0.01%
Climb 15	95.83	4445.1	2250	520.4	0.368	0.221	0.818	58.48	2170	520.1	0.410	0.238	0.819	59.71	-0.05%
Climb 16	99.35	4282.3	2250	516.3	0.366	0.214	0.824	59.08	2137	515.8	0.427	0.237	0.825	60.84	-0.09%
Climb 17	102.17	4129.0	2250	509.4	0.363	0.207	0.828	59.53	2105	508.6	0.442	0.237	0.830	61.80	-0.15%
Climb 18	104.99	3942.9	2250	497.5	0.356	0.199	0.832	59.93	2066	496.3	0.458	0.236	0.834	62.83	-0.24%
Climb 19	108.51	3795.6	2250	492.8	0.354	0.192	0.836	60.53	2026	491.2	0.483	0.237	0.839	64.09	-0.33%
Climb 20	111.33	3660.4	2250	486.1	0.350	0.186	0.838	60.98	1991	484.1	0.503	0.237	0.842	65.14	-0.40%
Climb 21	114.15	3528.3	2250	479.2	0.347	0.180	0.841	61.43	1966	476.7	0.517	0.236	0.845	66.00	-0.50%
Cruise 1	113.99	3500.4	1700	475.8	0.798	0.312	0.839	71.16	1959	472.5	0.518	0.235	0.845	66.06	-0.70%
Cruise 2	113.99	3437.3	1700	466.5	0.782	0.307	0.840	71.04	1949	463.2	0.515	0.233	0.846	66.13	-0.70%
Cruise 3	113.99	3331.1	1700	450.9	0.756	0.297	0.842	70.84	1907	448.8	0.533	0.236	0.847	66.73	-0.46%
Cruise 4	113.99	3262.2	1700	440.9	0.739	0.291	0.844	70.71	1900	439.3	0.528	0.233	0.847	66.75	-0.36%

Common Data			3 Rotational Speed Flight Data						Multi Rotational Speed Flight Data						
Segment	Velocity	Thrust	RPM	Power	CP	CT	Eta	Beta	RPM	Power	CP	CT	Eta	Beta	Power_Diff
[-]	[m/s]	[N]	[rpm]	[kW]	[-]	[-]	[-]	[°]	[rpm]	[kW]	[-]	[-]	[-]	[°]	[-]
Cruise 5	113.99	3198.0	1700	431.6	0.724	0.285	0.845	70.59	1884	429.8	0.529	0.232	0.848	66.94	-0.41%
Cruise 6	113.99	3128.3	1700	421.5	0.707	0.279	0.846	70.46	1853	420.3	0.544	0.235	0.849	67.41	-0.28%
Cruise 7	113.99	3026.0	1700	406.9	0.682	0.270	0.848	70.27	1818	406.2	0.557	0.236	0.849	67.90	-0.16%
Cruise 8	113.99	2955.9	1700	396.9	0.666	0.264	0.849	70.14	1799	396.7	0.561	0.236	0.850	68.15	-0.05%
Cruise 9	113.99	2887.3	1700	387.2	0.649	0.258	0.850	70.01	1800	387.2	0.547	0.230	0.851	68.01	0.00%
Cruise 10	113.99	2822.5	1700	378.1	0.634	0.252	0.851	69.89	1753	377.7	0.578	0.237	0.851	68.81	-0.11%
Cruise 11	113.99	2716.0	1700	363.3	0.609	0.242	0.852	69.69	1723	363.2	0.585	0.236	0.852	69.23	-0.04%
Cruise 12	113.99	2646.4	1700	353.7	0.593	0.236	0.853	69.56	1702	353.1	0.591	0.236	0.853	69.53	-0.17%
Cruise 13	113.99	2576.7	1700	344.2	0.577	0.230	0.853	69.43	1693	344.0	0.585	0.232	0.853	69.58	-0.05%
Cruise 14	113.99	2474.0	1700	330.2	0.554	0.221	0.854	69.24	1667	330.2	0.587	0.230	0.854	69.92	-0.01%
Cruise 15	113.99	2403.7	1700	320.7	0.538	0.215	0.854	69.11	1644	320.7	0.595	0.230	0.855	70.26	0.00%
Descent 1	113.99	1596.2	1700	214.9	0.360	0.142	0.847	67.64	1357	212.1	0.699	0.224	0.858	74.94	-1.28%
Descent 2	111.49	1657.0	1700	217.9	0.364	0.147	0.848	67.16	1379	215.1	0.673	0.224	0.858	73.99	-1.27%
Descent 3	108.98	1722.5	1700	221.2	0.368	0.153	0.849	66.68	1406	218.6	0.643	0.223	0.858	72.92	-1.17%
Descent 4	105.85	1793.5	1700	223.6	0.371	0.158	0.849	66.05	1406	221.1	0.648	0.231	0.857	72.35	-1.11%
Descent 5	103.35	1833.6	1700	223.2	0.369	0.161	0.849	65.50	1437	221.3	0.605	0.226	0.856	71.09	-0.86%
Descent 6	100.21	1417.0	1700	169.6	0.279	0.124	0.837	63.91	1270	165.7	0.654	0.223	0.858	73.36	-2.29%
Descent 7	97.71	1512.6	1700	175.9	0.288	0.132	0.840	63.43	1292	172.5	0.644	0.229	0.857	72.41	-1.96%
Descent 8	94.58	1554.9	1700	175.1	0.286	0.135	0.840	62.67	1300	171.8	0.627	0.231	0.856	71.49	-1.86%
Descent 9	92.07	1631.0	1700	178.7	0.290	0.141	0.841	62.13	1313	175.6	0.620	0.237	0.855	70.68	-1.69%
Descent 10	88.94	1088.5	1700	118.9	0.193	0.094	0.814	60.17	1103	112.6	0.667	0.222	0.858	73.90	-5.32%
Descent 11	86.43	1149.7	1700	121.5	0.196	0.099	0.818	59.56	1123	115.5	0.647	0.226	0.858	72.80	-4.92%
Descent 12	83.30	1199.8	1700	122.0	0.196	0.103	0.819	58.73	1142	116.6	0.618	0.227	0.856	71.49	-4.40%
Descent 13	80.80	1273.8	1700	125.3	0.201	0.109	0.822	58.12	1171	120.3	0.589	0.229	0.855	70.12	-3.94%
Descent 14	77.67	1368.2	1700	129.1	0.206	0.116	0.823	57.35	1203	124.9	0.562	0.232	0.851	68.54	-3.21%
Descent 15	74.53	1445.9	1700	130.9	0.208	0.122	0.823	56.53	1223	126.9	0.541	0.236	0.848	67.20	-3.09%

Common Data			3 Rotational Speed Flight Data						Multi Rotational Speed Flight Data						
Segment	Velocity	Thrust	RPM	Power	CP	CT	Eta	Beta	RPM	Power	CP	CT	Eta	Beta	Power_Diff
[-]	[m/s]	[N]	[rpm]	[kW]	[-]	[-]	[-]	[°]	[rpm]	[kW]	[-]	[-]	[-]	[°]	[-]
Descent 16	72.03	1555.3	1700	136.1	0.215	0.131	0.823	55.97	1264	132.7	0.511	0.237	0.843	65.58	-2.56%
Descent 17	68.90	1634.4	1700	137.4	0.217	0.137	0.820	55.14	1286	134.3	0.489	0.240	0.838	64.17	-2.22%
Descent 18	66.39	1720.5	1700	139.8	0.220	0.144	0.817	54.51	1316	137.3	0.465	0.240	0.833	62.78	-1.81%
Descent 19	63.26	1812.3	1700	141.2	0.221	0.151	0.812	53.68	1356	138.8	0.428	0.237	0.825	60.91	-1.74%
Descent 20	60.13	1929.2	1700	144.1	0.225	0.160	0.805	52.90	1393	142.1	0.403	0.238	0.816	59.23	-1.38%
Descent 21	57.62	2048.9	1700	148.0	0.230	0.169	0.798	52.33	1445	146.4	0.370	0.235	0.807	57.45	-1.04%
DClimb 1	52.14	8012.4	2250	665.3	0.446	0.378	0.628	52.97	2640	629.4	0.261	0.275	0.665	48.38	-5.41%
DClimb 2	55.67	7721.9	2250	659.5	0.443	0.366	0.652	53.37	2620	624.7	0.266	0.270	0.689	48.63	-5.29%
DClimb 3	58.48	7429.5	2250	647.8	0.437	0.353	0.671	53.62	2596	635.2	0.279	0.266	0.685	49.10	-1.96%
DClimb 4	62.01	7187.8	2250	645.7	0.437	0.343	0.690	54.12	2571	638.1	0.290	0.263	0.699	49.63	-1.18%
DClimb 5	64.83	6844.7	2250	626.9	0.426	0.328	0.708	54.32	2531	618.9	0.296	0.260	0.718	50.34	-1.28%
DClimb 6	68.35	6533.5	2250	615.0	0.420	0.314	0.726	54.73	2509	611.3	0.301	0.253	0.731	51.12	-0.60%
DClimb 7	71.17	6253.6	2250	601.3	0.412	0.302	0.740	55.03	2472	598.0	0.309	0.250	0.745	51.88	-0.54%
DClimb 8	74.69	5962.1	2250	589.4	0.405	0.289	0.756	55.48	2424	587.5	0.323	0.249	0.758	53.00	-0.33%
DClimb 9	77.51	5717.1	2250	577.7	0.399	0.278	0.767	55.83	2384	576.5	0.335	0.248	0.769	53.91	-0.21%
DClimb 10	81.03	5494.6	2250	571.7	0.396	0.268	0.779	56.38	2366	570.8	0.340	0.243	0.780	54.70	-0.16%
DClimb 11	83.85	5253.0	2250	558.5	0.389	0.258	0.789	56.73	2329	558.0	0.350	0.240	0.789	55.58	-0.08%
DClimb 12	86.67	5049.6	2250	549.0	0.384	0.249	0.797	57.13	2299	548.8	0.359	0.238	0.797	56.41	-0.03%
DClimb 13	90.19	4838.9	2250	541.5	0.380	0.239	0.806	57.68	2262	541.5	0.374	0.237	0.806	57.50	0.00%
DClimb 14	93.01	4640.7	2250	531.2	0.374	0.230	0.813	58.08	2213	531.1	0.393	0.238	0.813	58.65	-0.01%
DClimb 15	95.83	4445.1	2250	520.4	0.368	0.221	0.818	58.48	2170	520.1	0.410	0.238	0.819	59.71	-0.05%
DClimb 16	99.35	4282.2	2250	516.2	0.366	0.214	0.824	59.08	2137	515.8	0.427	0.237	0.825	60.84	-0.09%
DClimb 17	102.17	4129.0	2250	509.4	0.363	0.207	0.828	59.53	2117	508.6	0.435	0.234	0.829	61.60	-0.15%
DClimb 18	104.99	3942.9	2250	497.5	0.356	0.199	0.832	59.93	2066	496.3	0.458	0.236	0.834	62.83	-0.24%
DClimb 19	108.51	3795.6	2250	492.8	0.354	0.192	0.836	60.53	2026	491.2	0.483	0.237	0.839	64.09	-0.33%
DClimb 20	111.33	3660.4	2250	486.1	0.350	0.186	0.838	60.98	1991	484.1	0.503	0.237	0.842	65.14	-0.40%

Common Data			3 Rotational Speed Flight Data						Multi Rotational Speed Flight Data						
Segment	Velocity	Thrust	RPM	Power	CP	CT	Eta	Beta	RPM	Power	CP	CT	Eta	Beta	Power_Diff
[-]	[m/s]	[N]	[rpm]	[kW]	[-]	[-]	[-]	[°]	[rpm]	[kW]	[-]	[-]	[-]	[°]	[-]
DClimb 21	114.15	3528.3	2250	479.2	0.347	0.180	0.841	61.43	1966	476.7	0.517	0.236	0.845	66.00	-0.50%
DDescent 1	113.99	675.6	1700	101.3	0.170	0.060	0.760	66.01	1032	92.7	0.694	0.163	0.830	80.66	-8.56%
DDescent 2	111.49	712.5	1700	103.4	0.173	0.063	0.768	65.47	1032	94.5	0.705	0.171	0.836	80.24	-8.65%
DDescent 3	108.36	752.7	1700	105.1	0.175	0.067	0.776	64.77	1044	96.4	0.692	0.176	0.842	79.35	-8.29%
DDescent 4	105.22	798.9	1700	107.2	0.178	0.070	0.784	64.06	1052	99.3	0.694	0.184	0.847	78.58	-7.39%
DDescent 5	102.09	826.6	1700	107.1	0.177	0.073	0.788	63.30	1047	99.3	0.702	0.192	0.850	78.08	-7.28%
DDescent 6	98.96	901.7	1700	111.8	0.184	0.079	0.798	62.61	1050	104.0	0.726	0.206	0.854	77.48	-6.94%
DDescent 7	95.83	945.0	1700	112.8	0.185	0.082	0.803	61.84	1071	105.8	0.693	0.208	0.856	76.23	-6.23%
DDescent 8	92.70	1037.8	1700	118.5	0.193	0.090	0.812	61.15	1089	111.7	0.694	0.219	0.858	75.19	-5.73%
DDescent 9	90.19	1085.8	1700	120.2	0.195	0.094	0.815	60.53	1098	114.2	0.689	0.225	0.858	74.42	-5.00%
DDescent 10	87.06	1159.2	1700	123.2	0.200	0.100	0.819	59.77	1128	117.6	0.652	0.227	0.858	72.89	-4.54%
DDescent 11	83.93	1211.8	1700	123.9	0.200	0.104	0.821	58.95	1155	118.4	0.609	0.225	0.856	71.34	-4.45%
DDescent 12	80.80	1297.5	1700	127.4	0.205	0.111	0.823	58.18	1165	122.8	0.613	0.237	0.854	70.41	-3.60%
DDescent 13	77.67	1363.0	1700	128.6	0.206	0.116	0.823	57.35	1187	124.4	0.585	0.239	0.851	69.00	-3.21%
DDescent 14	74.53	1467.9	1700	132.8	0.212	0.125	0.824	56.59	1239	129.0	0.532	0.235	0.847	66.84	-2.83%
DDescent 15	71.40	1567.1	1700	136.0	0.216	0.133	0.823	55.81	1267	132.8	0.510	0.239	0.842	65.35	-2.38%
DDescent 16	68.27	1646.9	1700	137.3	0.217	0.139	0.819	54.98	1307	134.4	0.468	0.235	0.837	63.46	-2.07%
DDescent 17	65.14	1757.1	1700	140.4	0.221	0.147	0.815	54.20	1342	138.1	0.443	0.237	0.829	61.80	-1.66%
DDescent 18	62.01	1875.1	1700	143.7	0.226	0.157	0.809	53.43	1389	141.6	0.408	0.235	0.821	59.87	-1.44%
DDescent 19	58.88	1992.1	1700	146.3	0.229	0.166	0.801	52.65	1430	144.5	0.380	0.234	0.811	58.11	-1.25%
DDescent 20	55.74	2135.3	1700	150.4	0.234	0.177	0.792	51.93	1466	148.9	0.362	0.238	0.799	56.58	-0.96%
DDescent 21	52.61	2272.9	1700	153.4	0.238	0.188	0.779	51.20	1498	152.6	0.346	0.242	0.785	55.16	-0.57%
DHold 1	52.14	8012.4	2250	665.3	0.446	0.378	0.628	52.97	2555	619.2	0.283	0.294	0.676	57.63	-6.94%
DHold 2	55.67	7237.7	2250	607.6	0.409	0.343	0.663	52.62	2584	548.9	0.244	0.260	0.735	56.36	-9.66%
DHold 3	58.48	6484.0	2250	547.3	0.369	0.308	0.693	52.18	2620	517.7	0.221	0.227	0.733	48.05	-5.41%